UNIVERSITE DE LIMOGES

Ecole Doctorale Science – Technologie – Santé

Ecole Nationale Supérieure de Céramique Industrielle

Année : 2005 Thèse N° [ ]

Thèse

Pour obtenir le grade de

DOCTEUR DE L'UNIVERSITE DE LIMOGES

Discipline : Matériaux Céramiques et Traitements de Surface

Présentée et soutenue par

Sebastian Kowalski

Le 6 juillet 2005

Rheology based investigation of a polymer-mineral powder mix for low pressure injection moulding

Thèse dirigée par M. Pierre ABELARD

JURY :

M. Christian CARROT	Professeur, Université Jean Monnet, Saint Etienne	Rapporteur
M. Albert MAGNIN	Directeur de Recherche au CNRS, Grenoble	Rapporteur
M. Richard BROOK	Professeur, Université d'Oxford	Président
M. Pierre ABELARD	Professeur, SPCTS-ENSCI, Limoges	Directeur de thèse
M. Jean François BAUMARD	Professeur, SPCTS-ENSCI, Limoges	Examinateur
M. Thierry CHARTIER	Directeur de Recherche au CNRS, Limoges	Examinateur

Gutta cavat lapidem non vi, sed saepe cadendo
Sic homo doctus fit non vi, sed saepe studendo

To Anna

Acknowledgments

I like to thank Prof. P. Abélard for the opportunity to do this thesis at SPCTS laboratory, for the freedom to realize my ideas and his help and support throughout the work. He showed me that scientific research not only consists of working in the lab, but also in communicating that work to other people, and who had to show utmost patience with all my 'stupid' questions. It was a great pleasure for me to work under his supervision.

I want to thank Prof. Ch. Carrot from the UJM, Saint Etienne and Dr. A. Magnin, Research Director CNRS, Grenoble that they accepted to be my co-reviewer.

The final version of this work was substantially improved by the help of many people, especially Prof. T. Chartier, his advice is gratefully acknowledged.

I would like to express my gratitude towards the European Community (the European Social Funds) and the Limousin Region for their financial support of the present work.

Last but not least, I like to thank my parents and my brother for always believing in and supporting me.

I Introduction

The past 20 years have seen a significant increase in research and development efforts in advanced ceramics, with strong industrial interest and optimistic forecasts for commercial growth. However, while the sales of electronic ceramics have grown more than 30 percent annually in the worldwide market since 1975, engineering or structural ceramics have not lived up to commercial expectations despite significant technological advances. A major barrier has been their high cost of processing and manufacture.

Forming is a key process step in determining the cost competitiveness of engineering ceramics as high performance products. Typically, ceramics shrink to about two-thirds of their green (unfired) volume, during sintering. Therefore, it is extremely difficult to fabricate ceramics to a net shape with required dimensional tolerances. Furthermore, because ceramics are brittle and hard, machining is difficult and can introduce flaws that lead to failure in use. During the past 10 to 15 years, the goal has been to develop net shape-forming processes that produce a final product, which requires little or no machining. The major forming methods are: slip casting, extrusion, uniaxial pressing, isostatic pressing, tape casting and injection moulding.

Injection moulding is particularly suited to the production of complex shapes. It is currently used to mass-produce a large number of small ceramic parts including: cores for lost-wax metal casting, thread guides, cutting tools, welding nozzles, and other small, high production parts. Excluding the obvious, that it is a good technique for very large volume parts, injection moulding has also proved to be an excellent technique for making components such as turbo charger rotors (see Figure 1) and thrust bearings, which would be too expensive if the parts were machined [1, 2, 3 and 4].

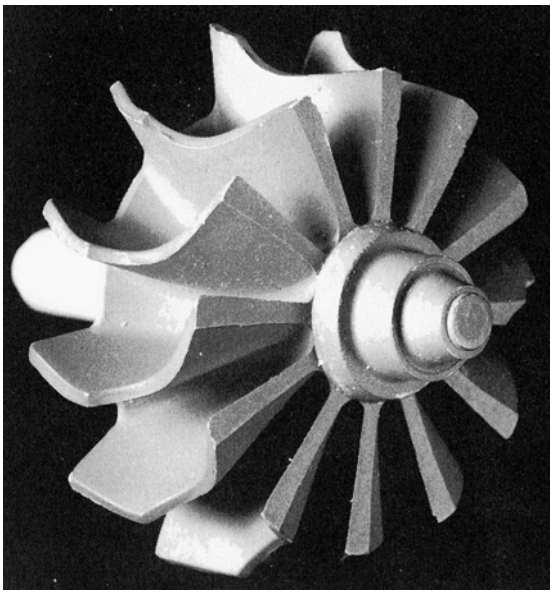

Figure 1. Turbocharger rotor.

Low-pressure injection moulding (LPIM) provides an excellent option for producing ceramic components using low cost tools in comparison to high pressure moulding techniques [5, 6, and 7]. The LPIM process enables fabrication of very complex shapes as well as simpler components. The essence of the process is that parts can be produced with a higher level of integrated function to meet the customers needs than other process.

Injection moulding process consists of four steps:

(1) Mix preparation;

(2) Moulding process;

(3) Binder removal;

(4) Sintering.

II Mix preparation.

Mixing a large fraction of ceramic powder with a much smaller fraction of organic binder can create a moldability problem. The flow characteristics of the mix, its subsequent moldability, and the quality of the final parts all depend on the homogeneity of the mix, so the preparation of the mix is a key factor. Preparation of the mix consists of the incorporation of a ceramic powder in an organic binder. This is typically accomplished in a sigma/Z-blade or other high-intensity mixer. The proper mixing procedure must result in the homogenization, de-agglomeration, and dispersion of the ceramic powder and of the minor organic additives in the major binder [1].

Binder systems can be classified into several general categories, which include thermoplastics, thermosets, sublimable organics and chemical gelation (e.g., ethyl silicate) [8, 9, 10, and 11]. The objective of batch formulation is to maximize the solids loading in a homogenous mix, in order to preserve the component strength after debinding and to achieve uniform shrinkage during sintering [12]. In addition to reduce costs and burnout time, a low binder content aids in controlling dimensional variation during binder burnout, in reducing shrinkage during sintering, and in attaining a high sintered density [12].

In a study of a variety of thermoplastic binder systems (ceramic powder-polymer system), it was concluded that such systems should possess three flow characteristics:

- a shear thinning behaviour,
- a fluidity (inverse of the viscosity) greater than 10 $(Pa.s)^{-1}$ at a shear rate of about 100 (sec^{-1}),
- a relatively low dependence of the viscosity on temperature at a given shear rate [1].

Almost all the natural and synthetic organic compounds that are commercially available have been tried as binders and are covered by patents. The objective is to achieve mixes that do not separate, but flow freely during moulding, can be readily removed from the mould without sticking, and burn out from the moulded shape without causing it to crack or rupture. The primary role of organics is to help flow of powder during injection and to provide mechanical strength before thermal treatment. Typical components include:

- a major binder which provide strength; fluidity; wetting; stability; easy burn-out. In addition it must be of low cost ;
- a minor binder (creation of controlled porosity for gas escape in debinding),
- non-reactive, non-volatile plasticizers,
- other aids: surfactants, mould-release agents, and dispersants [13, 14].

In general, the smaller the particle size, the higher the viscosity of the injection moulding mixes. Broad (multimodal) distributions are generally preferred over narrow distributions to reduce the viscosity of the mix. The coarser the powder, the higher the viscosity of the binder needed to achieve good injection moulding. At least two reasons can be cited for this: enhanced settling and higher permeability. If particle sizes are widely distributed, the viscosity coefficient of the mix generally decreases at the same solid loading. The effect of powder agglomeration on viscosity is not clear. However, the powder must be de-agglomerated for perfect homogenization. Soft agglomerates create problems in mixing. Hard agglomerates create problems in every stage of processing. A good powder that is free of agglomerates is essential to make a good mix. It is suggested that mixes be prepared (developed) specifically for the injection moulding jobs, and NOT adapted from another process [15, 16 and 17].

III The moulding process.

The moulding process begins when the granulated mix is loaded into the injection moulding machine. Injection moulding machines consist of two basic parts, an injection unit and a clamping unit.

Injection Unit

The injection unit melts the polymer resin and injects the polymer melt into the mould. The unit may be ram fed or screw fed, (see Figure 2). The reciprocation screw injection

moulding machine is the most common injection unit used. The screw rotates and axially reciprocates. A hydraulic motor produces rotation and acts to melt, mix, and pump the polymer. A hydraulic system controls the axial reciprocation of the screw, allowing it to act like a plunger, moving the melt forward for injection. A valve prevents back flow of the melt from the mould cavity [1, 18, and 19].

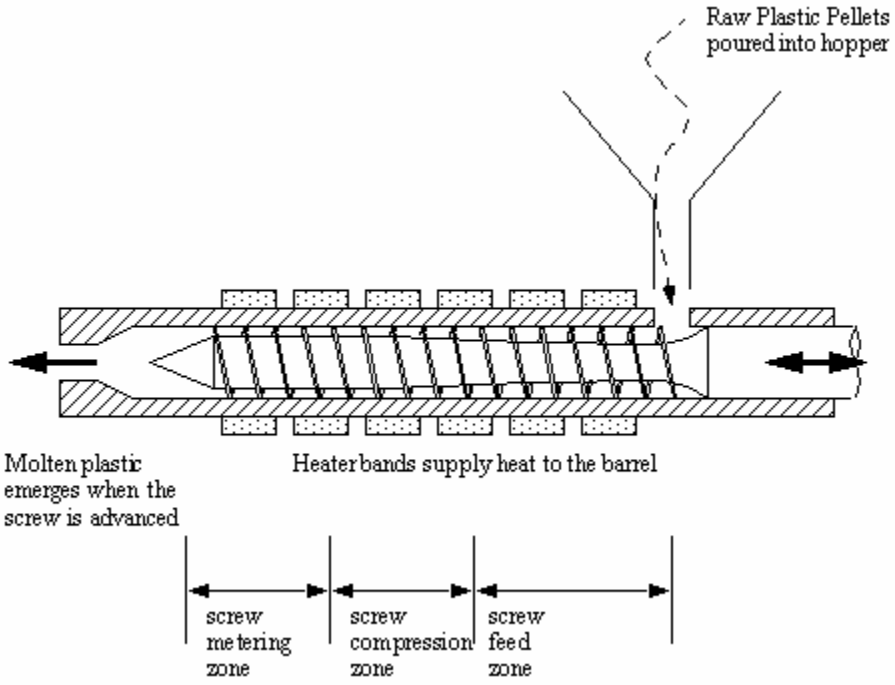

Figure 2. Extruder used for injection of the paste into the mould. [18].

Clamping Unit

The clamping unit holds the mould together, opens and closes it automatically, and ejects the finished part. The mechanism may be of several designs, mechanical, hydraulic or hydro-mechanical. Air is then evacuated from the mix to eliminate voids, and the heated mix is shot into a cold die. The mix fills the cavity and, on cooling, sets in the form of the die. The part is ejected from the die and the process is repeated. The piece will cool down to a temperature where it becomes sufficiently rigid so that it can be ejected without any deformation. Once the piece is ejected, the mould is closed and the piece cools slowly at room temperature.

The time cycle of injection moulding is a compromise between throughput and set-up of the mix. Parts should be cold when they are ejected from the die. It is better to have the mould at as low a temperature as possible during mould filling to increase the density of the injection moulding mix and to minimize the shrinkage in the die during cooling. There is a

trade off between good fluid flow and shrinkage. The fabrication stages of any shaping technique must preserve the homogeneity of the compound in order to minimize the strength-limiting defect size [1].

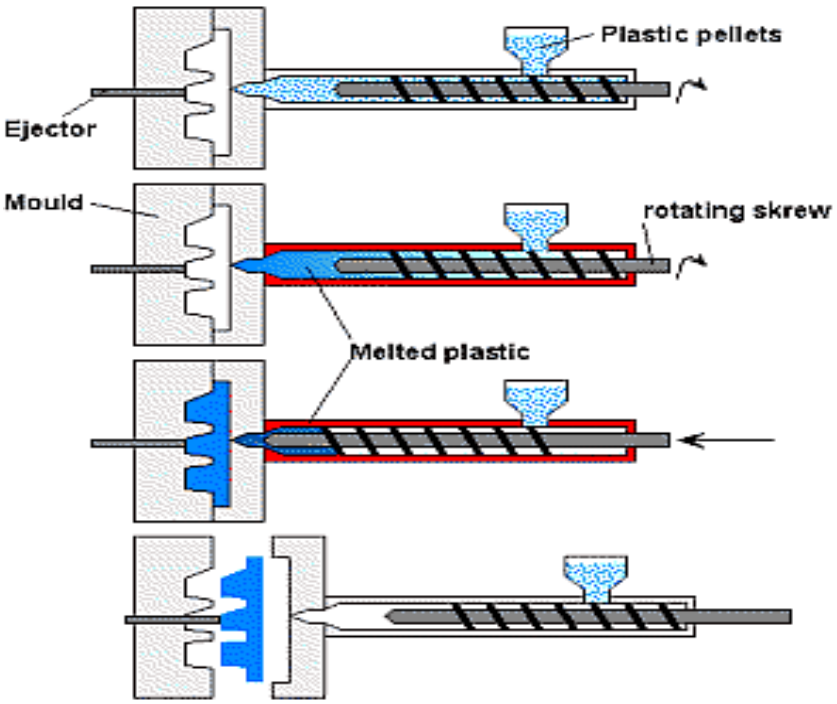

Figure 3. The moulding process [19].

Accordingly, in injection moulding, the number and size of defects should be minimized at all stages of manufacturing. Injection moulding involves simultaneous heat transfer and fluid flow. In the end, this combination of transport mechanisms leads to a host of problems, including defects such as knit lines, sink marks, short shots, excessive shrinkage, flashing, jetting, and others. It is therefore desirable to separate the two transport processes, the mould filling step and the setting step from one another.

Defects typically include:

- Incomplete mould filling. Weld lines result from low fluidity, low temperatures, low injection speed or pressure, or improper gate location.
- Cracks and voids result from non-uniform shrinkage, especially when the last liquid inclusion solidifies in the centre of the piece, but also if extensive orientation of polymer chains takes place.
- If temperatures are too high, flashing and sink marks are encountered. If temperatures are too low, short shots, knit lines, and jetting occur.

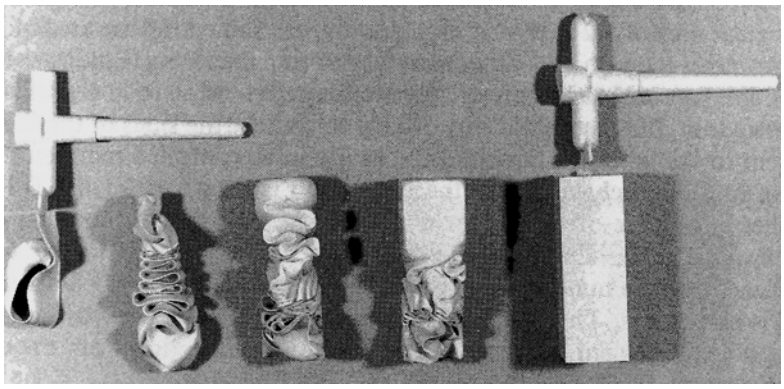

Figure 4. Knit lines [1].

IV Binder removal.

Binder removal is probably the most important and most difficult step in the injection moulding process. Binder removal is basically a diffusion problem and is analogous to drying. It is affected by the particle size of the powder, the packing arrangement of the powder, the viscosity and vapor pressure of the binder(s), the temperature, and the gas pressure in the binder removal chamber. It is here that many defects are generated, including pores, cracks, laminations, pin-holes, "orange peels", and others. Binder removal involves the elimination of the binder from the part that was added in the mix preparation stage to make the mix flowable. Binder removal is typically accomplished in two steps:

1. The bulk of the binder is removed, either by direct sublimation or by evaporation of the main constituents of the organic vehicle, or by capillary suction into a high-surface-area packing powder such as carbon black, hydrated alumina, or silica.
2. The remainder of the binder (5-10 %) is removed in the early stages of the sintering cycle. Thick and thin sections in single part present significant problems. For most of the commercial injection moulding technologies, binder removal is essentially a diffusion-controlled process.

Thick sections require more time to remove the binder than thin sections, because the time for removal is proportional to the thickness squared. Therefore, by the time the thick section has had enough binder removed to be safe to put into the furnace, the thin sections are devoid of binder and are thus quite weak. One way to deal with this lack of mechanical strength is to use multiple binders, miscible with one another, and which can be removed at different temperatures.

V Sintering.

Sintering usually follows standard procedures established for similar pressed parts.

VI The advantages and disadvantages of injection moulding.

The advantages of injection moulding are high production rates, design flexibility, repeatability within tolerances, the ability to process a wide range of materials, relatively low labour costs, little or no finishing of parts and minimum scrap losses.

Disadvantages of injection moulding are high initial equipment investment (some moulds run into the millions of dollars!), and high running costs (accurate cost prediction for moulding jobs are difficult), part must be designed for effective moulding.

Injection moulding will continue to be attractive mainly for high production, high value-added parts in which the cost of mould design and construction and the long binder removal times can be justified.

Low pressure moulding offers significant processing advantages compared to high pressure technology PIM based on thermoplastic resins. Considerable cost savings can be made in component production as the machine and the moulds are lighter and less costly. This makes manufacturing small numbers of particular components economical, because the machine and mould costs are less significant than with high-pressure technology. Moulds for low pressure processing are generally made from aluminium/steel. Other benefits of low pressure processing are: reduced anisotropy in moulded components, lower energy requirements, reduced machine and mould wear, lower mould costs, reduced processing equipment costs, increased flow path, more complex geometries – thinner wall sections, larger components, wider component design capability [20].

The most significant advantage of low pressure processing is the ability to make large mouldings. Low viscosity compositions do not need such a robust mould as high pressure/high viscosity PIM systems. As a result, a wide range of product sizes is possible using low-pressure injection moulding. Component size and mass range from 100μm to lm in length and from 0.1g to 50kg, with a tolerance of better than +/-0.15% in a given dimension.

VII This work.

Processing of ceramics is a major research topic of the SPCTS laboratory where this work was conducted. Rheological characterization of a paste is a prerequisite to master a forming process such as extrusion or injection moulding and this was one of the pursued objectives. The other, more ambitious, prospect was to relate these properties to the physico-chemical composition. This is possible if other complementary techniques are used such as DSC, SEM or sedimentation tests among others. The studied paste, comprising several organic components: paraffin (≈28%), EVA (≈8%), carnauba wax (≈4%), stearic acid (<1%) and loaded with a zirconia submicronic powder (60%vol.) was found adequate for injection moulding in a previous study [21]. Starting from this initial composition, several parameters were modified, first of all the solid content (from 0 to 60%vol.) but also the polymer's blend composition and the nature of the material (ZrO_2, Al_2O_3, SiC).

The document is organized along the following lines:

Chapter I present the raw materials used and the mode of preparation of the paste.

Chapter II focus on rotational rheometry. This technique allows a detailed study of the rheological behaviour of the paste although it is limited to shear deformation. The different techniques used are presented: flow curves, oscillation, creep and relaxation experiments. Results obtained for different solid fractions and different polymer's blend compositions are presented and discussed.

Chapter III is devoted to capillary rheometry. It permits to extend the range of applied stresses covered by rotational rheometry but is also one way to investigate the extensional properties (Cogswell's analysis). The basic equations are derived and the possible artefacts are described. Results are obtained for the basic composition suitable for injection.

In chapter II and III only paste loaded with Y-doped zirconia have been studied.

Chapter IV - the results obtained for different materials are presented and discussed. Finally, the effect of temperature is taken into consideration (125°C-135°C).

Bibliography.

[1] - B.C. Mutusuddy, R.G. Ford, "Ceramic injection molding", Chapman and Hall, UK, (1995).

[2] – H. Belofsky, "Plastics: Product design and process engineering", Hanser Publishers, Munich, Vienna, New York (1995).

[3] – C.G. Gogos, Z. Tadmor, "Principles of polymer processing", John Wiley & Sons, New York (1979).

[4] - S. Middleman, "Fundamentals of polymer processing", McGraw-Hill Book Company, New York, (1977).

[5] - R. Lenk, A. Ph. Krivoshchepov, "Effect of surface active substances on the rheological properties of silicon carbide suspensions in paraffin". J. Am. Ceram. Soc. 83 (2), p.273-276, (2000).

[6] - J. E. Zorzi, C. A. Perottoni, J. A. H. Jornada, "Hard-skin development during binder removal from Al_2O_3-based green ceramic bodies". J. Mater. Sci. 37 (9), p.1801-1807, (2002).

[7] - http://www.dynacer.com/Injection_Moulding.htm

[8] – J. G. Zhang, J.R.G Evans, "Predicting the viscosity of ceramic injection moulding suspensions" J. Euro. Ceram. Soc., 5, p.165-172, (1989).

[9] – A. Johnosson, E. Calstrom, L. Hermansson, R. Carlson, "Rate-controlled thermal extraction of organic binders from injection-moulded bodies" Adv. Ceram., 9, p.241-245, (1983).

[10] – B.K Lograsso, A. Bose, B.J Carpenter et al. "Injection moulding of carbonyl iron with polyethylene wax", International Journal of Powder Metallurgy, 25, p.337-348, (1989).

[11] – R.W Ohnsborg, US Patent Nov.11, 4, p.233-256, (1980).

[12] - C. Toy, Y. Palaci, T. Baykara, "New ceramic thread-guide composition via low-pressure injection molding", J. Mat. Process. Tech. 51 (I -4), p.211 -222, (1995).

[13] – B. Lanteri, H. Burlet, A. Poitou, I. Campion, "Rheological behavior of polymer-ceramic blend used for injection molding." J. Mat. Sci., 31, p.1751-1760, (1996).

[14] – C. Lanos, "Méthode d'identification non viscométrique de comportements de fluides", Thèse, Institut National des Sciences Appliquées de Rennes, (1993).

[15] – R.M. German, “Powder injection molding” MPIF, Princeton, New Jersey, (1990).

[16] – J.D. Jeffrey, A. Acrivos, “The rheological properties of suspensions of rigid particles” AIChE J 22, p.417-432, (1976).

[17] – R. M. German, A. Bose, “Ceramic injection molding”, Chapman & Hall, London, vol. 1, p.11-131, (1997).

[18] - http://claymore.engineer.gvsu.edu/~jackh/eod/manufact/manufact-213.html

[19] - http://www.dogma.org.uk/vtt/process/processes/injectionmoulding.html

[20] – M. Martin, Materials World 7(2), p.71-75, (1999).

[21] – E. Delhomme "Déliantage par CO_2 supercritique de matériaux céramiques réfractaires mis en forme par injection basse pression" Thèse de l'Université de Limoges (France), (1991).

Chapter one: Materials and preparation of the paste.

I The components.

I.1 The powders.

I.1.1 Alumina (Al_2O_3).

Alumina is the most common raw material used for the elaboration of technical ceramics.

The powder used in this study is the grade A16-SG alumina (ALCOA Chemicals-USA). It is a low-soda, high-purity, ultrafine α-Al_2O_3 powder (X-Ray Diffraction pattern shows only this phase [1]) with a density of 3950kg/m^{3*}. The chemical composition is given in Table 1.

Chemical composition	**wt%**
Al_2O_3	99.8
Na_2O	0.06
Fe_2O_3	0.02
SiO_2	0.03
CaO	0.02
B_2O_3	0.003
MgO-added during grinding	0.03

Table 1. Chemical composition of used powder.*

The granulometric distribution* ranges between 0.05 and 20 µm, with two maxima at 0.2 µm and 1.5 µm (average diameter of 0.4 µm), see Figure 5.

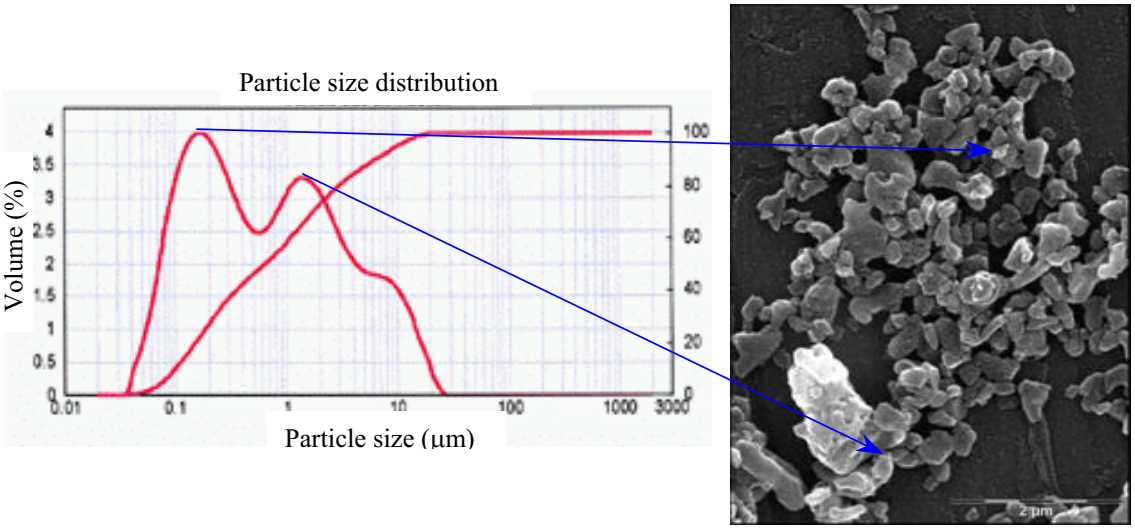

Figure 5. Granulometric distribution and SEM picture.

* According to the producer.
* liquid environment, ultrasonification 5 min.

The specific surface of this powder, S_V, determined by the BET method, is equal to 9.5 m^2/g*. The apparent radius ($\frac{3}{\rho S_v}$) is equal to 0.08 µm and it is concluded that the powder is agglomerated.

I.1.2 Silicon carbide (SiC).

Silicon carbide is a synthetic material with an outstanding hardness, only superseded by diamond, boron nitride and boron carbide. The chemical inertness to most of the alkaline and acids in combination with its excellent heat and abrasion resistance makes silicon carbide very suitable under extreme operation conditions.

The powder used in this study is the grade FCP 13C SiC (SIKA NORTON A.S). The X-Ray Diffraction pattern shows only the pure α-SiC phase [1]. The density is reported as 3200 kg/m^3 *

Chemical composition	wt %
SiC	98.06
Si	0.63
SiO_2	0.57
C	0.25
Fe	0.16
Al	0.23
CaO	0.05

Table 2. Chemical composition of used powder. *

The granulometric distribution* ranges between 0.2 and 8 µm, with two maxima at 0.3 µm and 2.5 µm (average diameter of 2 µm), see Figure 6.

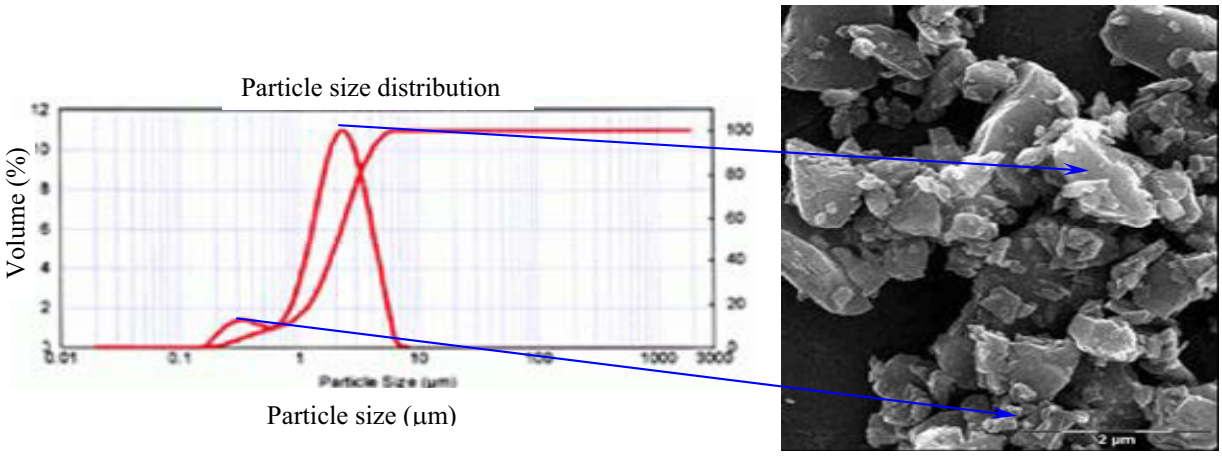

Figure 6. Granulometric distribution of the SiC powder and SEM picture.

* According to the producer.
* liquid environment, ultrasonification 5 min.

Figure 6, shows a general view of the grain's shape obtained by SEM. The BET specific surface area, of the powder S_V, is 15 m^2/g.* The apparent radius ($3/(\rho S_v)$) is equal to 0.065 μm and it is concluded that the powder is agglomerated.

I.1.3 Zirconia (Y-ZrO_2).

Zirconia is a unique advanced ceramic material. As a technological breakthrough, YSZ surpasses the strength limitations of traditional fine ceramics. Heat insulating properties and oxygen-ion conductivity indicate zirconia has potential for use in a wide variety of applications.

The powder used is the grade TZ-3YS (Tosoh, Japan). The density is equal to 6050 kg/m^3 *. X-Ray diffraction pattern, (see Figure 7) shows the presence of two phases, the tetragonal and the monoclinic ones [1]. i.e., this is a partially stabilized zirconia in agreement with the dopant content (3 mol % yttria).

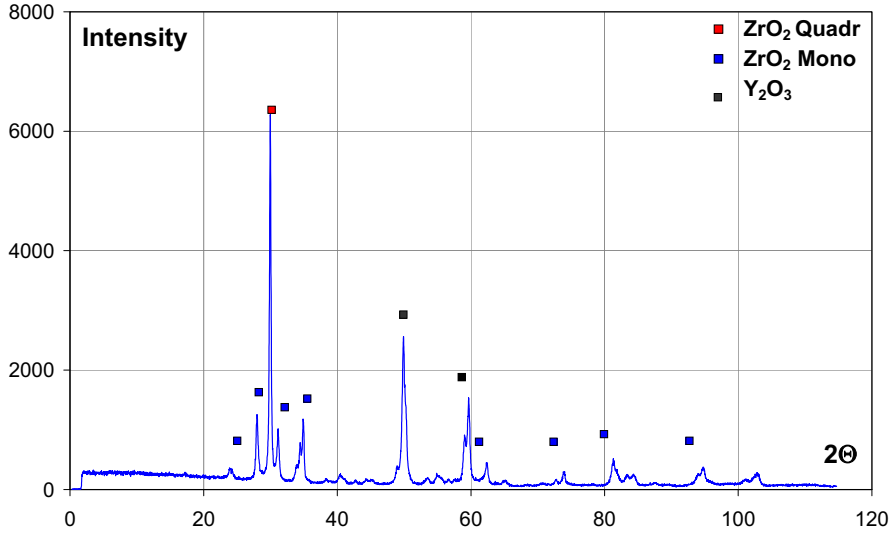

Figure 1. X-Ray Diffraction pattern of the zirconia powder used in this study.

The chemical composition is detailed in Table 3:

Chemical composition	wt%
$ZrO_2 + HfO_2$	94.7
Y_2O_3	5.0
Fe_2O_3	0.07
SiO_2	0.05
TiO_2	0.08
Na_2O	0.03
CaO	0.06

Table 3. Chemical composition of used powder*.

* According to the producer.

The granulometric distribution* ranges between 0.2 and 80 µm, essentially one maximum at 3 µm, see Figure 8.

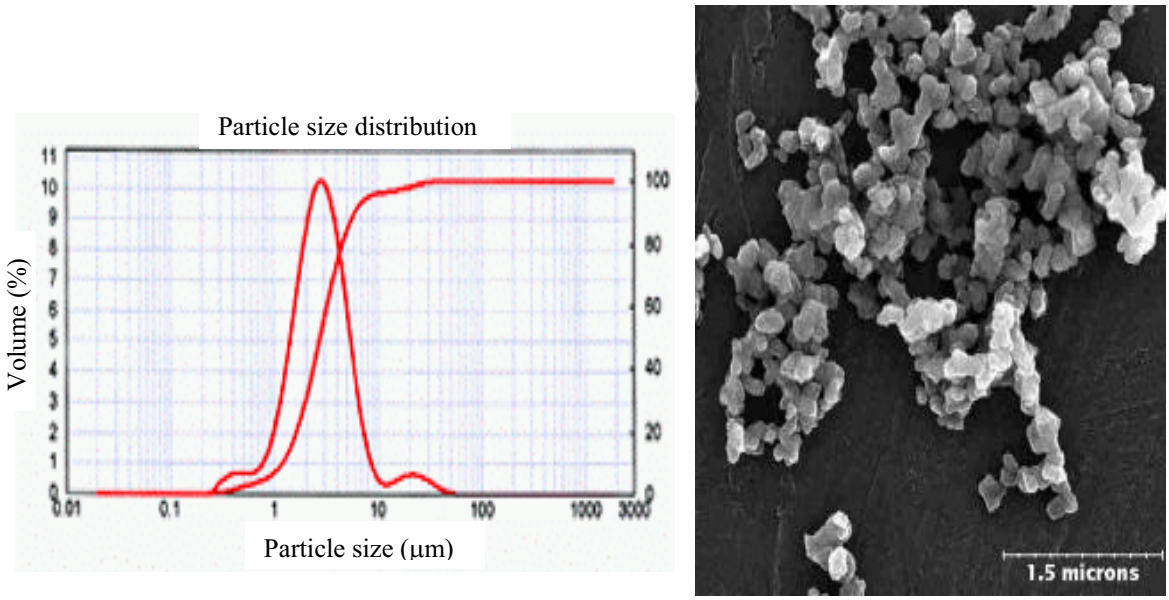

Figure 8. Granulometric distribution and SEM picture of the zirconia powder.

The specific surface area is equal to 7 m^2/g*. The apparent radius, $3/(\rho S_v)$ is equal to 0.07 µm and it is concluded that the powder is agglomerated. Confirmation is given by SEM observations, see Figure 8.

I.2 The organic components.

I.2.1 Paraffin.

Paraffin, consists mainly of a mixture of saturated straight-chain solid hydrocarbons with general formula C_nH_{2n+2} where n is an integer between 22 and 27 [2].

The grade used in this study is paraffin 62/64 6J109N/10 (France). Its density is 900 kg/m^{3*} and the molecular weight M is equal to 260 mol/g*. At room temperature this is a solid and the X-Ray diffraction pattern, see Figure 9, shows that it is partially crystallized [3].

* voie liquide, ultrasonification 5 min.
* According to the producer.

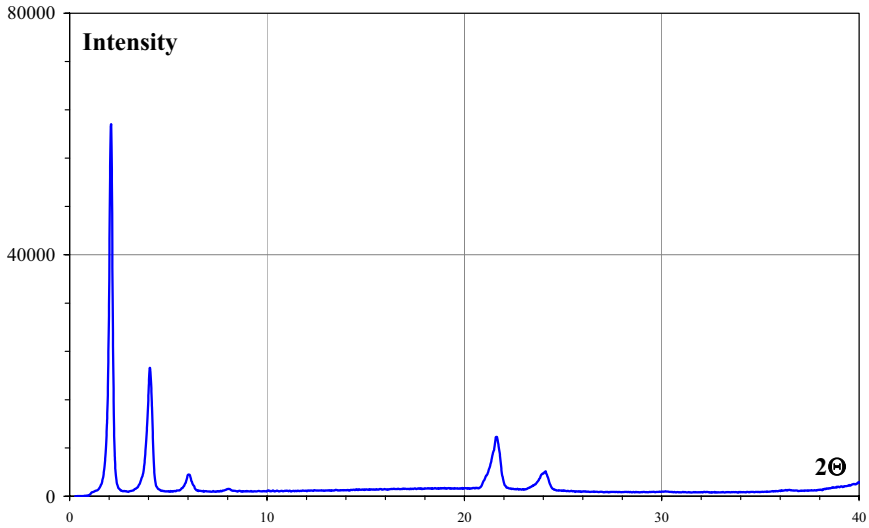

Figure 9. X-Ray diffraction pattern of the paraffin 62/64 6J109N/10.

A DTA analysis, see Figure 10, shows that melting covers a wide temperature range from 35 to 72°C with a maximum at 64°C, reflecting its complex composition.

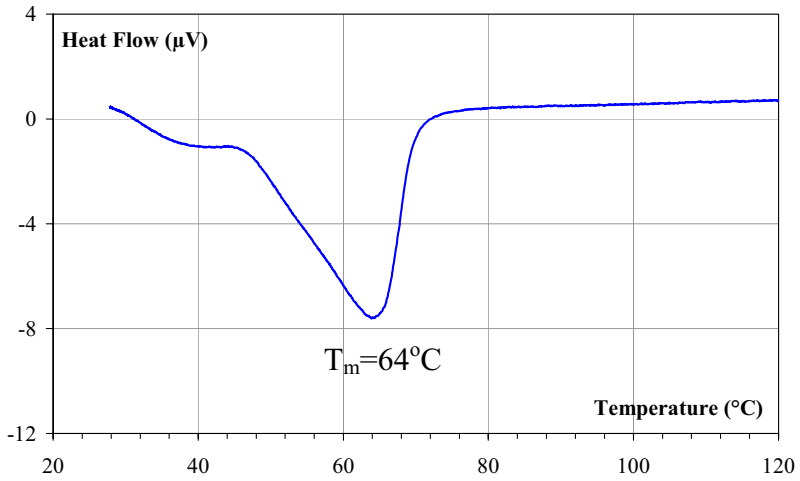

Figure 10. DTA analysis of paraffin 62/64 6J109N/10. Heating speed – 2°C/min.

I.2.2 Ethyl Vinyl Acetate.

The Ethyl Vinyl Acetate (EVA) is a chemical copolymer with repeating ethylene groups and acetate functional.

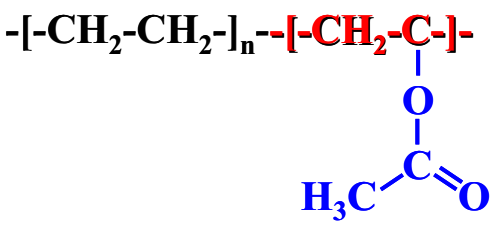

The polar functional groups reduce the crystallinity, increase the chemical reactivity and has a strong affinity to polar solid surfaces. [4].

The grade used in this study is ESCORENE^{TM} ULTRA (FL 00309) fabricated by Exxon Mobil Chemicals, Belgium. It contains 9.4 wt% of Vinyl Acetate*. The density is equal to 930 kg/m^3 and the molecular weight is M= 60000 mol/g *. At room temperature, this is a partially crystallised solid. A DTA analysis, see Figure 11, shows the presence a main peak at 96°C which correspond to EVA 9.4 wt.%. A small peak is observed at 48°C, melting temperature of Pure vinyl acetate*.

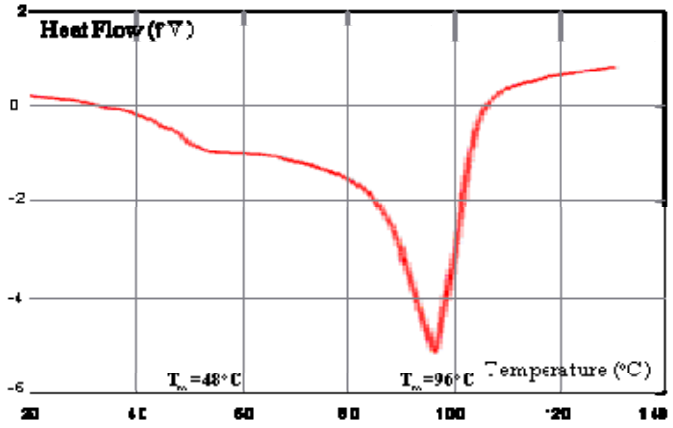

Figure 11. DTA analysis of EVA. Heating speed – 2°C/min.

I.2.3 Carnauba Wax.

Carnauba wax is the coating on the surface of the leaf of a particular palm tree. Leaves of this fan palm are removed individually from the tree, cut and shredded, and then dried, so that wax flakes off. A pound of carnauba wax is obtained from about 20 leaves. This powder is melted, strained, and then moulded into blocks. Because of its strong grain structure, it is the hardest natural wax known to man. It contains mainly wax esters (85%), accompanied by small amounts of free acids and alcohols, hydrocarbons and resins. The wax esters comprise C_{16} to C_{20} fatty acids linked to C_{30} to C_{34} alcohols, giving C_{46} to C_{54} molecular species [5]. The density is 1000 kg/m^{3*}and the molecular weight M= 700-900mol/g.

The grade used in this study is Carnauba wax T3 commercialized by Barlocher (France). Its chemical composition is detailed in Table 4.

Acid Value (wt. %)	3-6
Alcohols (wt. %),	10-15
Ester value (wt. %)	80-85

Table 4. Chemical composition of carnauba wax T3.

* According to the producer.

At room temperature, this is a partially crystallised solid, see Figure 12 [3].

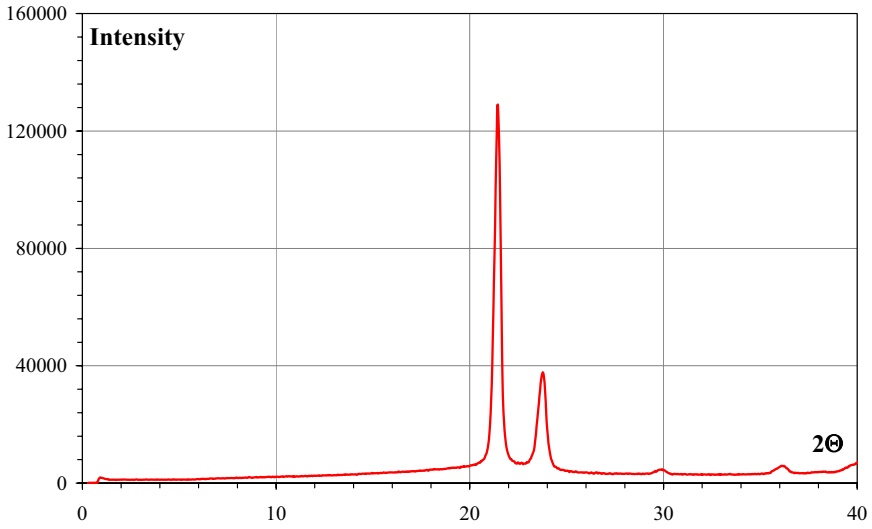

Figure 12. X-Ray Diffraction pattern of carnauba wax T3.

A DTA analysis, see Figure 13, shows the presence of a dissymmetric peak with a maximum at 84,7°C corresponding to the melting of the wax.

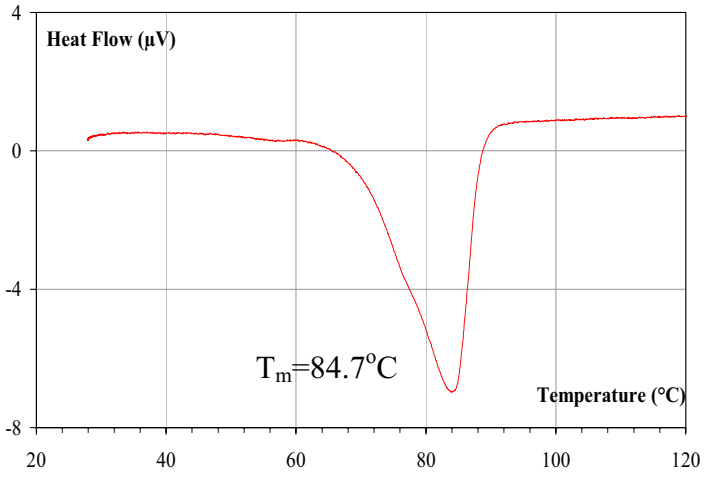

Figure 13. DTA analysis of carnauba wax. Heating speed – 2°C/min.

I.2.4 Stearic Acid.

Stearic acid is a typical example of a fatty acid, which is essentially a long hydrocarbon chain with a carboxyl group at one end and a carboxylic acid group at the other. It is a saturated acid, since there are no double bonds between neighbouring carbon atoms.

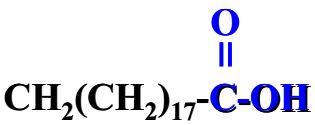

This means the hydrocarbon chain is flexible and can roll up into a ball or stretch out into a long zig-zag.

The grade used in this study CAS 57-11-4 is fabricated by ALDRICH (Germany) and commercialised by Merck (Index 13, 8882). Its purity is greater than 95 %* and remaining comprises essentially saponifiable substances such as methyl ester. The density is 940 kg/m^{3}* and the molecular weight M= 284.5 mol/g*. At room temperature, it is a partially crystallised solid as proved by its X-Ray diffraction pattern; see Figure 14 [3].

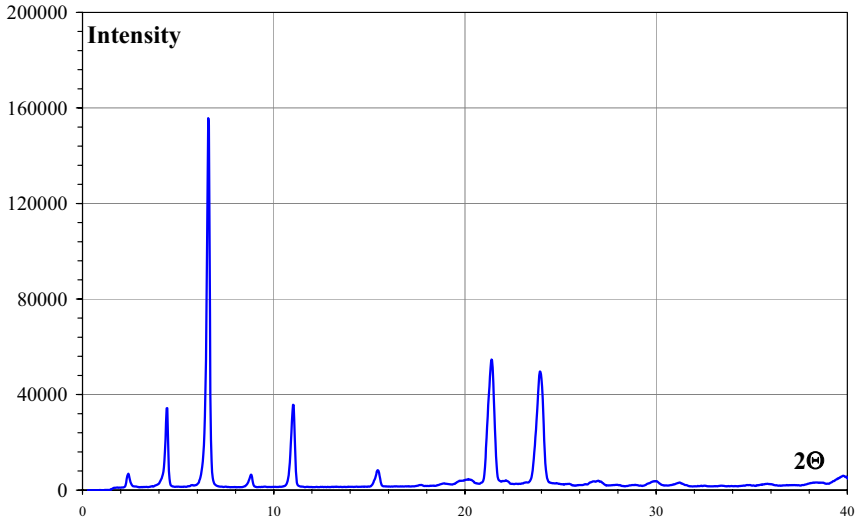

Figure 14. X-Ray Diffraction pattern of Stearic acid.

Melting occurs at 70°C, see the DTA analysis depicted in Figure 15.

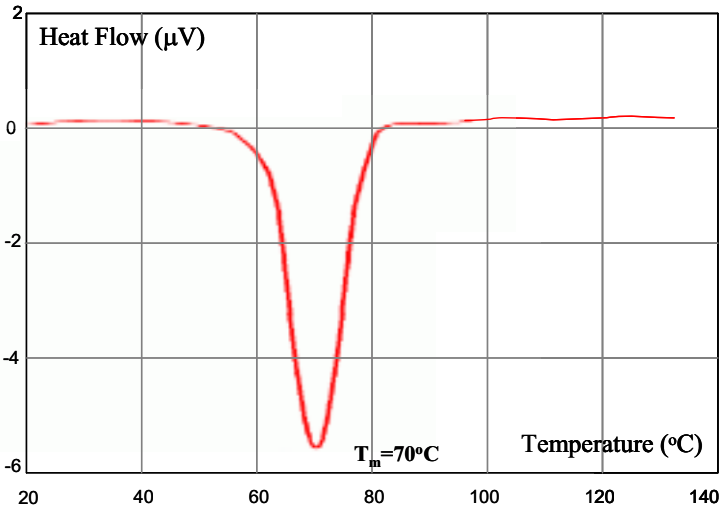

Figure 15. DTA analysis of stearic acid. Heating speed – 2°C/min.

* According to the producer.

I.3 Immiscibility aspect.

At 130°C, temperature of the process, all organic components are liquid but their compatibility with one another is not known. Four blends were prepared (Par+EVA, Par+Car, EVA+Car, EVA+Par+SA) and submitted to a DTA analysis, see Figure 16.

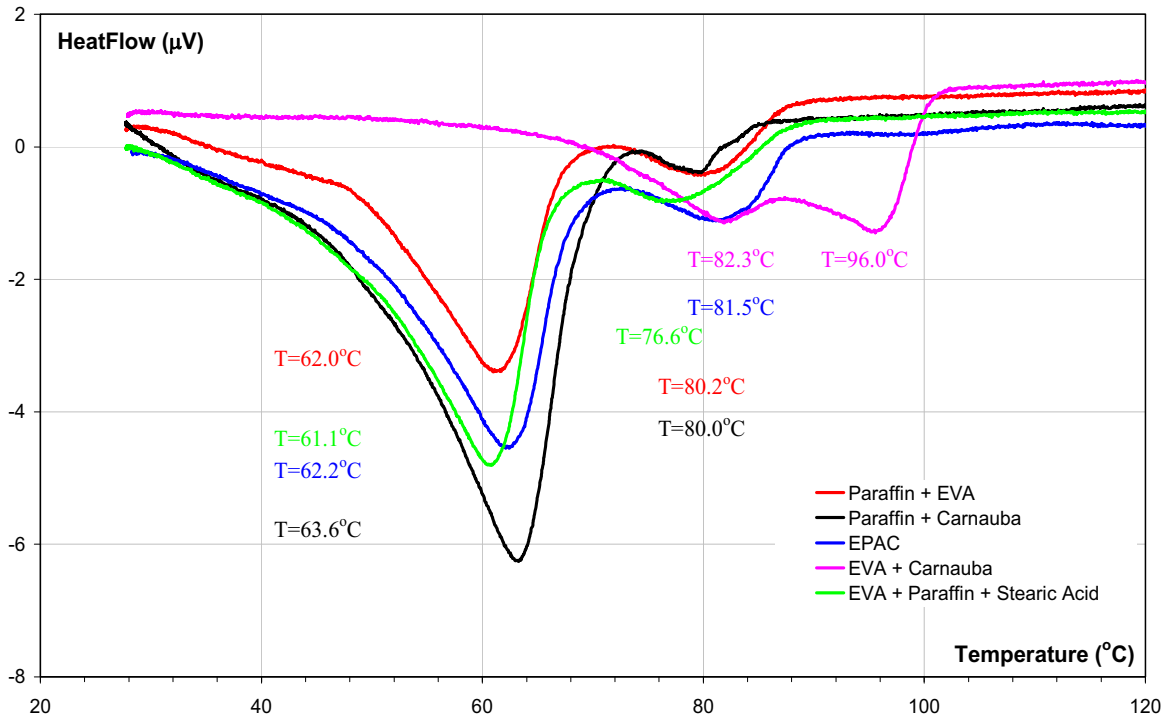

Figure 16. DTA Analysis of different blends.

As a general remark, in the case of a pair of components, the DTA curve presents always two maxima, which indicates the presence of two phases. This immiscibility was also seen in SEM observations at room temperature, see Figure 17.

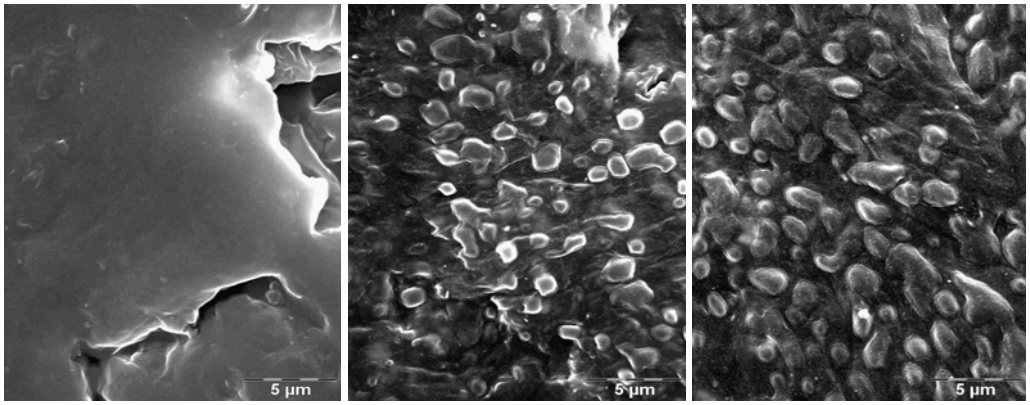

Figure 17. Coalescence of polymer's liquid drops. A. Initial state. B – 3 hours of rest at 130oC, C –5 hours of rest at 130°C.

Immiscibility does not mean no interaction, see Table 5:

Paraffin wax	T_m=64.0°C	**Carnauba wax**	T_m=84.7°C	**EVA**	T_m=96.0°C
Par+ Car	T_m=63.6°C	**Car + Par**	T_m=80.0°C	**EVA + Car**	T_m=96.0°C
Par + EVA	T_m=62.2°C	**Car + EVA**	T_m=82.3°C	**EVA + Par**	T_m=80.2°C

Table 5. Melting temperatures deduced from DTA analysis (Figure 16).

EVA and carnauba wax appear to be totally immiscible. In the same way, paraffin is not particularly affected by the presence of the other components. On the other hand, the melting temperature of EVA is decreased in presence of paraffin although the paraffin peak is not strongly modified. This shows some compatibility of EVA and paraffin but a limited miscibility.

Selective dissolving test does not allow to separate each phase from other.

II Preparation procedure.

II.1 Preparation of the powders

It has been noticed that the powders are agglomerated, in particular the zirconia powder. In order to promote de-agglomeration, the following procedure was adopted:

Preparation of the mixture: powder + dispersant in alcohol (ZrO_2, SiC, Al_2O_3 + C213 - ester phosphoric) or water (Al_2O_3 + DarvanC). All powders are mixed in a planetary mill during 3-4 hours.

- Drying through atomization. This technique makes it possible to avoid any segregation of the components of the suspension at the time of drying. The machine used, is an apparatus BUCHI 190 mini Spray Dryer, see Figure 18.

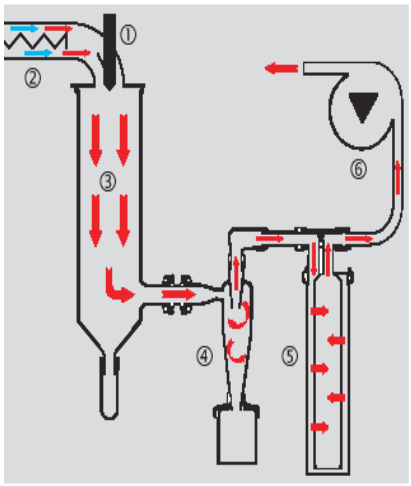

1 - Two-fluid nozzle, operated by compressed air to disperse the solution into fine droplets.
2 - Electric heating of the drying medium.
3 - Spray cylinder for drying the droplets to solid particles.
4 - Separation of the particles in the cyclone.
5 - Outlet filter to remove fine particles.
6 - Aspirator for generating the flow.

Figure 18. Illustration of the Buchi mini Spray Dryer.

II.2 Preparation of the organic matrix.

All organic additives were melted at 130°C for 3-5 hours and thoroughly mixed with a propeller mixer during the next two hours until a good homogeneous alloy is obtained. During preparation of blend evaporation was evidenced, see Figure 19.

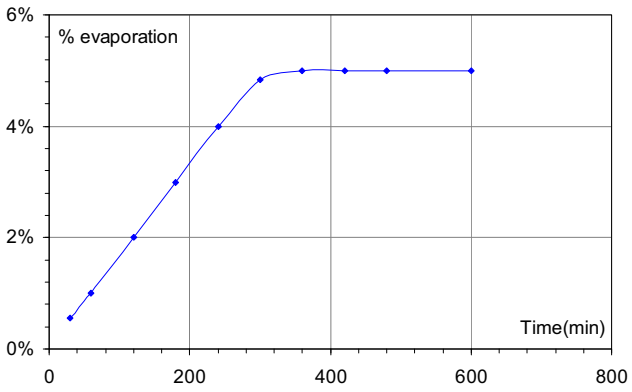

Figure 2. Evolution of the mass with the mixing time.

To eliminate this problem, in agreement with the results presented in Figure 19, the weight of the prepared blend was increased by 5%.

II.3 Preparation of the paste.

Two methods of preparation were selected:

- For low and medium solid fractions (in the range 2%-30% vol. of the powder) the paste was prepared in a LABO Reactor system.
- For higher solid fractions (40%, 50% and 60% vol. of the powder) the paste was prepared in a mixer with Z-blades and the powder being slowly added in the already melted organic phase (at 130°C).

Figure 19. Labo-Reactor System (on the left image) and mixer with Z-blades (on the right image).

Bibliography.

[1] – Powder Diffraction File – International Centre for Diffraction Data.

[2] - http://www.nationmaster.com/encyclopedia/Paraffin

[3] – Hanawalt Search Manual for Experimental Patterns.

[4] – http://www.specialchem4adhesives.com/tc/ethylene-copolymers/index.aspx?id=eva.

[5] – www.lipidlibrary.co.uk.

Chapter two : Rheological behaviour at low stresses (<500 Pa) using a rotational rheometer.

I Rheological background.

The rheological behaviours of the organic matrix and of the paste were investigated using a rotational rheometer (TA Instruments AR 2000) operated in the stress mode. It is designed to characterize the deformation induced by a shear stress. The extensional behaviour will be studied in chapter three.

I.1 The rotational rheometer, the apparatus and the principle of operation.

The AR 2000 rheometer is based on CMT (Combined Motor and Transducer) technology where the stress is input using an advanced non-contact induction motor, and the strain is measured with a highly sensitive optical encoder. The rheometer is capable of handling many different types of samples, using a wide range of geometry sizes and types.

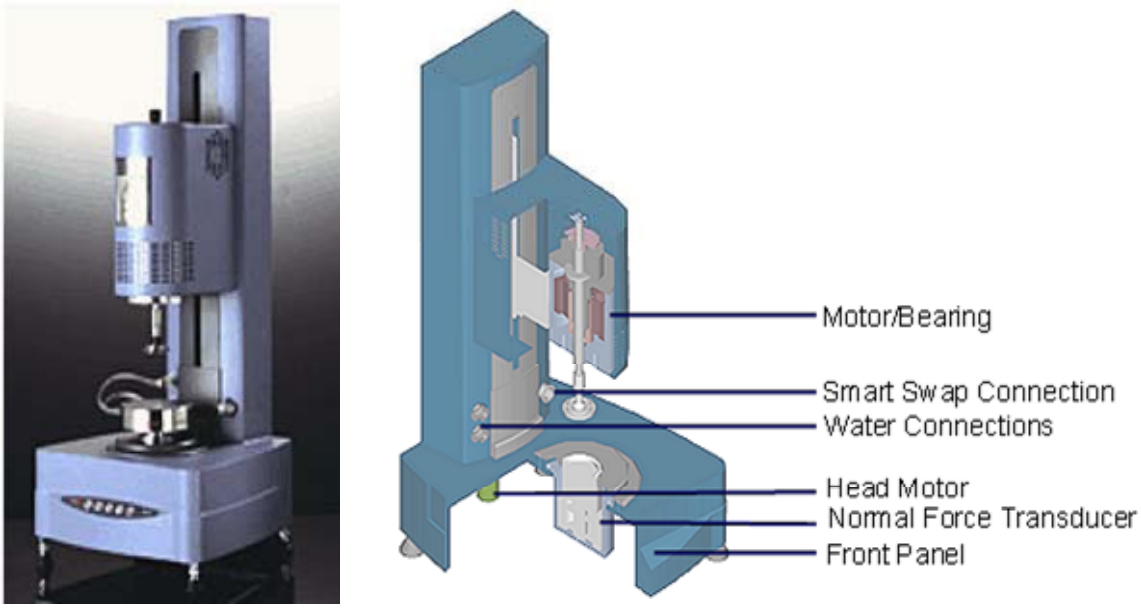

Figure 21. The TA AR 2000 rheometer.

The stress can be applied and released at will and an optical encoder device measures the angular displacement, down to 40 nanorad. The encoder consists of a non-contacting light

source and photocell arranged on either side of a transparent disc attached to the drive shaft. On the edge of this disc are extremely thin, accurate photographically etched radial lines. There is also a stationary segment of a similar disc between the light source and encoder disc. The interaction of these two discs results in a diffraction pattern that is detected by the photocell. The associated circuitry interpolates and digitizes the resulting signal to produce digital data which is directly related to the angular deflection of the disk, and therefore to the strain of the sample [1].

I.2 The measurement system.

Measurements were performed with a cone-plate geometry (radius 20 mm and cone angle of 1.6° in order to eliminate secondary flows) and plate-plate geometry (radius 10 mm). It is taken for granted that the sample has adhesion to surfaces and this was indeed the case in our experiments.

⇒ **Cone-plate geometry.**

A low angle cone rotates against a flat plate with the sample between them. A schematic of the system is shown in Figure 22. The shear rate and shear stress are given by [2]:

$$\dot{\gamma} = \frac{R \cdot \omega_o}{R \cdot \tan\alpha} \approx \frac{\omega_o}{\alpha}$$

$$\sigma = \frac{3M}{2\pi R^3}$$

where: ω_o is the constant angular velocity, α the cone angle, M-the applied torque, R – the radius of the upper plate.

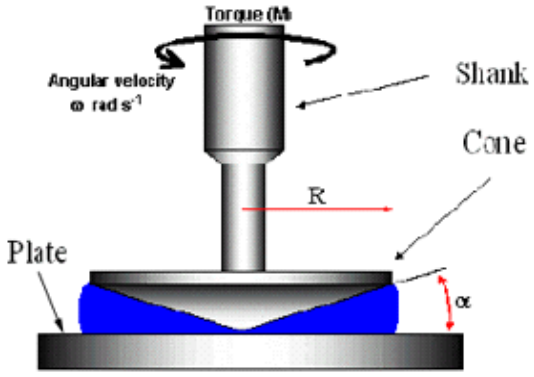

Figure 22. Cone-plate geometry.

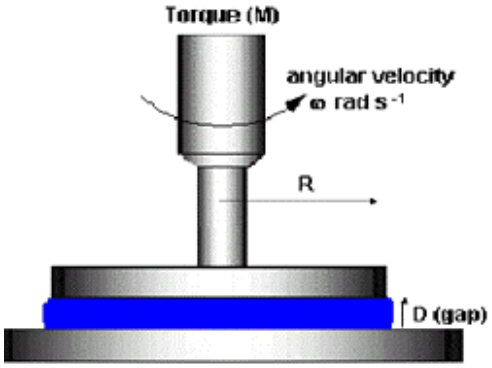

Figure 23. Plate-plate geometry. R- plate radius, D- gap thickness between plates.

⇒ **The plate-plate geometry.**

The gap, D, between the plates can be set to any distance which permits to avoid problems due to the finite particles size (D has to be greater than 5 to 10 times the size of the biggest particle). The main disadvantage of a plate-plate system is that the stress is not uniform in space. It depends on the radial coordinate r and it is solution of an integral equation :

$$\int_0^M dM = 2\pi \int_0^r x^2\,\sigma(x)dx$$

The shear stress and the shear rate are evaluated at the rim of the plate and are given by [2] :

$$\dot{\gamma}_R = \frac{\omega_o R}{D}$$

$$\sigma(R) = \frac{M}{2\pi R^3}\left[3 + \frac{dLn(M)}{dLn(\dot{\gamma}_R)}\right]$$

The bottom plate can be heated up to 200°C using a Peltier element. The measurements have been performed at 130°C most of the time. One problem encountered is the existence of a temperature gradient between the bottom plate (Peltier plate) and the upper plate (geometry surface). A trap was designed with a circulation of a caloric fluid inside the walls, the temperature of which could be controlled (±0.5°C), see Figure 24.

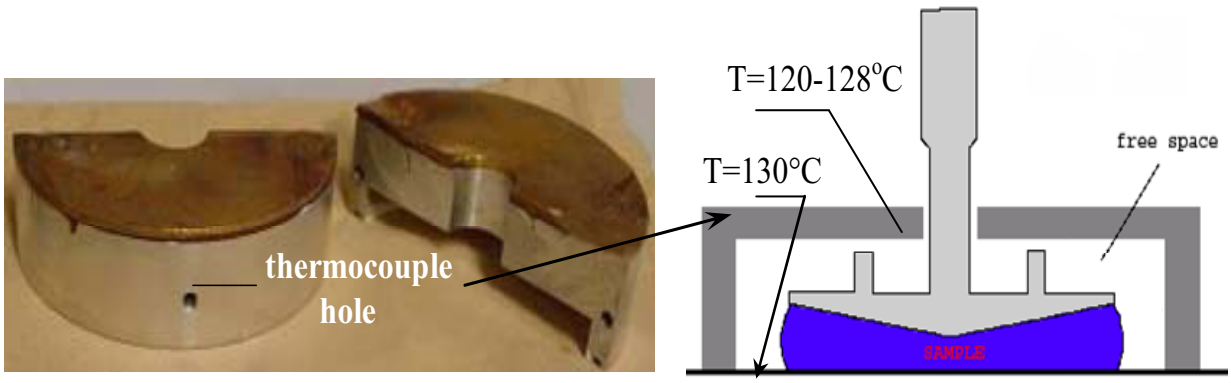

Figure 24. Temperature trap.

As shown in Figure 25, the temperature gradient across the trap was reduced to 2°C (less than 0.5°C across the sample).

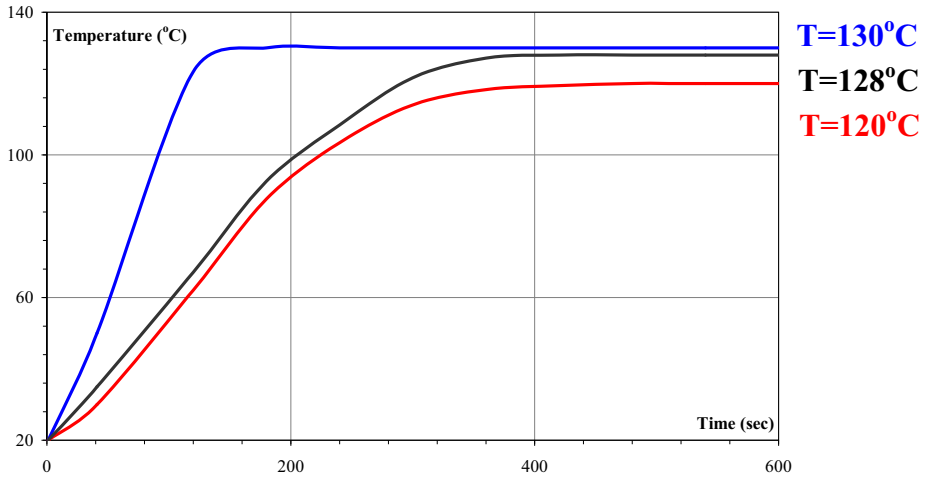

Figure 25. After a step increase to 130°C, evolution of the temperature of the Peltier plate (Blue line), and of the upper plate without (Red line) and with (Black line) circulation of fluid in the trap walls.

I.3 The measurements.

The simplest rheological behaviour is a linear relationship between stress and strain rate, the so-called Newtonian behaviour:

$$\sigma = \eta \dot{\gamma}$$

where η is the viscosity. Simple fluids (water, oil of low viscosity) obey this simple law but usually the behaviour is much more complicated. Two aspects can be investigated, the time evolution and the non-linearity of the rheological properties, although they are not always easily separable. Therefore, creep experiments (see below), performed at different levels of stress, were performed first, to define the conditions of a linear regime and estimate the time needed to establish a stationary state.

- **Nonlinear stationary behaviour (flow test)**.

A ramp of increasing torque is applied to the upper plate (the bottom plate is at rest) and the strain rate is recorded. The ratio $\sigma/\dot{\gamma}$ is called the apparent viscosity [3]. This ramp can be defined through an analog or a digital signal. The latter was used in all experiments [1]. The ramp is then a succession of steps, i.e. the time evolution can be followed for each value of

stress, which makes the procedure much more valuable. In this work a shear-thinning behaviour [3] has commonly observed, see Figure 26,

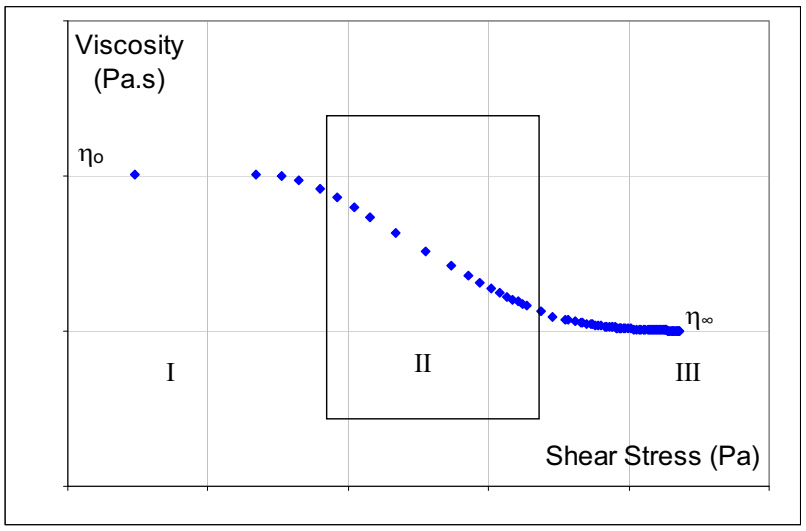

Figure 26. Flow curve – Shear-thinning behaviour of the typical fluid.

i.e. at low-enough shear stresses, the viscosity is constant with a value η_o (region I) but at some point it begins to decrease, and usually enters a straight line on a log-log plot, which can be expressed as a power-law behaviour (region II). At some point of the curve, a flattening out is seen and another stress region of constant viscosity is usually observed (region III). Thus we have two limiting Newtonian viscosities – η_∞ and η_o, separated by a power-law region. This behaviour is well described by a mathematical formula proposed by P.J. Carreau [4] which describes the whole curve:

$$\frac{\eta - \eta_\infty}{\eta_o - \eta_\infty} = \frac{1}{(1 + (K\dot{\gamma})^2)^{\frac{n}{2}}}$$

where: K-has the dimension of a time and n is-dimensionless

For highly loaded pastes, the stress must be higher than σ_c in order to promote flow, σ_c is called the yield stress. A simple relation has been proposed by E.C Bingham [2, 3] :

$$\sigma = \sigma_c + \eta_m \dot{\gamma}$$

where η_m is the dynamical viscosity.

- **Time evolution (creep and oscillation tests).**

We are now interested in the dynamics of the system. The simplest experiment is to apply a step increase of stress and to record the deformation as a function of time, what is

called a creep experiment [3]. One interesting advantage of this procedure is that it is applicable in the linear and in the non-linear regime. However a general mathematical theory for the interpretation exists only in the former case [5, 6], which will be detailed now.

In the case of a linear response, a response function f(x), characteristic of the material, can be used to describe the evolution of the strain induced by an imposed stress [3, 7]:

$$\gamma(t) = \int_{-\infty}^{t} \sigma(t')\ f(t-t')\ dt'$$

NB : Let us emphasize that in the case of a strain controlled rheometer, a different response function g(x) has to be used :

$$\sigma(t) = \int_{-\infty}^{t} \gamma(t')\ g(t-t')\ dt'$$

The relationship between f(x) and g(x) will be made clear later on.

- In the creep test,

$$\gamma(t) = \sigma_o \int_{0}^{t} f(x)\ dx$$

The ratio $\gamma(t)/\sigma_o$ is called the compliance, J(t) and f(x) can be obtained by derivation.

$$f(x) = \left.\frac{dJ}{dt}\right|_{t=x}$$

- In the oscillation experiment,

$$\gamma(t) = \sigma_o\ \exp(-j\omega t) \int_{0}^{+\infty} f(x)\ \exp(j\omega x)dx = \overline{\gamma}\ \exp(-j\omega t)$$

where a complex formalism has been used. In other words, the response to an alternating signal is an alternating signal of the same frequency (consequence of the linear regime), but displaced with a phase φ.

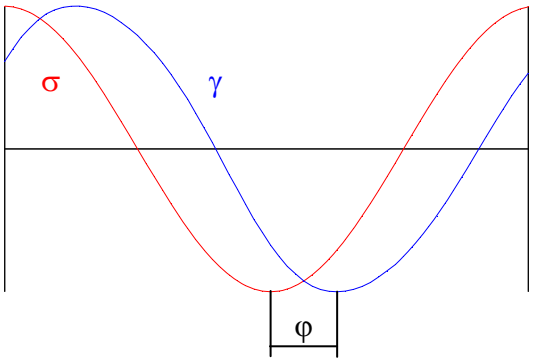

Figure 27. Phase lag between the recorded strain and the applied stress in the case of a sine wave signal.

The complex compliance $\bar{J}$ can be written:

$$\bar{J}(\omega) = \bar{J}' - j\,\bar{J}'' = \frac{\bar{\gamma}}{\sigma_o}$$

f(x) is then obtained through an inverse Fourier transform [8].

NB : In the case of a strain controlled rheometer, the same development can be made, introducing the modulus function G(t) defined as $\sigma(t)/\gamma_o$. It is easy to prove that

$$\bar{G}(\omega) = \frac{1}{\bar{J}(\omega)}$$

where $\bar{G}$ is the complex modulus. In the literature [9, 10], it is customary to plot and discuss the variations of the modulus with frequency, even in the case of a stress controlled rheometer.

It is concluded that both experiments, creep and oscillation, contain the same information, f(x), and therefore they may appear to be redundant. However, this is not the case because they do not operate in the same x-range, i.e., they are indeed complementary [3].

Quite often, f(x) can be described as a superposition of time constants τ :

$$f(x) = \int_0^{+\infty} F(\mathrm{Ln}\,\tau)\,\exp\left(-\frac{x}{\tau}\right) d(\mathrm{Ln}\,\tau)$$

F(Ln τ) being the time constant distribution function which can be continuous or discrete : $F(\mathrm{Ln}\,\tau) = \sum A_i\,\delta(\tau - \tau_i)$.

One reason is that it can be included in phenomenological equations, which describe the linear and nonlinear rheological behaviour, such as the Giesekus equation [11]. Then, the previous equations become :

- In the case of a creep experiment

$$J(x) = \frac{1}{G_0} + \frac{x}{\eta} + \sum_i A_i[1 - \exp(-\frac{x}{\tau_i})]$$

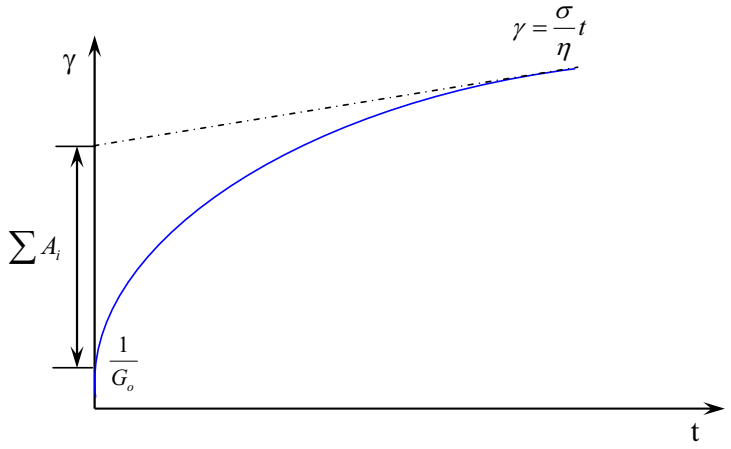

Figure 28. Creep test.

- In the case of an oscillation experiment …

$$\overline{J} = \frac{1}{G_0} + \frac{1}{j\omega\eta_o} + \sum_i \frac{A_i}{1 + j\omega\tau_i}$$

where the τ=0 and τ=∞ contributions, corresponding to a pure elastic and pure viscous behaviour, have been taken out of the sum. The Maxwell model [12, 13] corresponds to the case where only these two terms exist, the Burger's model [8] when the summation is restricted to one term, a more realistic representation of the experimental data in practice. In the general case, the behaviour is called viscoelastic.

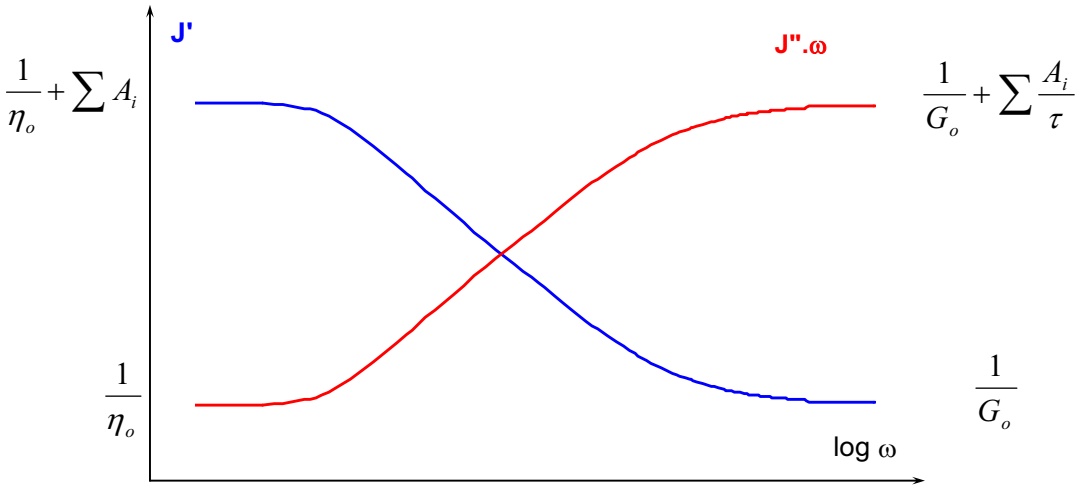

Figure 29. J' and (J".ω) as a function of log angular frequency.

It can be useful to plot the data in the complex plane [13]. A single term of the form : $\frac{1}{1+j\omega\tau}$ is represented by a semicircle of diameter unity and centred on the real axis, and the frequency at the top of the semicircle obeys the relation ωτ=1, see Figure 30.

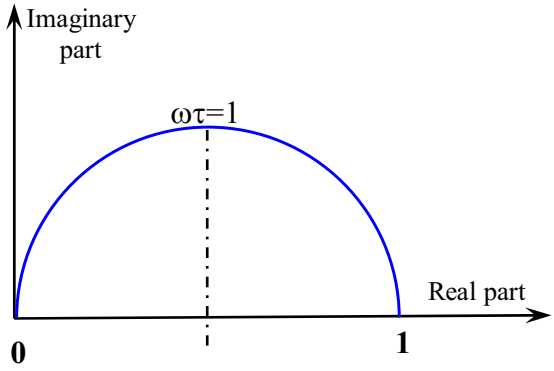

Figure 30. Cole-Cole plot.

One example is the Maxwell model, plotting G in the complex plane. In the case of the Burger's model [3, 8], J' and J"-1/($\eta_o\omega$) gives also a single term although the semicircle is translated by 1/G_o on the real axis.. In the general case of a distribution of relaxation times, plotting J' and J"-1/($\eta_o\omega$) in the complex plane, the figure is a superposition of semicircles, more or less a flattened semicircle if the time constants are close and numerous or distinct semicircles if they are far apart [14].

A distribution of time constants corresponds to a linear system of 1st order differential equations with constant coefficients, which is not always appropriate to describe the kinetics. Another case, often cited in the literature, is a power law [15, 16] :

$$G \approx (j\omega)^n$$

As a consequence, G' and G'' are parallel straight lines in a log-log representation and tan(δ)=G''/G' is a constant. In the complex plane, experimental data are aligned on the straight line with a slope tan(nπ/2). Indeed, one may question if G is the adequate response function because it is expected that at very high frequencies, the behaviour is elastic and viscous at very low frequencies. Probably,

$$J = \frac{1}{G_o} + \frac{1}{j\omega\eta_o} + A(j\omega)^{-n}$$

is a more adequate formulation. Several physical mechanisms could in principle lead to such a law (for instance a diffusion process with n=0,5) but in the field of rheology, it is usually associated with percolation and the existence of a fractal geometry [17]. However, only scaling arguments exist and no complete theory has been published. More over, some ambiguity may exist because measurements are performed in a restricted frequency interval: a broad distribution of time constants leads to the same observations.

- **Nonlinear behaviour and time evolution**

It has already been mentioned that the creep experiment is suitable to investigate the time evolution in the non-linear regime but this is not the only experiment.

In this work, Start-Up Flow (Stress Overshoot) was also performed. A shear strain rate is suddenly imposed on a viscoelastic fluid held previously at rest. The shear stress produced by this transient deformation displays an initial overshoot before reaching a steady-state value; hence, the phenomenon is commonly referred to as stress overshoot, see Figure 31.

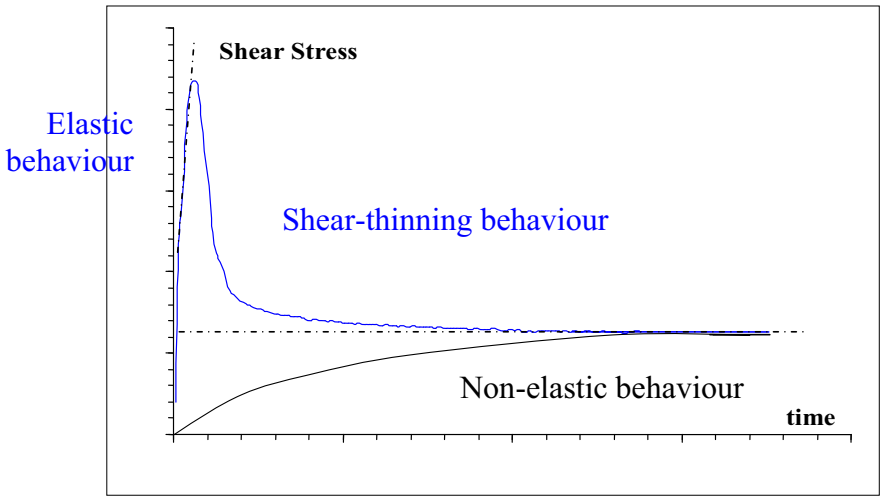

Figure 31. Stress response to a step increase in strain rate.

Results can be used to produce a shear stress growth function. The zero shear viscosity and the relaxation spectrum can be computed from the stress transient.

I.4 Calibrating the instrument before measurements.

I.4.1 The dynamics of the rheometer.

The fundamental equation of mechanics [18], when applied to the rheometer, becomes:

$$I\ddot{\theta} + f\dot{\theta} + \Gamma_1 = \Gamma$$

where Γ is the imposed torque, I the moment of inertia of the measuring system, f the friction coefficient. What is really applied to the sample is Γ_1, which can be quite different from Γ if friction and inertia contributions are important.

- Inertia contribution.

It is interesting to split up inertia moment into three contributions,

- that of the driving system, I_1 : its value is about 15.3 μN.m.s^2,

- that of the measurement geometry, I_2. Its value can be calculated by the following equation:

$$I_2 = \frac{\pi \cdot \alpha \cdot R^5 \cdot \rho}{10}$$

where: α is the cone angle (in degrees), R the radius, ρ the density of steel. The moment of inertia depends very strongly on the radius, being proportional to R^5. Using this equation for cone-plate geometry (R=20mm, α-1.6°), it is calculated as 7.9 μN.m.s^2.

- that of the sample which is difficult to estimate a priori. It is of the order of 0.5 μN.m.s² in the case of the blend.

- The friction term.

An air bearing is used to provide virtually friction free application of torque to the sample. f is equal to 0.5-1 μN.m/(rad/s).

The two parameters (I_1+I_2) and f can be determined from a simple creep experiment in the absence of sample but with the chosen geometry. The dynamic equation becomes :

$$I\ddot{\theta} + f\dot{\theta} = \Gamma$$

The velocity of the moving plate obeys a simple first order differential equation; the characteristic time and the stationary plateau are equal resp. to I/f and Γ/f, see Figure 32.

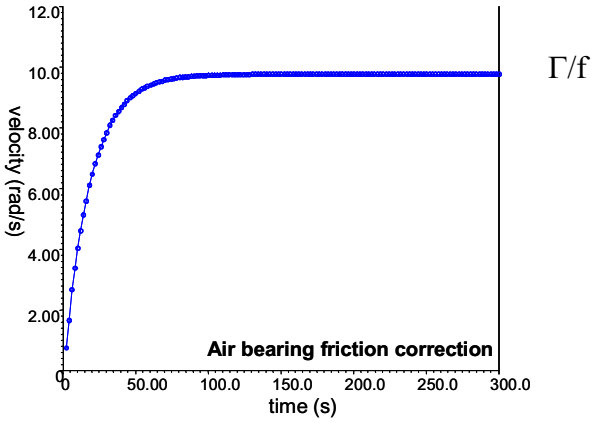

Figure 32. Response of the rheometer to a step increase of Γ (cone-plate geometry). Determination of I and f.

The time constants for the plate-plate and cone-plate system used in this work are respectively: 17.88 s and 22.67 s.

I.4.2 Tests.

- **Test 1**

To test the quality of the calibration, two standard oils of known viscosity were tested. As shown in Table 6, the agreement is good.

	Viscosity (Pa.s)	Exp. Viscosity (Pa.s)
Standard oil 1	η_1=0.83	η_1=0.82 +/- 0.02
Standard oil 2	η_2=1.092	η_2=1.093 +/- 0.02

Table 6. Study of two standard oils

- **Test 2**

The second test is an oscillation experiment performed on a standard oil in the linear regime. If the applied torque is a sine wave,

$$\Gamma = \Gamma_o \exp(j\omega t)$$

the response is also alternating with the same pulsation :

$$\theta = \theta_0 \exp(j\omega t + j\varphi)$$

The dynamic equation becomes :

$$(-\omega^2 I + j\omega f)\theta_o e^{j\varphi} + \Gamma_1 = \Gamma \text{ or } \frac{\Gamma_1}{\Gamma} = 1 + (\omega^2 I - j\omega f)\frac{\theta_o}{\Gamma_o} e^{j\varphi} = Ae^{j\psi}$$

The results are presented in Table 7,

Frequency (rad/sec)	**Phase φ(°) (raw data)**	**A**	**Ψ(°)**	**Phase (corrected)**
0.62	91.81	1.001	1.825	89.98
0.99	92.82	1.000	2.836	89.98
1.57	94.34	0.998	4.388	89.95
2.50	96.72	0.994	6.861	89.86
6.28	106.2	0.961	16.634	89.57
15.78	125	0.820	36.328	88.67
39.65	150.2	0.498	63.630	86.57
99.58	167.7	0.215	85.727	81.97
250.13	175.1	0.088	99.279	75.82
628.31	178.6	0.031	126.616	51.98

Table 7. Evaluation of the contributions of inertia and friction.

and depicted in Figure 33.

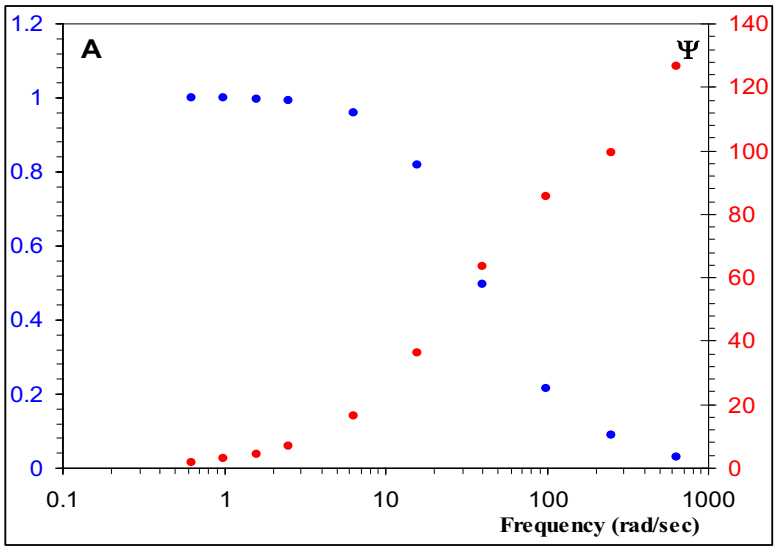

Figure 33. Factor A (Blue) and Ψ (Red) depicted as a function of frequency.

It could be concluded that corrections to the ideal case (A=1, Ψ=0) are negligible below 1 rad/s. In fact, this is not true because the corrections are then similar to the deviation from a pure viscous behaviour. In particular, this makes the determination of G' very uncertain, very sensitive to the contribution of the sample inertia (I_3). Increasing the frequency, A decreases rapidly, which means that an experiment performed at constant torque Γ is not performed at constant torque Γ_1. At the highest frequency Γ is divided by as much as 30 !

For two weeks, each day, an oscillation test was made. The system inertia $\mathbf{I_s}$ varied in range of 23.01-23.27 µNms^2 while the variations of the factor f were negligible. The influence of such variations on G' and G" are depicted in Figure 34.

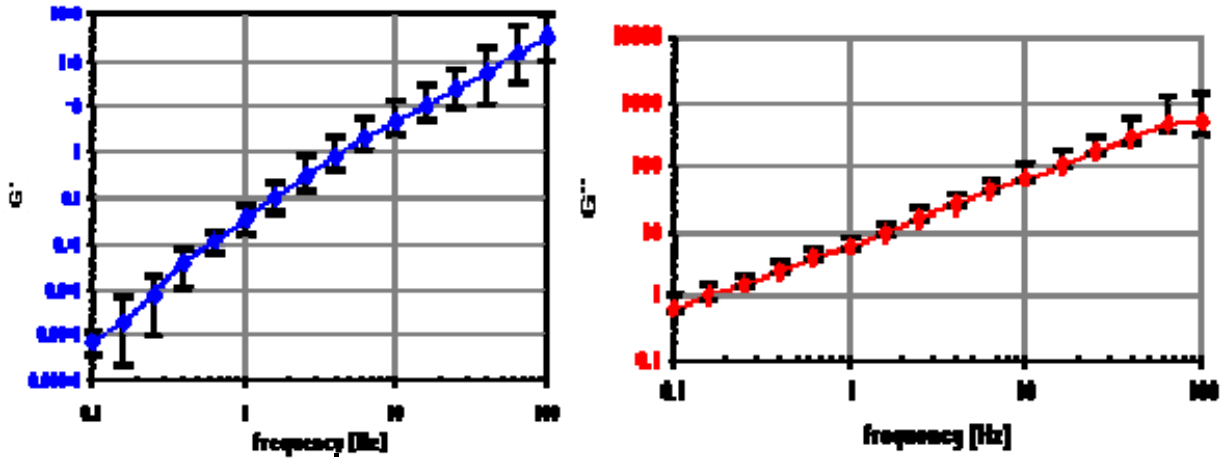

Figure 34. Statistical error on G' and G". Study of the standard oil.

I.5 Artefacts.

- **The fracturing phenomena**.

This artefact, see Figure 35, is observed in all experiments involving highly loaded pastes (50-60% vol. of the powder) performed with the plate-plate geometry.

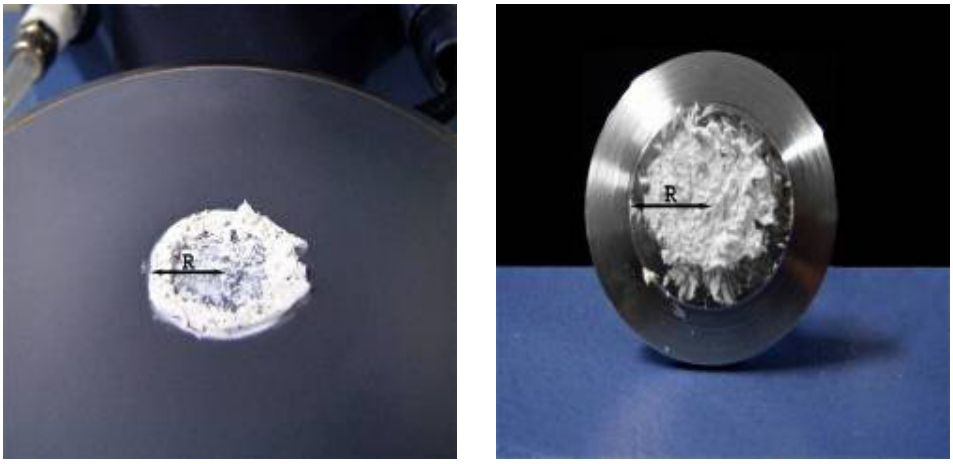

Figure 35. Fracturing phenomena.

Then, the cone-plate system was chosen.

- **Sedimentation and segregation of particles**.

In some conditions, segregation and/or sedimentation have been observed, see Figure 36. This occurs in the case of low solid fraction pastes (<10%vol.) when the applied stress is high or for long resting time (min.3 hours). It does not depend on the used geometry.

Figure 36. Sedimentation of particles. ***Figure 37. Throw away of paste***

- **Throw away of the paste.**

When the applied torque or deformation is too high, this phenomenon is observed, see Figure 37. The critical stress depends on the solid fraction of the paste and increases regularly from 200 Pa below 10%vol. up to 1500 Pa for 60%vol. solid fraction**.** It depends also on the measuring time.

- **An optical encoder rollover issue-**

For samples with a very low viscosity the displacements in the point time are very large and the encoder can only count up to ~1300 rad before a reset occurs. To work around this problem a shorter sample period and maximum point time – 15 sec and 2 min was chosen.

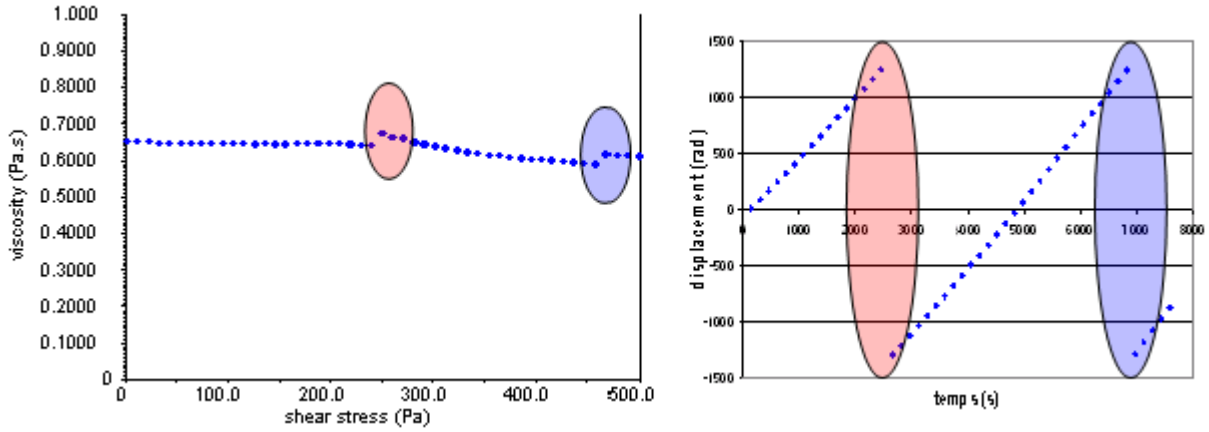

Figure 38 The variations of viscosity are not real ! b) Zooms

- **Errors in torque value.**

Error associated with truncated cones, may be considered as a deviation from the ideal geometry. The maximum relative error introduced by the truncated cone can be easily described by the following equation:

$$\%E_{\max} = \left[1 - \frac{R^3 - R_T^3}{R^3}\right] \cdot 100$$

$\%E_{max}$=0.125%

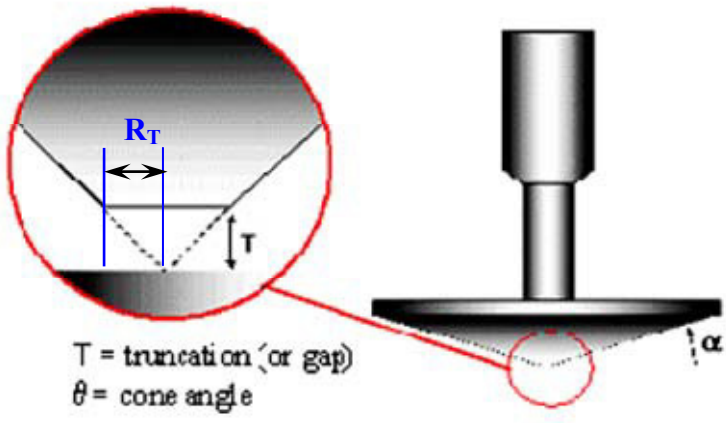

Figure 39. Error induced by the truncation of the cone on the torque value.

II Rheological characterization of the organic matrix.

The organic medium is a mixture of four components : Paraffin wax, Ethyl Vinyl Acetate (EVA), Carnauba wax, and Stearic acid. The composition used in low pressure injection moulding is the following :

	Paraffin wax	**EVA**	**Carnauba wax**	**Stearic acid**
EPAC (% vol.)	70.00	20.00	9.75	0.25

Table 8. Composition of the organic medium.

Their rheological behaviour will be now investigated.

II.1 Paraffin.

At 130°C, paraffin is a simple fluid with a low viscosity, 2.5 mPa.s., as proved by the different experiments : flow test, creep and oscillation.

II.2 EVA.

Addition of EVA to paraffin has a strong impact on the properties of the mixture. Three compositions were studied: EP1 (80P-20EVA), EP2 (65P-35EVA) EP3 (55P-45EVA).

- Flow tests show a Newtonian behaviour, except a slight shear thinning effect of EP3 at high stresses (above 100 Pa). The viscosity increases exponentially with the EVA content, see Figure 40 .

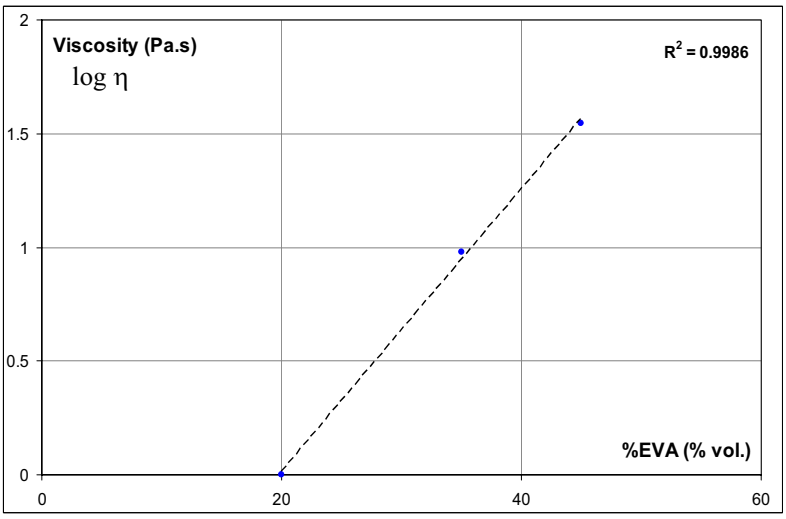

Figure 40. Variation of the viscosity as a function of EVA percentage.

The mixture paraffin + EVA is viscoelastic at short times. A preliminary test shows a linear response in a wide range of stresses, see Figure 41.

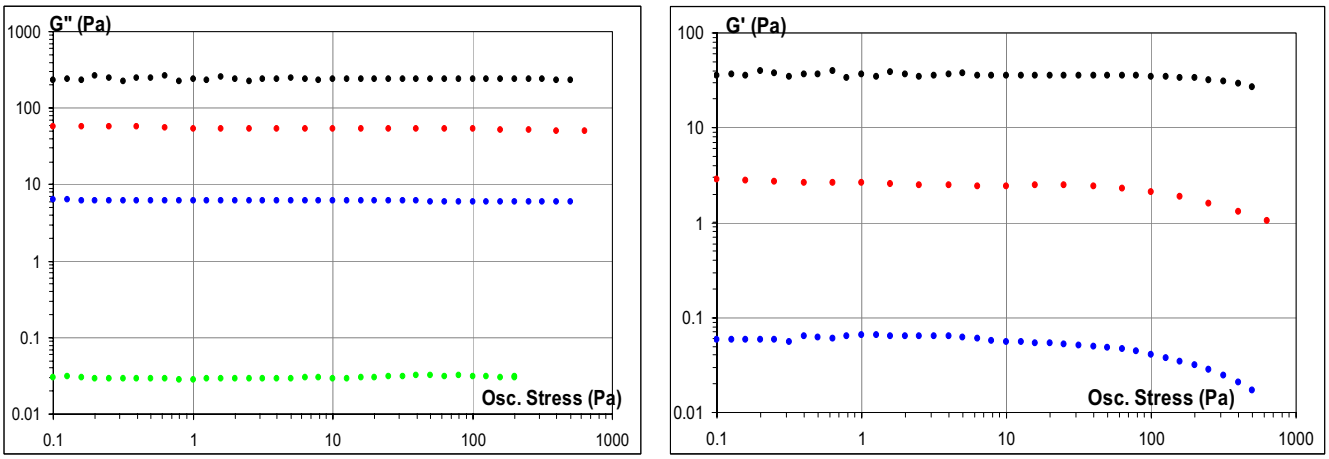

Figure 41. Oscillation curve – stress sweep test.
Paraffin (Green), Paraffin + 20% (Blue), 35% (Red), 45% (Black) vol. of EVA.

The variations of the moduli G' and G" with frequency are depicted in Figure 42.

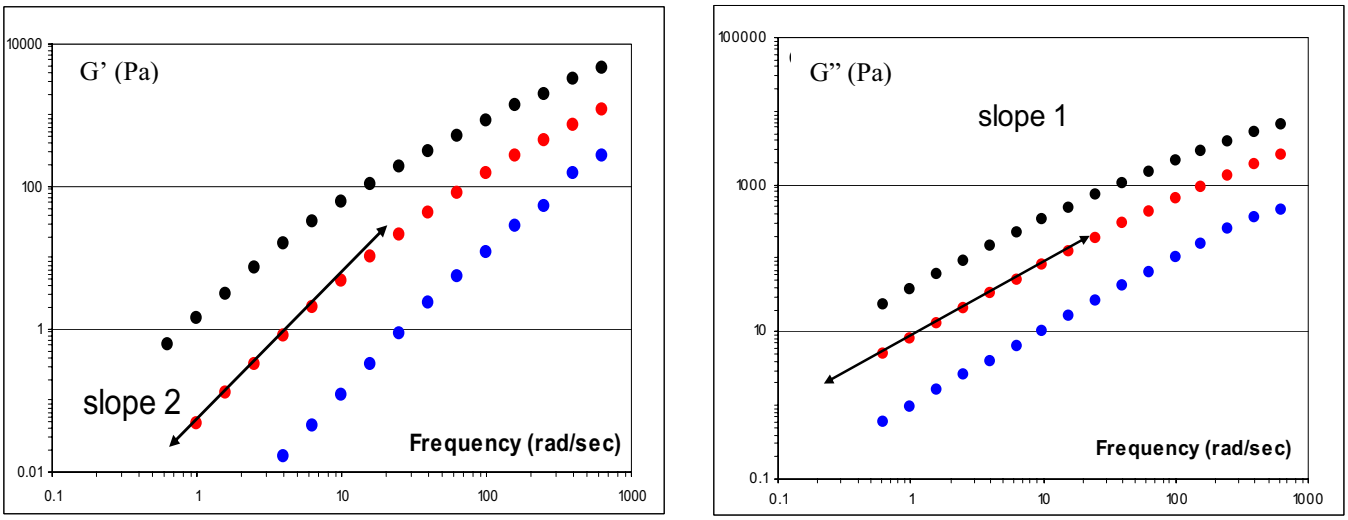

Figure 42. Frequency dependence of storage modulus in a log-log scale.
Paraffin + 20% (Blue), 35% (Red), 45% (Black) vol. of EVA.

In all cases, G" is much greater than G', i.e. the behaviour is essentially viscous. Equivalently, the variations of J' and J"ω are depicted on Figure 43.

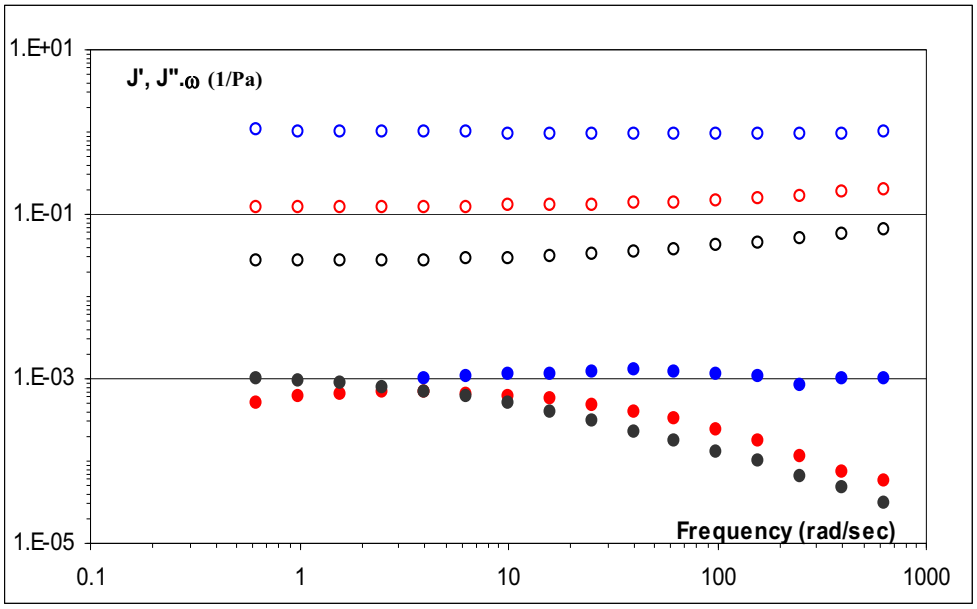

Figure 43. J'(full dots) and (J".ω) (open dots) as a function of frequency. Paraffin + 20% (Blue), 35% (Red), 45% (Black) vol. of EVA.

They make clear the fact that the main contributions to the modulus G are only a pure elastic and a pure viscous terms. In the case of samples EP2 and EP3, additional terms exist which account for deviations of J' and (J"ω) from a constant value, resp $1/G_o$ and $1/\eta_o$. Representation in the complex plane, see Figure 44, reveals a distribution of relaxation times, the same for the two compositions.

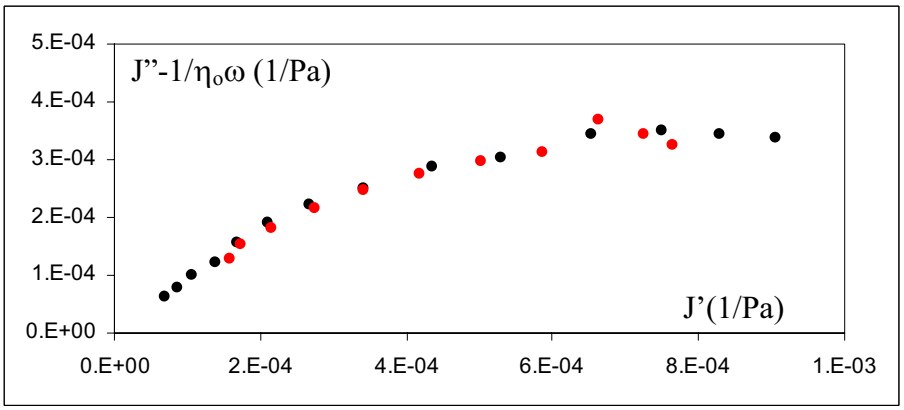

Figure 44. Cole-Cole plot.
Paraffin + 35% (Red), 45% (Black) vol. of EVA..

This dispersion is usually attributed to entanglements of the polymer chains.

- **Temperature effect**.

  In this experiment, the temperature was varied between 90°C and 140°C.

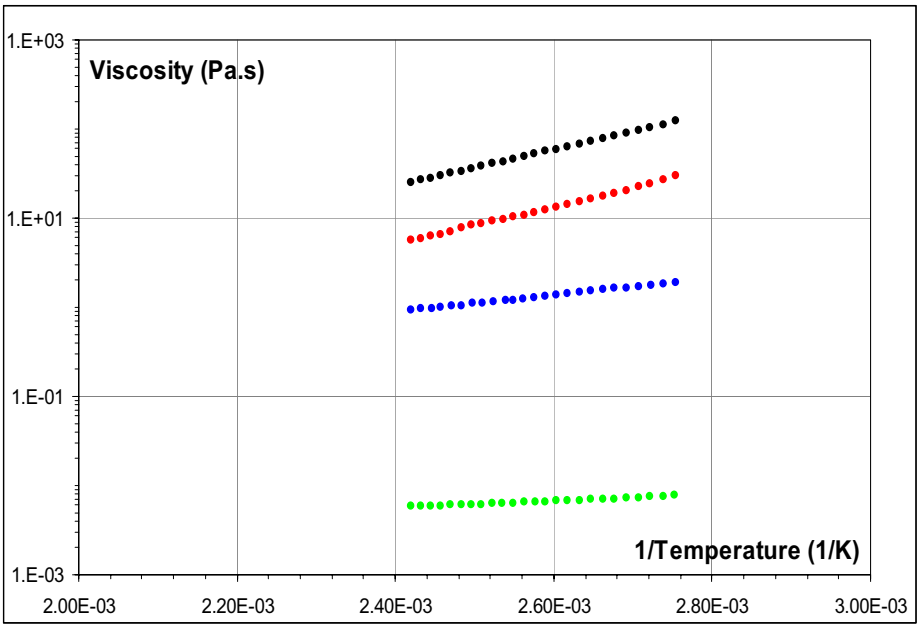

Figure 45. Variations of the viscosity of the blend with temperature in an Arrhenius plot. Paraffin (Green), Paraffin + 20% (Blue), 35% (Red), 45% (Black) vol. of EVA.

As expected, the viscosity decreases with temperature and the variations are well represented by an Arrhenius law [3]:

$$\eta = A \exp\left(\frac{E_a}{R\,T}\right)$$

where R is the universal gas constant, E_a and A are adjustable parameters, see Table 9.

Material	A	E_a(kJ/mol)	% viscosity/°C
Paraffin	3.1	30.4	-0.55
EVA 20%	3.66	61.7	-1.1
EVA 35%	4.1	166.1	-3.0
EVA 44%	4.5	169.4	-3.5

Table 9. Viscosity changes and activation energies for pure paraffin and the various blends with EVA.

III Study of the paste.

III.1 Flow tests, experimental results.

Flow tests have been conducted as already described. The procedure consists of a succession of short creep experiments. For low solid fractions, the creep duration was varied between 30 and 200s; for higher solid fractions (10-20-30-40-50-60%vol.), it was fixed as 200 s. In this chapter only results for pastes loaded with Y-doped zirconia are presented. Influence of the powder material will be studied in chapter IV.

III.1.1 0, 2, 5%vol. solid fraction.

The observed behaviour is a pure viscous one, except for a paste load of 5% vol. of powder and a very small applied stress (1Pa), where viscoelasticity could be noticed at short times, see Figure 46 a).

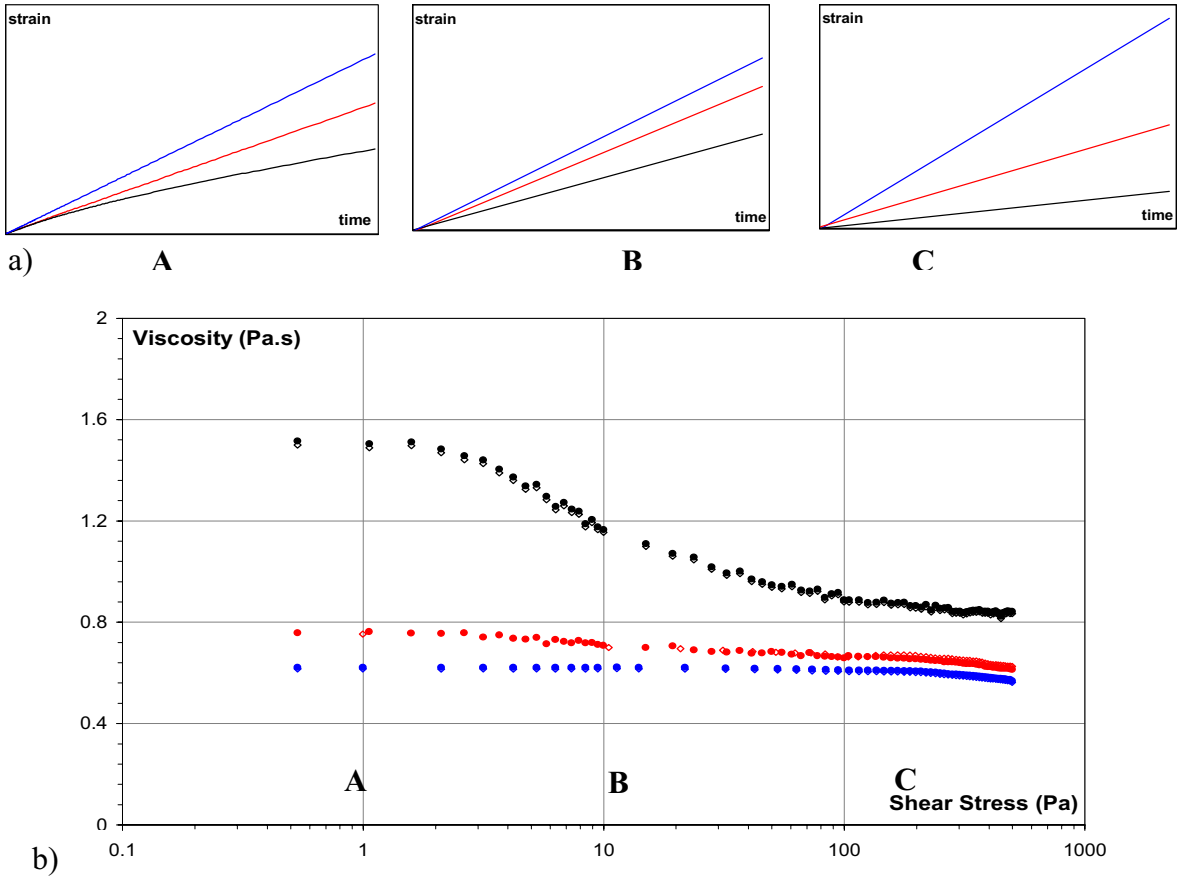

Figure 46. a) Creep curve 0% (Blue), 2% (Red), 5% (Black) A. 1Pa, B. 10Pa, C. 200Pa. Strain axis – arbitrary scale.
b) Flow curve – semi-log scale. Viscosity vs shear stress for 0% (Blue), 2% (Red), 5% (Black) % vol. of the powder. Open dots – return procedure.
Points A, B, C denote stresses for which the creep curve is depicted in Figure 46 a).

These flow tests were performed for different creep durations (between 30 and 200 s.), up and down, with identical results. In Figure 46b, the viscosity is plotted versus the shear stress.

In the absence of powder, the behaviour is Newtonian, except at the highest shear stresses but this is probably an artefact because it is observed that centrifugal forces become important and tend to throw the mixture out of the cell. The introduction of powder particles (2% and 5% vol. of the powder) leads to an increase of viscosity and a non Newtonian shear thinning behaviour, which can be well fitted with Carreau's law [4].

III.1.2 10%vol. solid fraction.

One example of a flow curve is given in Figure 47.

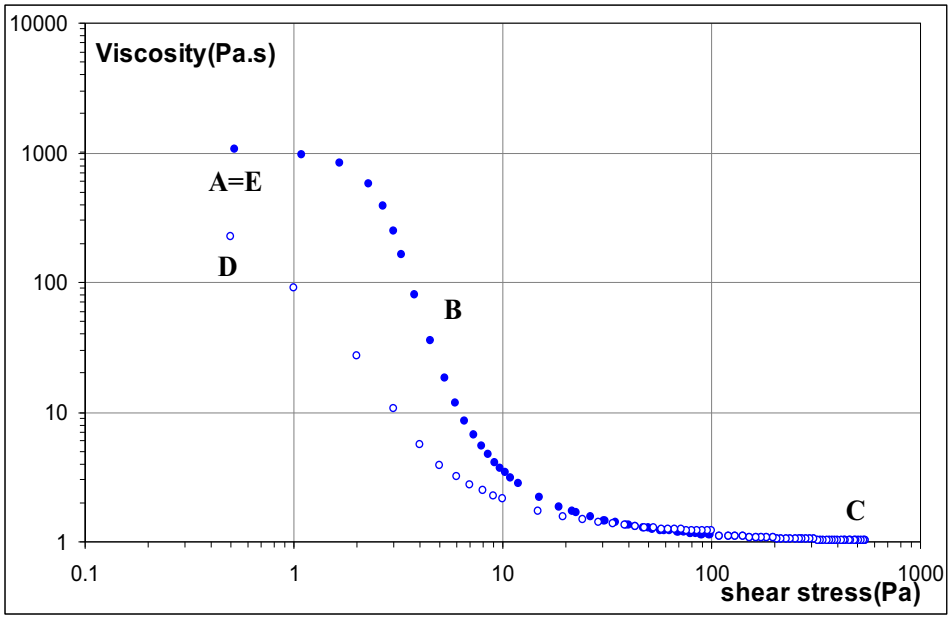

Figure 47. Flow curve – log-log scale. Full dots (curve ABC) - increasing stresses, open dots - (curve CD) decreasing stresses. Second and next stress cycle: curve EBCD. Points A,B,C,D,E denote stresses for which the creep curve is depicted in Figure 48.

The curve is very similar to that obtained in the case of a 5%vol. loaded paste, but at low stresses, viscoelasticity is more important, (see sketch A in Figure 48, and a time duration of 200 sec was chosen, to measure properly the viscosity and to eliminate the viscoelasticity effect. With increasing stresses, a strong non-Newtonian behaviour (shear thinning) is observed. The microstructural changes of the material are not instantaneous as depicted in sketch B and probably the equilibrium state is not realized. At high shear stresses, the behaviour is purely viscous (sketch C) and even quasi Newtonian – plateau η_∞. Then, the suspension is probably made of non-interacting aggregates. Decreasing the stress, some

hysteresis can be seen. In conditions of D, a thixotropic effect (the inverse of B) is observed. Waiting long enough – in this case a minimum of 30 minutes – the same value of the initial viscosity η_o is recovered, but the viscoelastic effect (sketch E) is no longer observed. Repeating the stress cycle, the same curve (EBCD) is obtained.

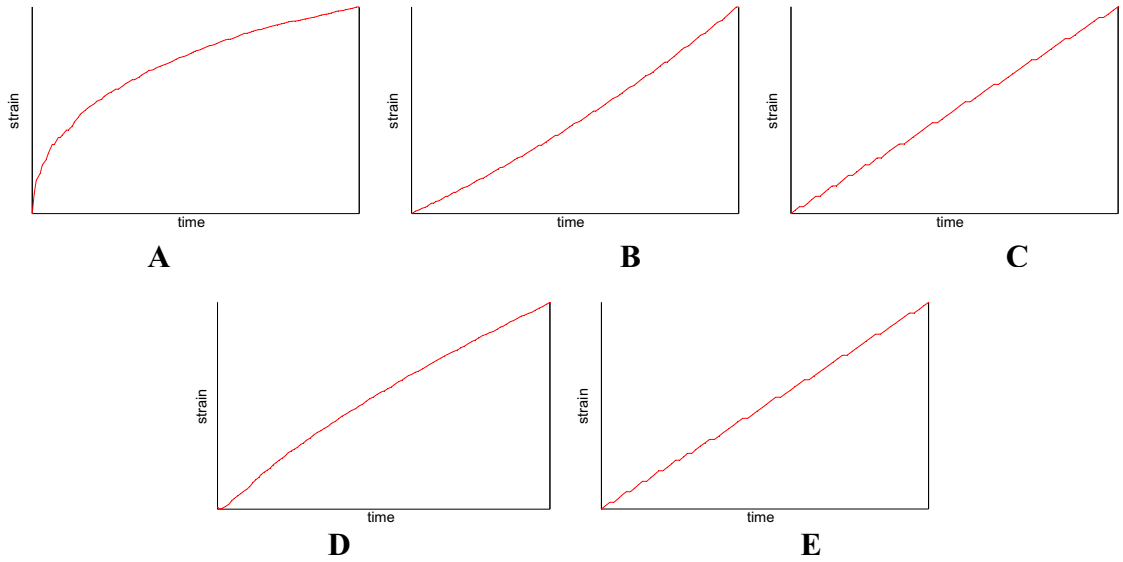

Figure 48. Paste filled with 10% vol. solid fraction.
Creep curves: A=E. 0.5Pa, B. 50Pa, C.500Pa, D.0.5Pa. Strain axis – arbitrary scale.

III.1.3 20% vol. solid fraction.

The flow curve is depicted in Figure 49

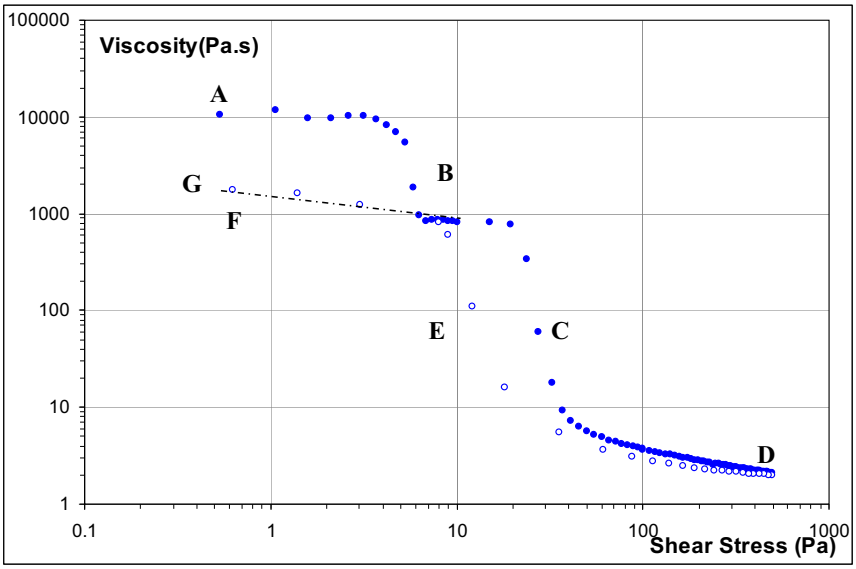

Figure 49. Flow curve – log-log scale. Full dots (curve ABCD) - increasing stresses, open points - (curve DEF) decreasing stresses. Second and next stress cycle (curve GCDEF). A, B, C, D, E, F, G denote stresses for which the creep curve is depicted in Figure 50.

Most features already noticeable in the case of 10%vol. solid fraction can be seen, but in addition an intermediate plateau of viscosity appears about 1000 Pa.s. a value close to that of 10%vol. solid fraction paste : a strong viscoelasticity at low applied stresses (sketch A in Figure 50), thixotropy at intermediate values (sketches B, C, E), a "pure" viscous behaviour (sketch D) at high stresses. Decreasing the stress, some hysteresis can be seen (sketch E). At the lowest stresses, the data become very noisy, (sketch F), what is probably due to, a spatial redistribution of the powder between the cone geometry and the Peltier plate. Waiting a very long time, even a couple of hours, the initial viscosity η_o cannot be recovered. Further stress cycling gives the same curve (GCDEF). Comparison of sketches A and G, shows less viscoelasticity after an initial run.

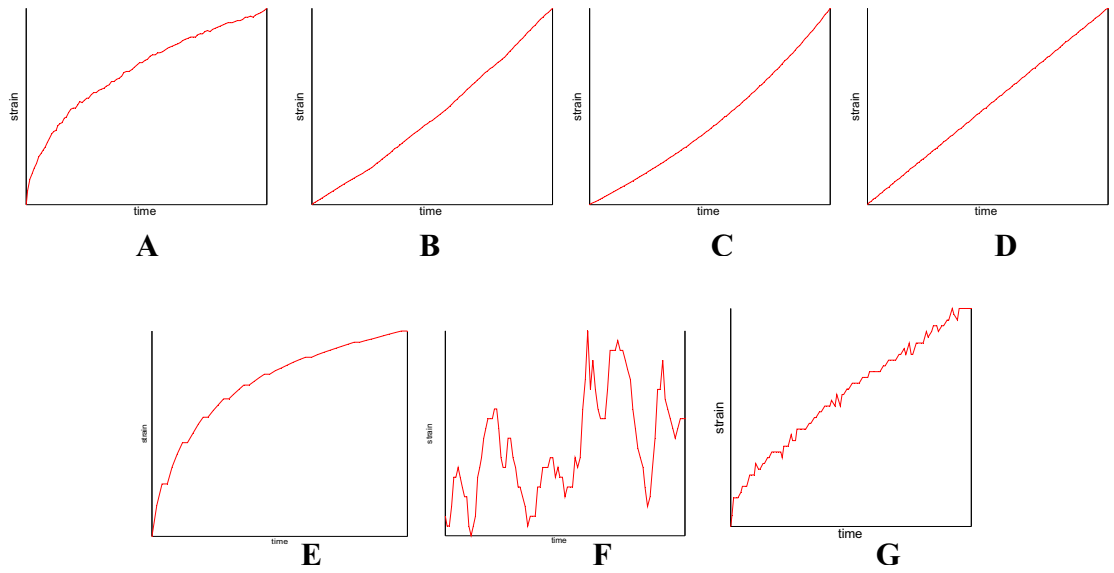

Figure 50. Paste filled with 20% vol. solid fraction. Creep curves: A=F=G. 0.5Pa, B. 50Pa, C. 300Pa, D. 500Pa, E. 15Pa. Strain axis – arbitrary scale.

III.1.4 30%vol. solid fraction.

The flow curve is depicted in Figure 51.

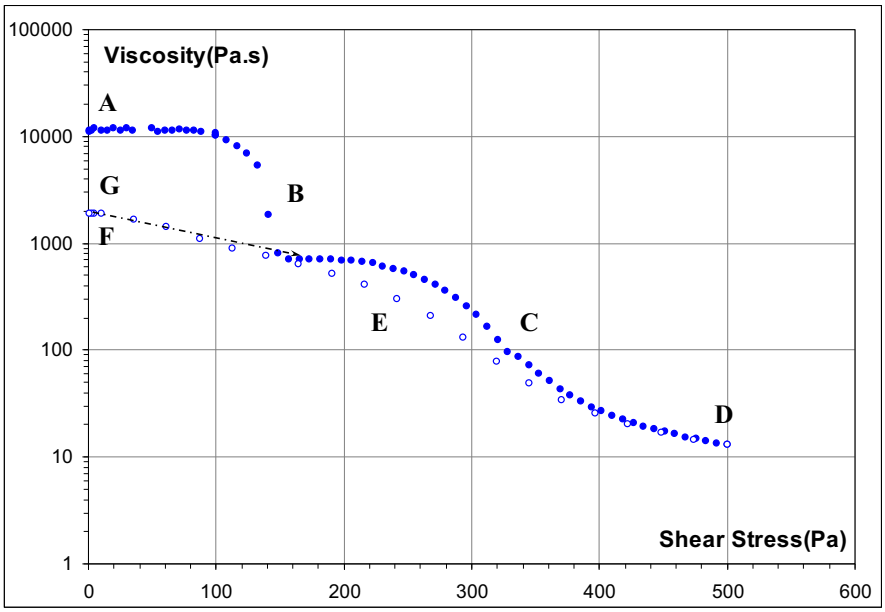

Figure 51. Flow curve – semi-log scale. Full dots (curve ABCD) - increasing stresses, open dots - (curve DEF) decreasing stresses. Second and next stress cycle (curve GCDEF). A, B, C, D, E, F, G denote stresses for which the creep curve is depicted in Figure 52.

It can be seen that it is very similar to Figure 49. This impression is reinforced by a comparison of the sketches in Figures 50 and 52.

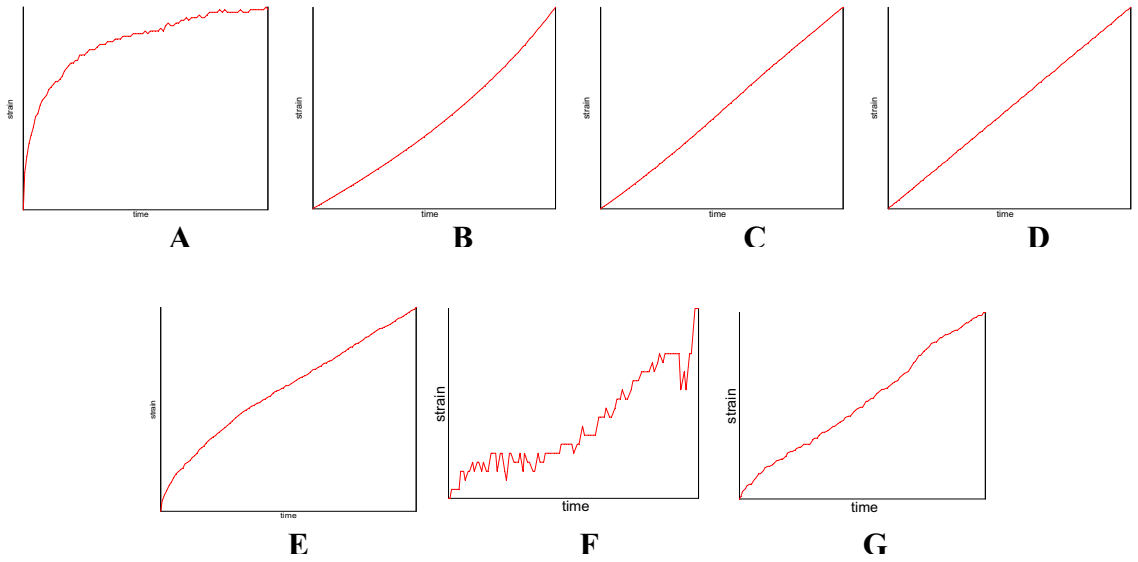

Figure 52. Paste filled with 30% vol. solid fraction. Creep curves: A=F=G. 0.5Pa, B. 50Pa, C. 350Pa, D. 500Pa, E. 300Pa. Strain axis – arbitrary scale.

III.1.5 40%vol. solid fraction.

The flow curve is depicted in Figure 53, exemplified by sketches of Figure 54.

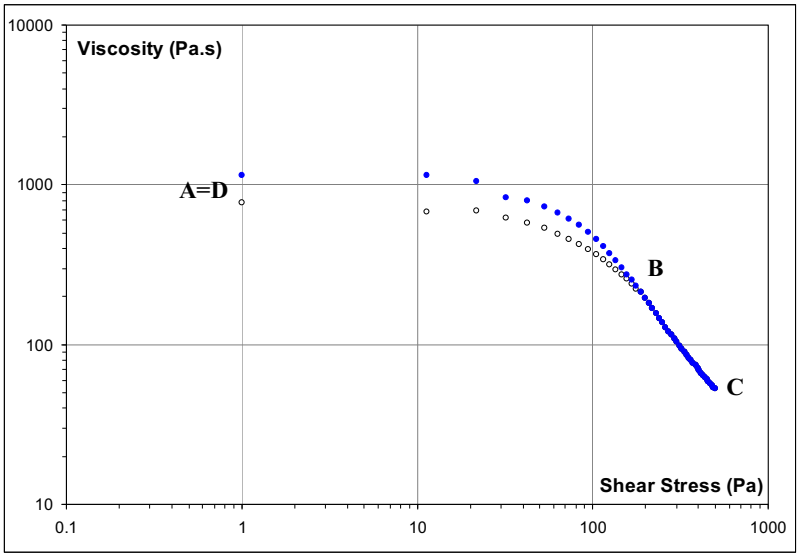

Figure 53. Flow curve – log-log scale. Full dots (curve ABC) - increasing stresses, open dots - (curve CD) decreasing stresses. Second and next stress cycle (curve ABCD). A, B, C, D denotes stresses for which the creep curve is depicted in Figure 54.

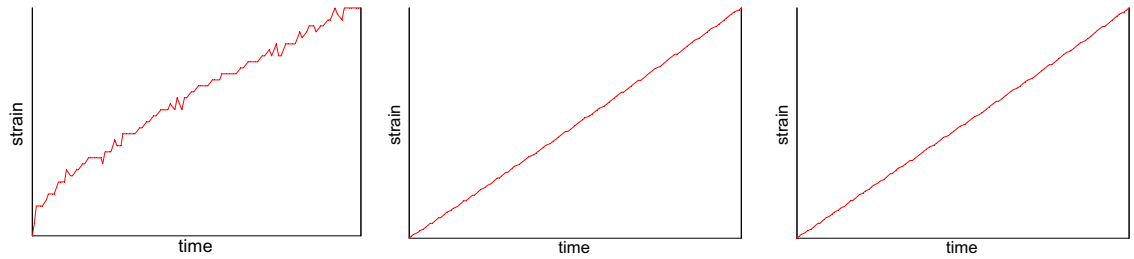

A=D **B** **C**

Figure 54. Paste filled with 40% vol. solid fraction. Creep curves: A=E=D. 1Pa, B. 200Pa, C. 500Pa. Strain axis – arbitrary scale.

Surprisingly, this flow curve is simpler than those described in the two previous paragraphs although the solid fraction is higher: no intermediate plateau of viscosity, small hysteresis, less viscoelasticity. Curve (ABCD) is reproducible with further cycling.

III.1.6 50, 60%vol. solid fraction.

In Figure 55, the variations of the shear rate are depicted versus the applied stress during the first cycle for a solid fraction of 60%vol.

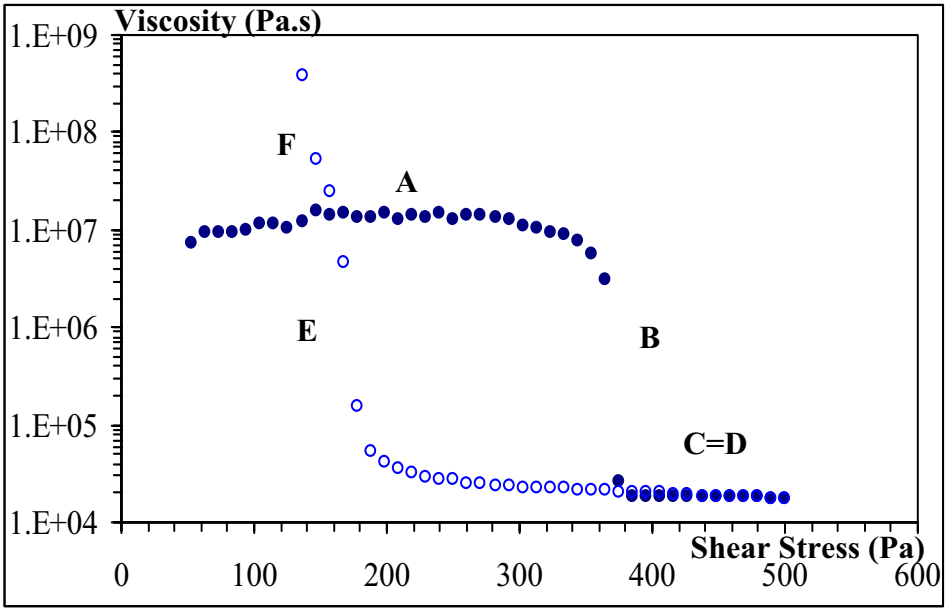

Figure 55. Flow curve – semi-log scale. Full dots (curve ABC) - increasing stresses, open points - (curve DEF) decreasing stresses. Points A, B, C, D, E, F denote stresses for which the creep curve is depicted in Figure 56.

Increasing the applied stress, a plateau of very high viscosity is observed at low stresses followed by a rapid decrease at a critical stress σ_1 and another plateau of much lower viscosity. On return, the transition occurs at a much lower value of the stress, σ_2. Below σ_2., the behaviour is no longer viscous. The examination of the time sketches is instructive:

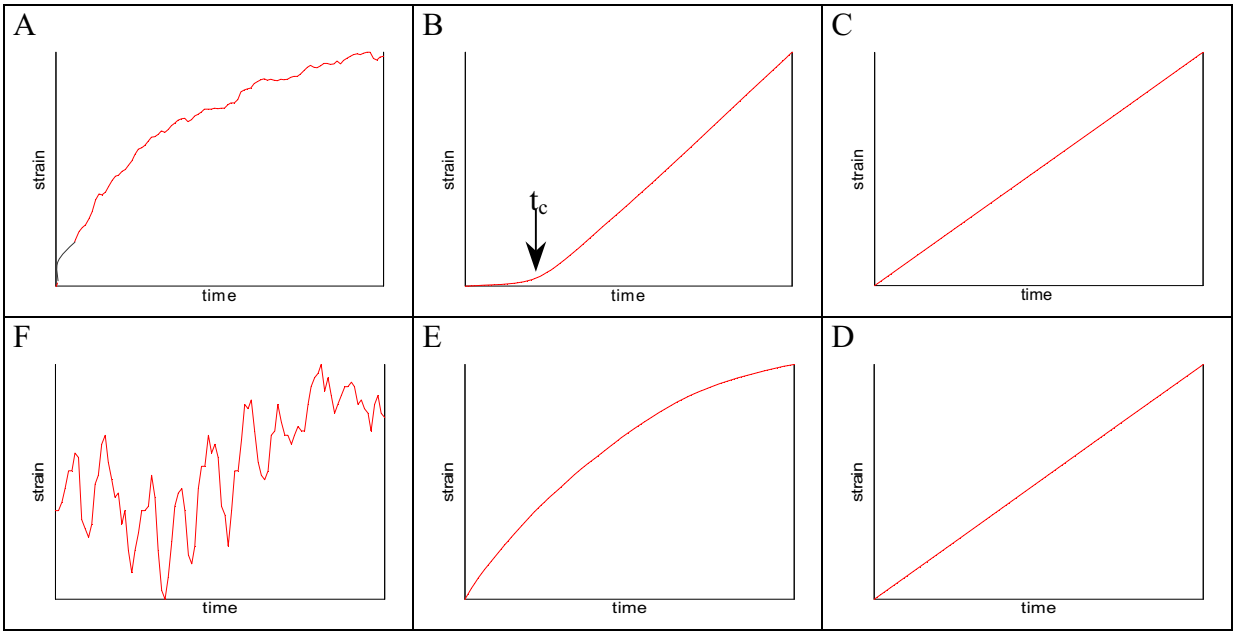

Figure 56. Paste filled with 40% vol. solid fraction. Creep curves: A. 200Pa, B. 380Pa, C=D. 450Pa, E. 175Pa, F. 130Pa. Strain axis – arbitrary scale.

In A, the behaviour is viscoelastic. In C (and D), it is purely viscous. The transition between the two regimes occurs suddenly as shown in B. Indeed, it lasts a few seconds. On return, the transition is also rapid but takes a longer time, a few tens of seconds. In F, the sample no longer flows. [19, 20]

In linear coordinates, the same data can be analysed as a Bingham law [3], see Figure 57. The dynamic is equal to 12 000 Pa.s about.

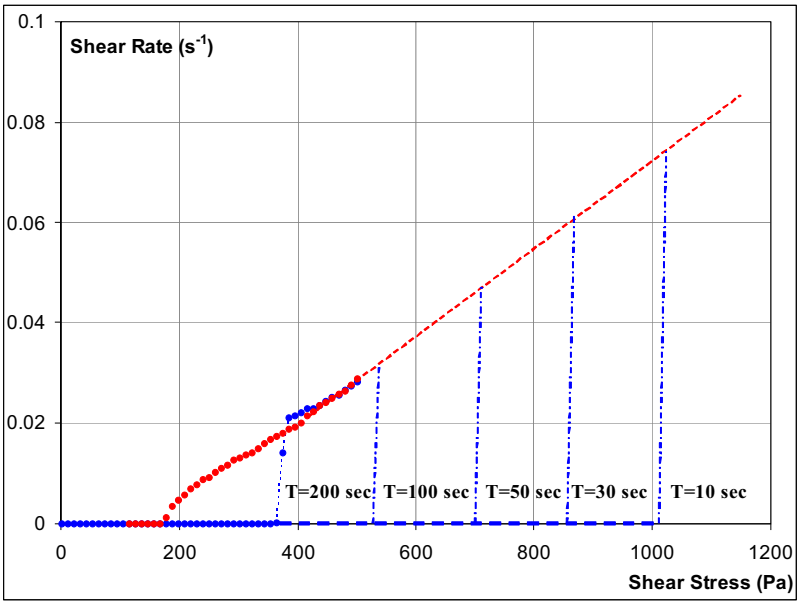

Figure 57. Flow curves in a linear system of coordinates, obtained for different step durations.

If one varies the duration of the each step, the two critical stresses, σ_1 and σ_2, behave differently. The former increases with decrease of the duration while the latter is unchanged. Indeed the return curve appears to be an "equilibrium curve".

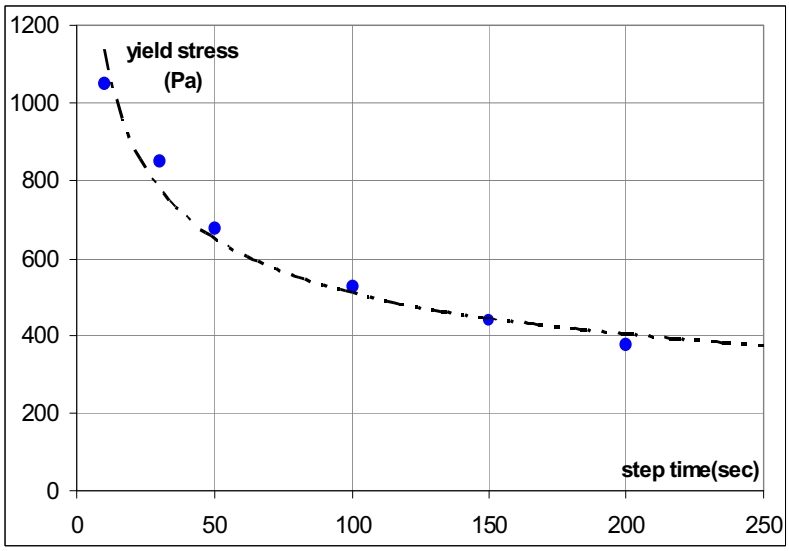

Figure 58. Variation of the yield stress with the step duration.

Plot of the critical stress versus the step duration, see Figure 58, shows that a very long time is needed in order that σ_1 equals σ_2.

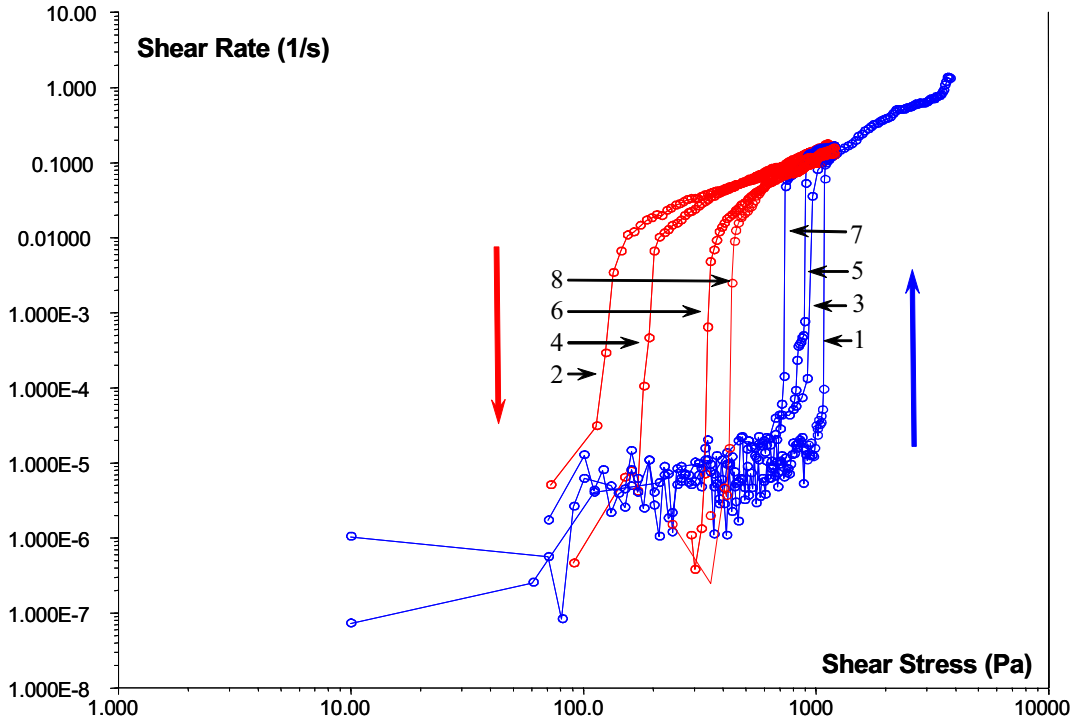

Figure 59. Flow curve in log-log scale. Successive cycling.

Figure 59 presents what happens on further cycling. Qualitatively all curves are similar but both σ_1 and σ_2 change while the step duration is fixed: they become closer to each stress cycling to other. Each stress cycle modify the microstructure of the paste.

All these features are common to the 50 and 60vol% solid fraction pastes.

III.2 Interpretation

III.2.1 The high shear stress behaviour

One main feature of the results which have been presented, is the reliability of the data at high shear stresses (for instance at a shear stress of 200 Pa). In Figure 60, the relative viscosity, η_r, is plotted versus solid fraction for low solid fractions (0, 2, 5 %vol.).

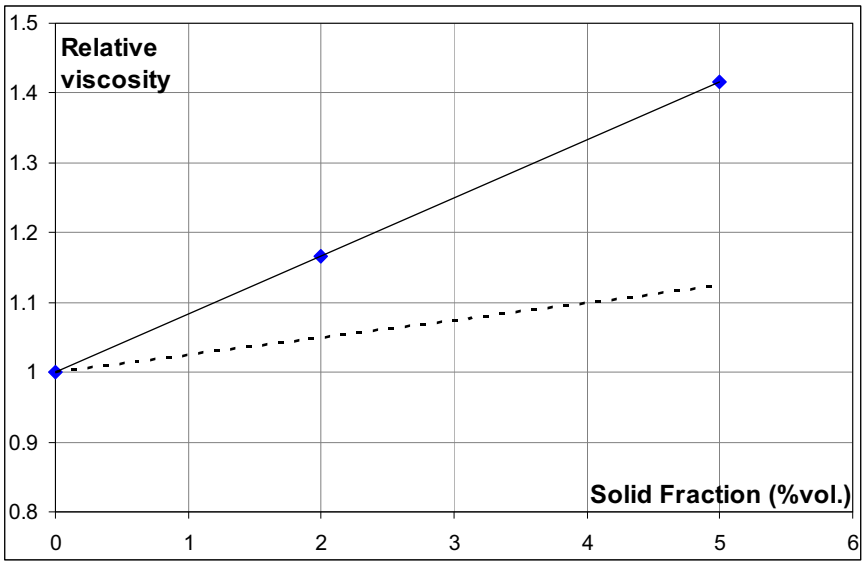

Figure 60. Relative viscosity vs. the volume fraction of powder. Experimental data - Blue dots, – linear fit, - - - Einstein model

A straight line can be drawn through the experimental data points in agreement with the Einstein's law [21] but with a different slope, 7.5 instead of 2.5. A factor **k** can be introduced,

$$\eta_p = \eta_m \cdot (1 + k \cdot 2.5 \cdot \varphi)$$

equal to 3. This observation is quite common and often this factor k is attributed to the non-spherical shape of powder grains [22], contrary to one of the hypothesis made by Einstein in his model.

Similar studies have been performed, mixing the powder with paraffin, carnauba wax, paraffin and carnauba wax, paraffin and EVA. The results are presented in Figure 61.

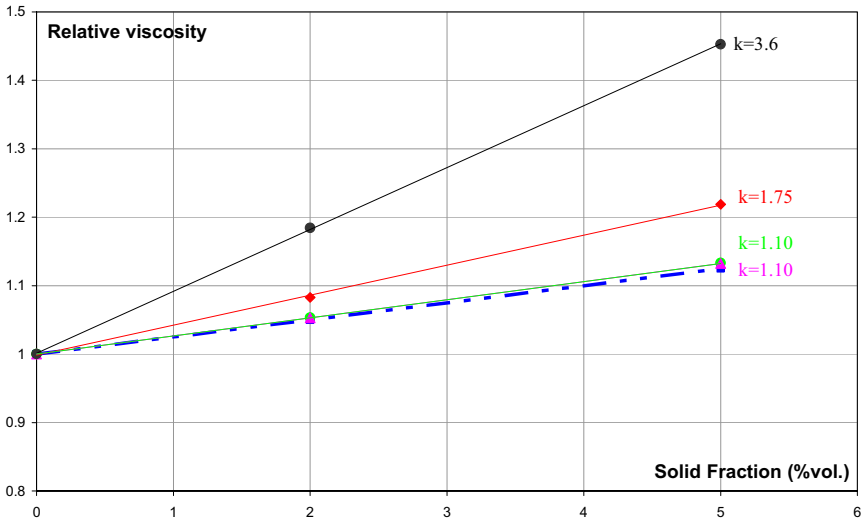

Figure 61. Relative viscosity versus solid fraction : experimental data: Powder + paraffin (P) (Rose), powder + carnauba wax (C) (Red), powder +P+C (Green), powder +P+EVA (Black), - linear fit of the curves, - - - Einstein model.

In all cases, a linear relationship is observed but the value of **k** depends on the organic composition. In the case of carnauba wax, or carnauba wax and paraffin, this factor is equal to 1.1. Sedimentation test of the powder immersed in liquid carnauba wax at 130°C proves that the wax is a good dispersant. This was further confirmed by SEM observations, see Figure 62.

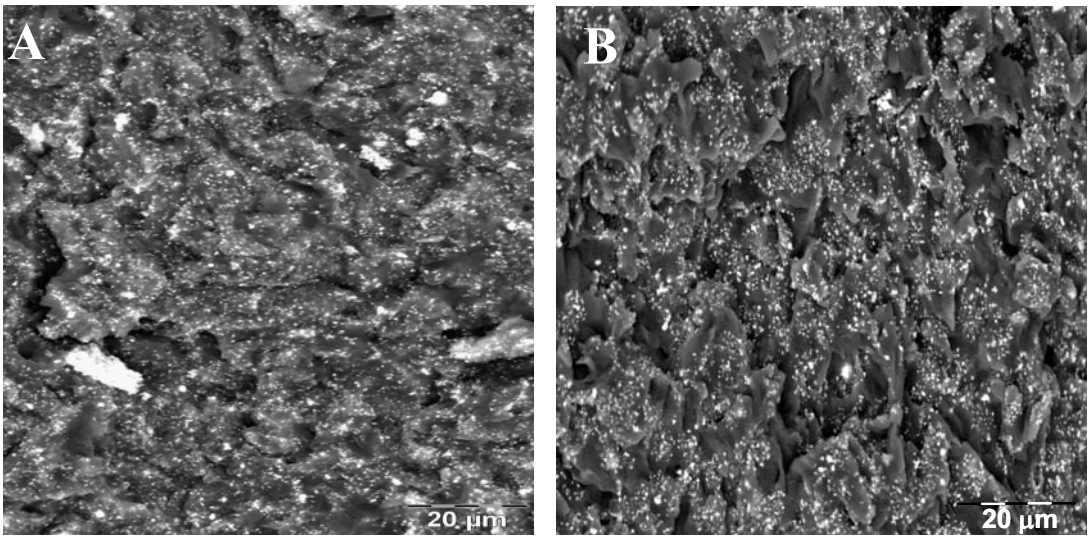

Figure 62. SEM observation (5% vol. solid fraction). A. carnauba wax + powder, B. paraffin + carnauba wax + powder.

This proves that the shape of the grains is indeed not very different from spherical. In the case of paraffin, in which the powder flocculates, see Figure 63, k=1.75.

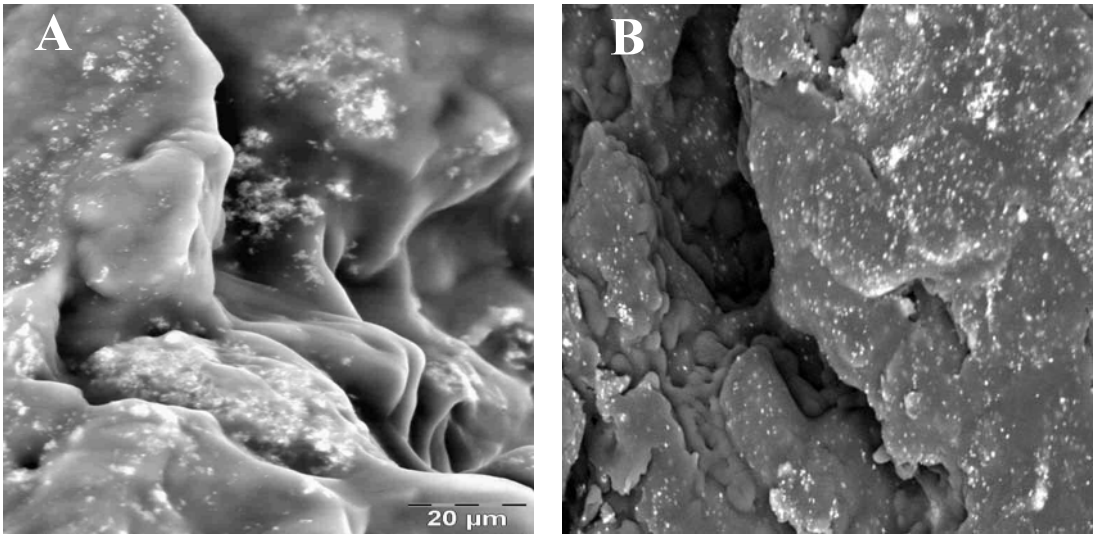

Figure 63. SEM observation (5% vol. solid fraction): A. paraffin + powder; B. paraffin + EVA + powder.

It is concluded that the volume fraction of solid to be inserted in Einstein equation, $\phi*$, must take into account the liquid trapped into the aggregates[*], i.e.; $\phi* = k\,\phi$. In the case of the blend

[*] aggregate – a collection of strongly bounded grains.

paraffin+ EVA, k=3.6, a value not very different from 3.0. This identifies EVA as responsible for the high value of k and confirms, if necessary, its binding character. Having justified experimentally the interpretation of k, its determination permits to evaluate the trapped liquid fraction (k-1)ϕ.

Solid fraction (% vol.)	**Trapped liquid (% vol.)**	**Carnauba wax (% vol.)**	**EVA (% vol.)**	**Paraffin wax (% vol.)**
2	4	9.8	20	68.2
5	10	9.5	19	66.5

Table 10. Comparison of the trapped liquid content in the agglomerates* with the volume fraction of each component.

In Table 10, the quantity of trapped liquid is compared to the amounts of the different components. Let us remind that they are immiscible which arise the question of the nature of the trapped liquid. We know that carnauba wax and EVA have strong affinities to oxides contrary to paraffin [23]. These data suggest that EVA + carnauba wax is indeed in sufficient amounts to provide the trapped liquid.

If the relative viscosity is plotted versus the volume fraction of solid, see Figure 64, for larger solid fractions (10, 20, 30, 40%vol.), a departure from the linear fit is observed, as expected.

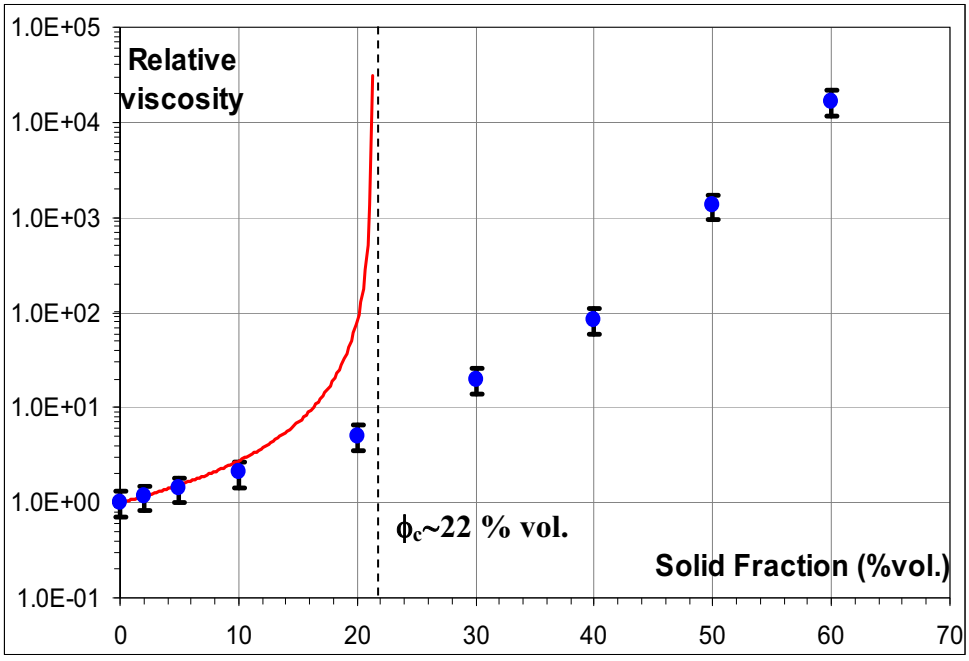

Figure 64. Relative viscosity vs the volume fraction of solid.
Note! – All values of η_∞ - were estimated using a Carreau equation [4].

* agglomerate – a collection of aggregates.

The Krieger-Dougherty [24] equation :

$$\eta_r = \frac{1}{(1-\frac{\phi^*}{\phi_m})^{[\eta]\phi_m}}$$

where: [η], the intrinsic viscosity, is equal to 2.5 for spherical particles, $\phi^* = k\,\phi$, $\phi_m = 64\%$, was used to fit the data but without success. Indeed an upper limit of solid percentage of 22% is predicted which is not evidenced in Figure 64. One possibility, which will be explored now, is to adjust the value of k for each composition. This means that the spheres of the Krieger-Dougherty model are considered as soft. Let us remind that 1/k is the compactness of the aggregate; it increases up to the maximum value for a random arrangement of spheres.

Solid fraction (% vol.)	**k**	**Effective solid fraction (%vol.)**	**1/k (%)**
2	3	6.0	33
5	2.5	12.5	40
10	2.35	23.5	43
20	2.1	42.0	48
30	1.7	51.0	59

Table 11. Variations of k (and 1/k, the compactness) with volume fraction of solid.

In Table 12, the quantity of trapped liquid, $(k-1)\phi$, is compared to the amounts of the different organic components.

Solid fraction (%vol.)	**Trapped liquid (% vol.)**	**Carnauba wax + EVA (% vol.)**	**Paraffin wax (% vol.)**
10	13.5	27	63
20	22	24	56
30	21	21	49

Table12. Comparison of the trapped liquid content in the agglomerates with the volume fraction of each component.

It can be noticed that k decreases in such a way that the quantity of trapped liquid is less than or comparable to the volume fraction of EVA + carnauba wax liquid. This can be related to the fact that the three liquid phases, EVA carnauba wax, paraffin are immiscible and

that the latter does not show any affinity for oxide surfaces. Let ϕ_L be the liquid fraction of carnauba wax and EVA and let us assumed that they are totally trapped into the aggregates, then;

$$(k-1)\phi = \phi_L (1-\phi)$$

which gives an upper limit for k. This happens to be indeed the case as depicted in Figure 65. More precisely, the upper limit is attained for solid fractions higher than 20 vol. %.

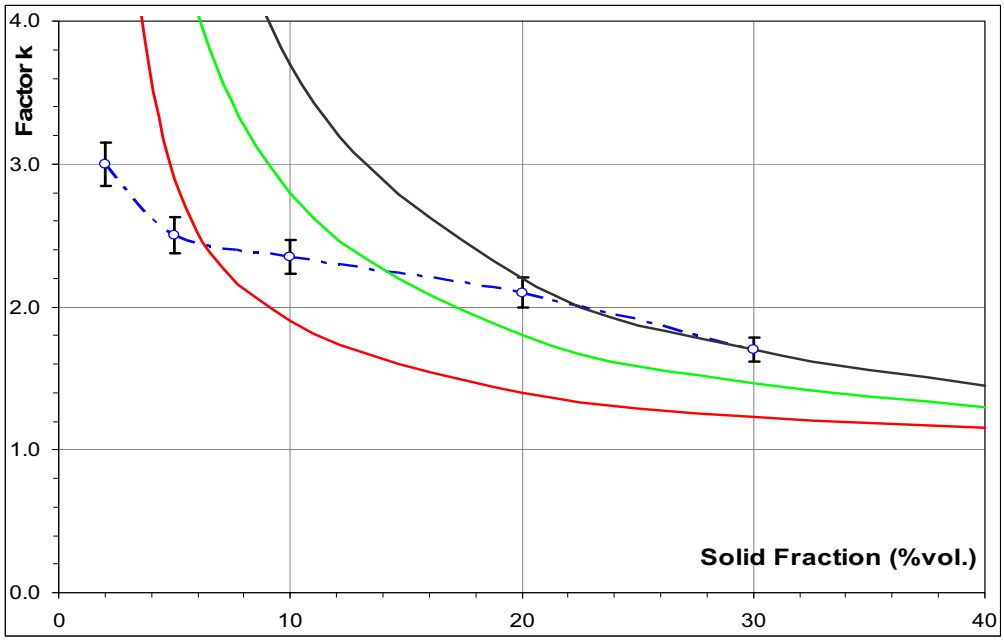

Figure 65. Variation of factor k with vol. fraction of the powder. Lines: %vol. EVA + carnauba (Black), % vol. EVA (Green), % vol. carnauba wax (Red), experimental points (Blue).

Once again, it is concluded that the powder segregates in the EVA **and** carnauba wax phases but not in the paraffin one. Moreover this gives confidence in the use of the Krieger-Dougherty model.

In order to precise the respective roles of EVA and carnauba wax, another composition was studied, namely Car20-EVA10-Par70 instead of EVA20-Car10-Par70, keeping the same ratio of (Car + EVA) over paraffin. The flow tests have been performed according to the protocol already described. Very similar observations have been made and the same canvas has been used for the interpretation.

In Figure 66, the quantity of trapped liquid (k-1) ϕ is plotted versus ϕ.

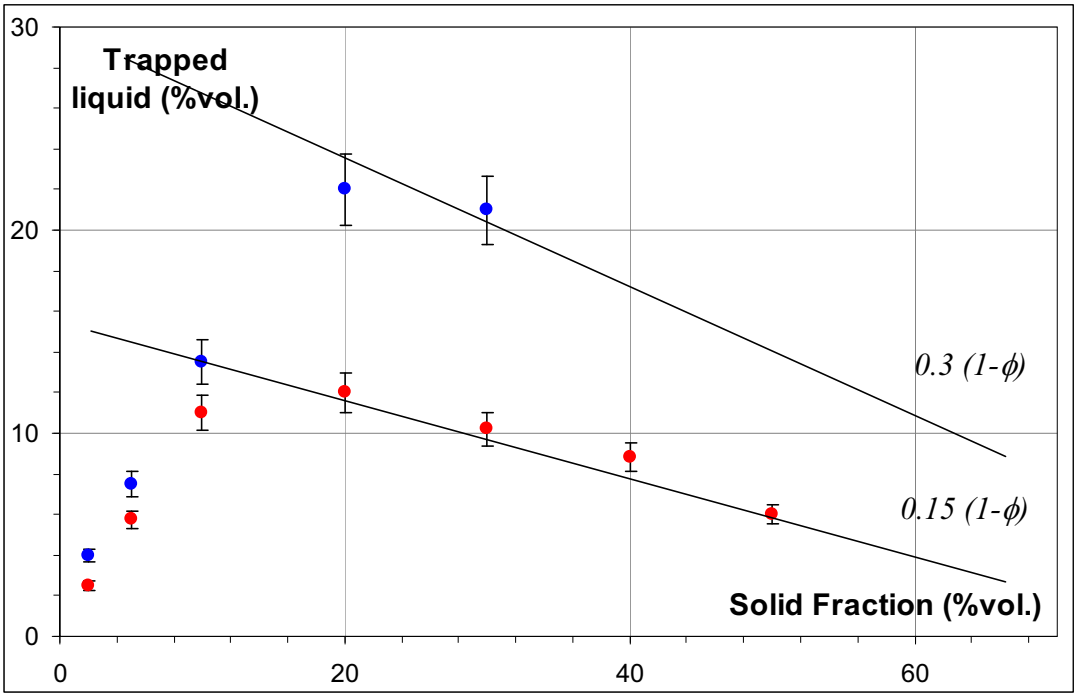

Figure 66. Trapped liquid as a function of the solid fraction for the two compositions . EVA20-Car10 (Blue) and EVA10-Car20 (Red).

It is noted that 30=20 (EVA) +10 (Car), 15=10 (EVA) +5 (Car). i.e. the volume fraction of adsorbed Carnauba is half of the adsorbed EVA. In the case of EVA10Car20 there is an excess of Carnauba.

In Table 13, the values of k determined for the various solid fractions are compared for both compositions.

Solid fraction (%vol.)	**EVA20-Car10 k (1/k)**	**Trapped liquid (%vol.)**	**Car20-EVA10 k (1/k)**	**Trapped liquid (% vol.)**
2	3.00 (33.0%)	4	2.25 (44.0%)	2.5
5	2.5 (40.0%)	7.5	2.15 (46.5%)	5.75
10	2.35 (42.5%)	13.5	2.10 (47.6%)	11
20	2.10 (47.6%)	22	1.60 (62.5%)	12
30	1.70 (59%)	21	1.34 (74.6%)	10.2

Table 13. Comparison between the pastes with different EVA-carnauba wax ratios.

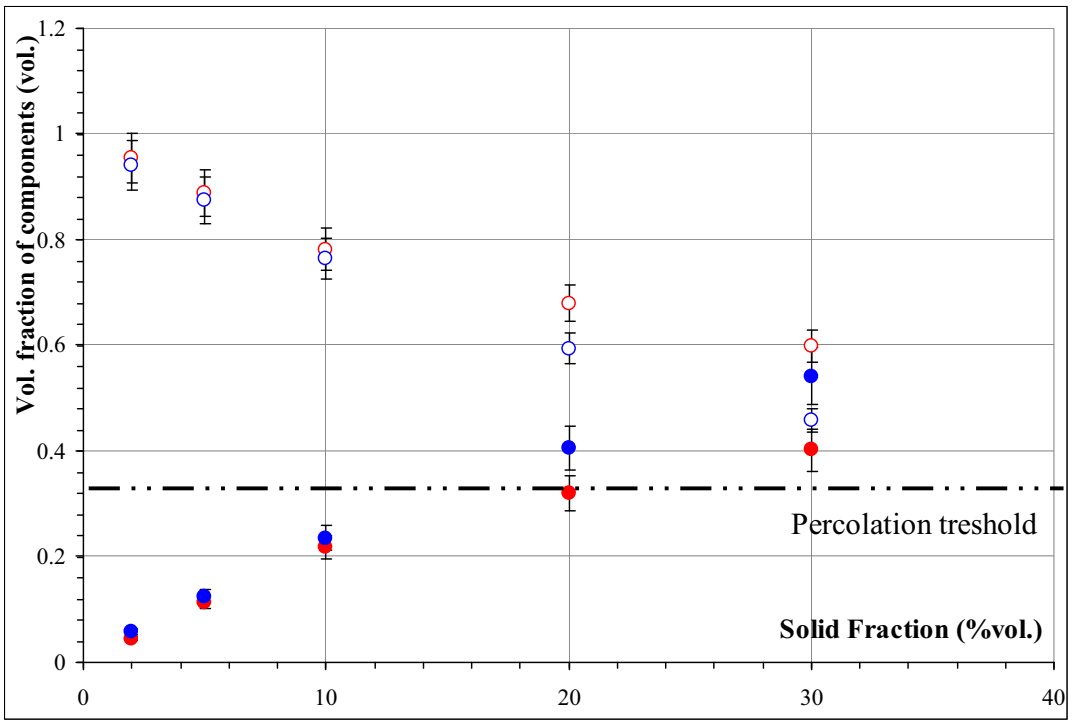

Figure 67. Apparent volume fraction of solid, kϕ full dots, and of free liquid, (1-ϕ*) (open dots). Two compositions Car20-EVA10-Par70 (Red), Car10-EVA20-Par70 (Blue).

In Figure 67, the apparent volume fraction of solid and the volume fraction of free liquid are plotted versus the solid fraction and compared to the theoretical percolation threshold of 1/3. For a solid fraction of 20%vol., taking into account the trapped liquid, the percolation threshold is attained, which is equally true for the two compositions EVA20Car10 and EVA10Car20**.**

III.2.2 The low shear stress microstructure.

On decreasing the shear stress, two important phenomena are expected to take place:

1 coalescence of liquid drops of the same composition to minimize the surface energy,

2 agglomeration of the aggregates identified at high shear stresses to make larger flocs, which may explain the shear thinning rheological behaviour [25].

Knowing the affinity of oxide surface for EVA and carnauba molecules, it is expected that the agregates are not dispersed randomly in the organic liquid but are concentrated in the EVA and/or carnauba wax phases [26, 27]. SEM observations were made at room temperature to ascertain this point although one must be conscious that several phenomena may happen on cooling.

Anyway, observations demonstrate the inhomogeneity of the microstructure with the existence of two phases and the presence of the powder only in one of them. Taking into account the previous results, these are identified with the two phases, paraffin and the 2/1 blend. The agglomerates are also clearly visible – see Figure 68.

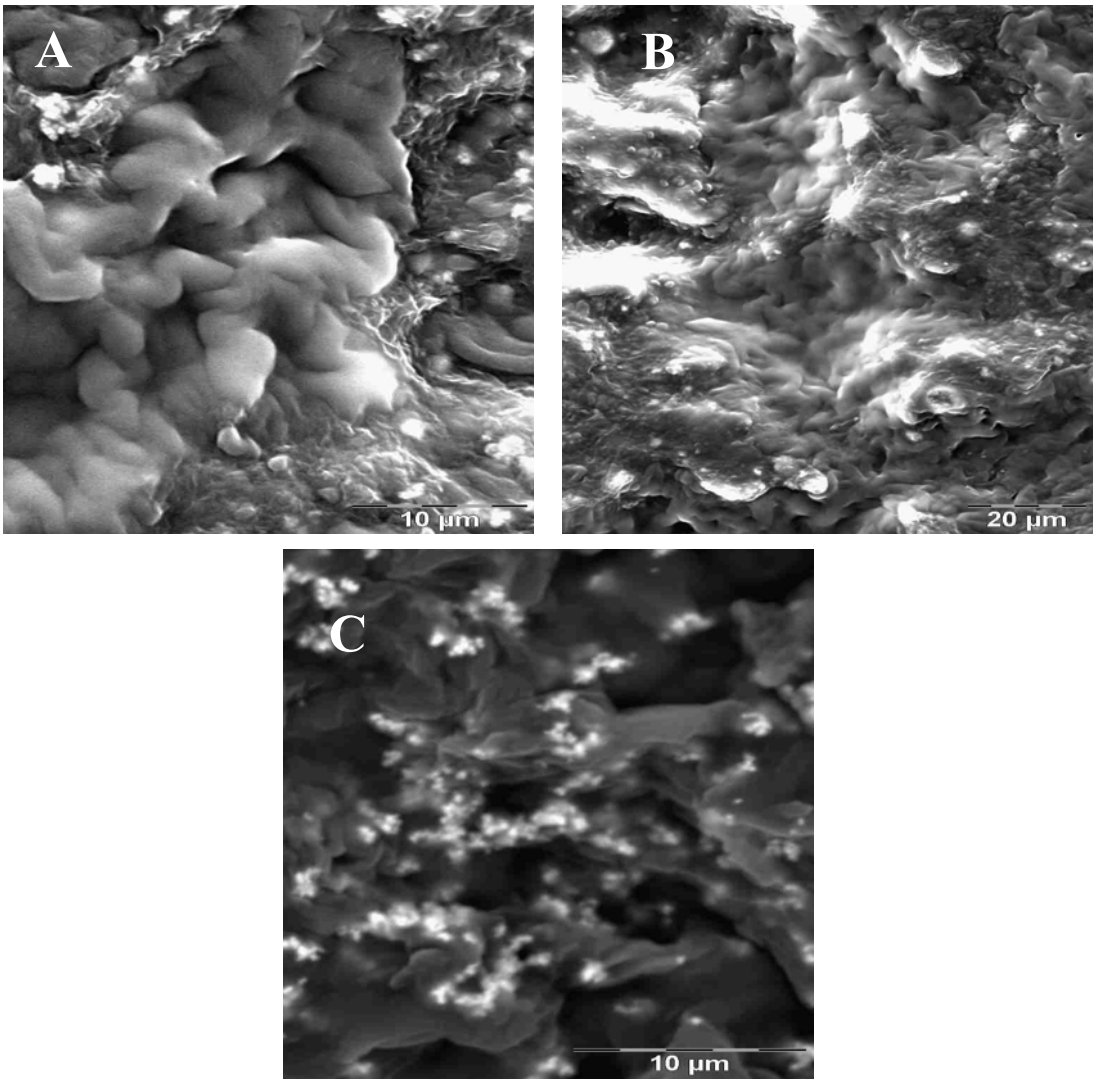

Figure 68. SEM observations.
A,B EVA20Car10 composition , resp 2%vol., 5% vol. solid fraction,
C –EVA10Car20 composition , 5%vol. solid fraction

In Table 14, the free (EVA + carnauba) liquid content is calculated for the two compositions. As can be seen, for solid fraction of 2% and 5% vol., the agglomerates occupy a minor part of the inclusions* and therefore, it is not surprising that the shear thinning effect is only slight.

* inclusion – closed drops of liquid with or without solid in it.

	"Free liquid" (% vol.)		Effective solid fraction (%vol.)	
Solid Fraction (%vol.)	**EVA20Car10**	**EVA10Car20**	**EVA20Car10**	**EVA10Car20**
2	25.8	27.1	6.0	4.50
5	21.0	22.7	12.5	10.75
10	13.5	16.0	23.5	21.00
20	2.0	12.0	42.0	33.00
30	0.0	10.8	51.0	40.20

Table 14. Amount of free liquid phases for the two compositions.

The situation reverses when the solid fraction is increased from 5% to 10% vol. Then, the agglomerates occupy most of the inclusions volume. Moreover, the effective solid fraction approaches the percolation threshold of 1/3. The two reasons may explain the large jump in the viscosity ratio η_o/η_∞ from 2 to 1000.

For a solid fraction of 20% vol., a new feature appears in the flow curve, i.e. the existence of an intermediate plateau of viscosity.

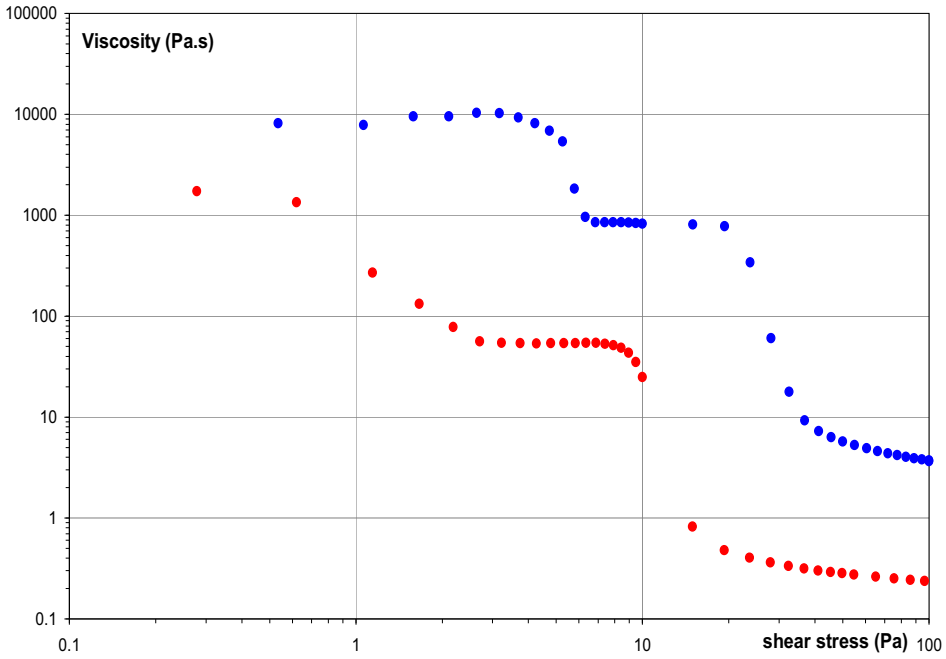

Figure 69. Flow curve on a log-log scale.
Two compositions EVA20-Car10 (Red), EVA10-Car20 (Blue).

One clue for the interpretation is found in Table 14 : the free liquid has almost disappeared and the effective solid fraction has over passed the volume percolation threshold of 1/3. It is also noticed that the intermediate plateau of viscosity is comparable to the viscosity of the 10% vol. sample. It is thus proposed that the microstructure can be described

as a network of interacting dense and deformable inclusions. The first decrease in viscosity is due to the disruption of the network of inclusions while second decrease corresponds to the fragmentation of them, a mechanism already operative for lower solid fractions. Increasing the solid fraction to 30% vol. displaces the stresses at which the two mechanisms are active, i.e. the interactions between inclusions become stronger and the inclusions themselves become harder (and more compact). These conclusions are equally valid for the two compositions EVA20Car10 and EVA10Car20**.**

In the case of the composition EVA20Car10**,** it has already mentioned that the rheological behaviour changes abruptly when the solid fraction increases from 30 to 40%vol. In the letter case, almost no viscoelasticity, a negligible thixotropy and only one jump of viscosity are observed. SEM observations suggest that the paste has become homogeneous, see Figure 70.

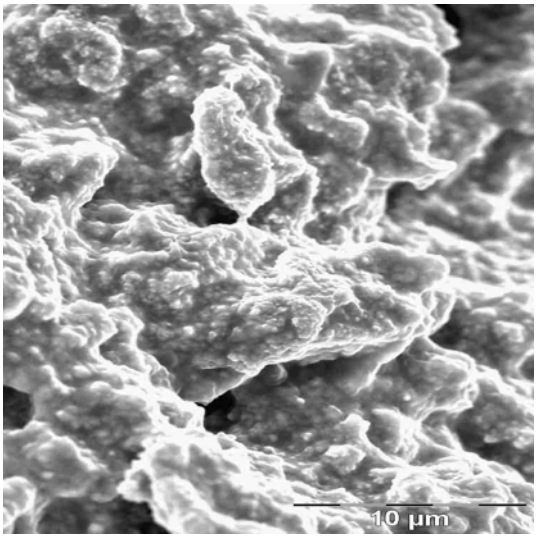

Figure 70. SEM micrograph. Composition EVA20Car10, 40%vol. solid fraction.

Indeed, two necessary conditions are met:

- the ratio EVA/(carnauba wax) is equal to 2, the exact composition of the organic phase adsorbed on the surface of the grains.
- all the (EVA + carnauba wax) is adsorbed on the solid surface, no free liquid is left.

These two conditions are not verified in the case of the EVA10Car20 composition as proved by the data of Table 15 and therefore, a different behaviour is expected, which is indeed observed, see Figure 71.

	EVA20Car10		EVA10Car20	
%vol. Powder	**Carnauba wax (% vol.)**	**EVA (% vol.)**	**Carnauba wax (% vol.)**	**EVA (% vol.)**
2	8.5	17.2	18.7	8.1
5	7	14	17	5.3
10	4.5	9	14.3	1.7
20	0	0	12	0

Table 15. Volume fractions of EVA and Carnauba wax in the free liquid.

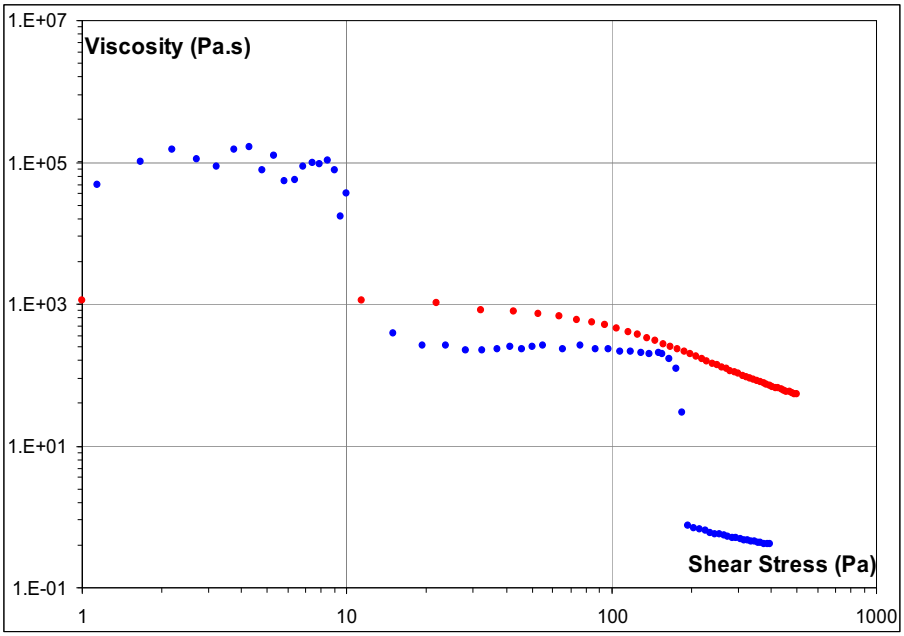

Figure 71. Flow curves for a solid fraction of 40%vol.
Two compositions EVA20-Car10 (Red), EVA10-Car20 (Blue).

The flow curve is qualitatively similar to those obtained for lower solid fractions, i.e. two jumps in viscosity with an intermediate plateau, accompanied with viscoelasticity and thixotropy, compare with Figure 69. SEM observations confirm the inhomogeneity of this paste.

Summary on the EVA20-Car10 composition..

During the mixing step, EVA and carnauba molecules are adsorbed on grain surfaces in a ratio 2/1. EVA binds grains together forming hard aggregates, which cannot be destroyed by the highest applied shear stresses.

- Compositions 2, 5, 10vol.% solid fractions : the volume of trapped liquid is lower than the volume of (EVA + carnauba wax) and the volume of aggregates is less than the percolation threshold ; on decreasing the shear stress, the aggregates form agglomerates which are isolated and immersed in inclusions of liquid EVA and/or carnauba wax.
- Compositions 20, 30vol. % solid fractions : the volume of trapped liquid is more or less equal to the volume of (EVA + carnauba) wax and the volume of aggregates is larger than the percolation threshold ; on decreasing the shear stress, the agglomerates form and interact.
- Compositions 40, 50, 60vol.% solid fractions. The agglomerates loose their identities and the paste is homogeneous.

This is further substantiated by SEM observations, see Figure 72– A in the first case, B,C in the second, D in the third one.

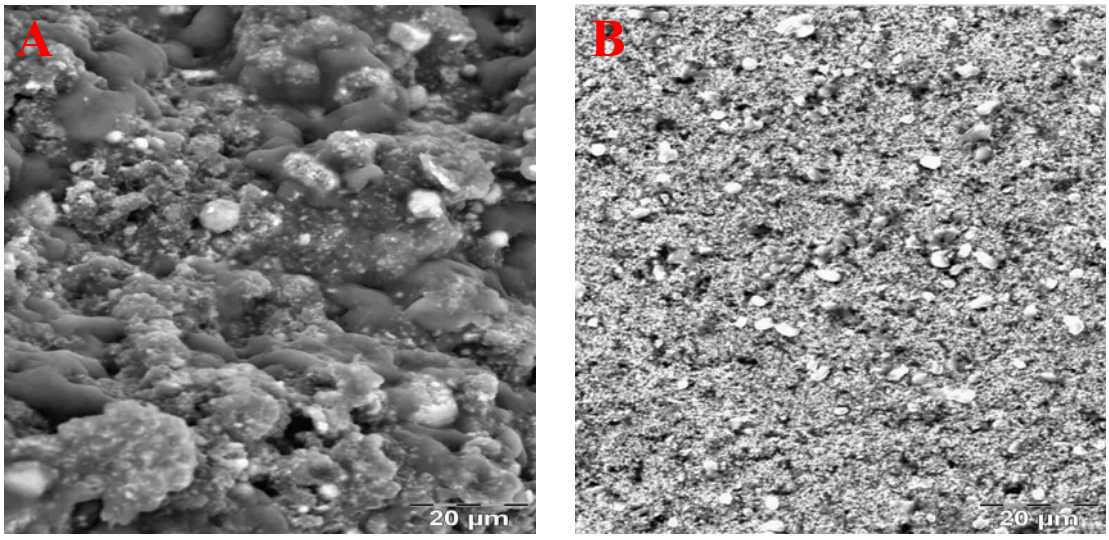

Figure 72. SEM observations (EVA20-Car10 composition).
A- 10%, B – 20%, solid fraction.

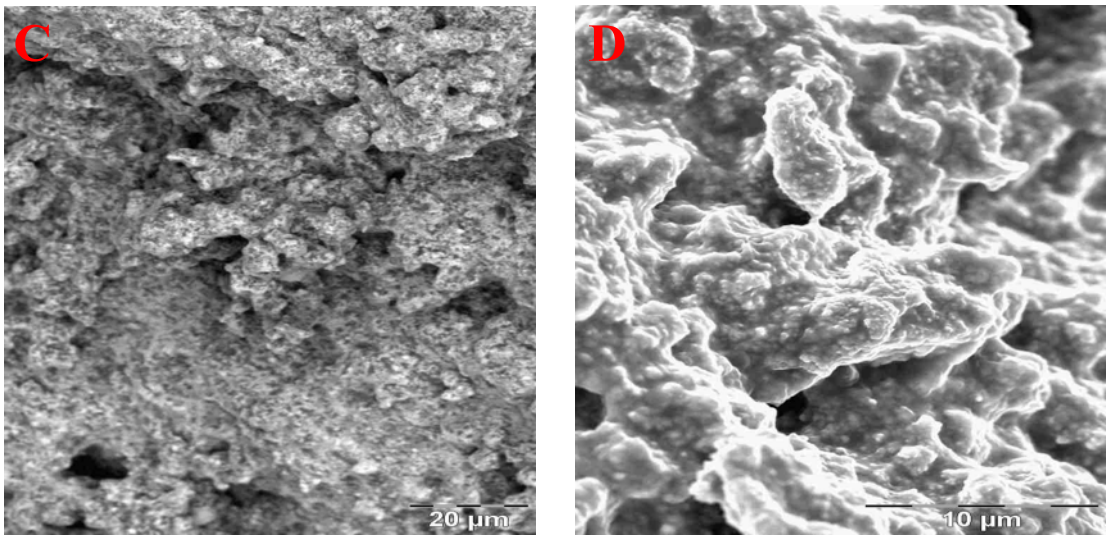

Figure 72. SEM observations (EVA20-Car10 composition).
C – 30%, D – 40% vol. solid fraction.

III.3 Viscoelasticity.

III.3.1 Stress sweep.

A preliminary stress sweep is necessary to determine the conditions in which the response is linear [28, 29]. This is done at a fixed frequency (6.25 rad/sec) and the criterium is a decrease of $|\overline{G}|$ of 10%, see Figure 73.

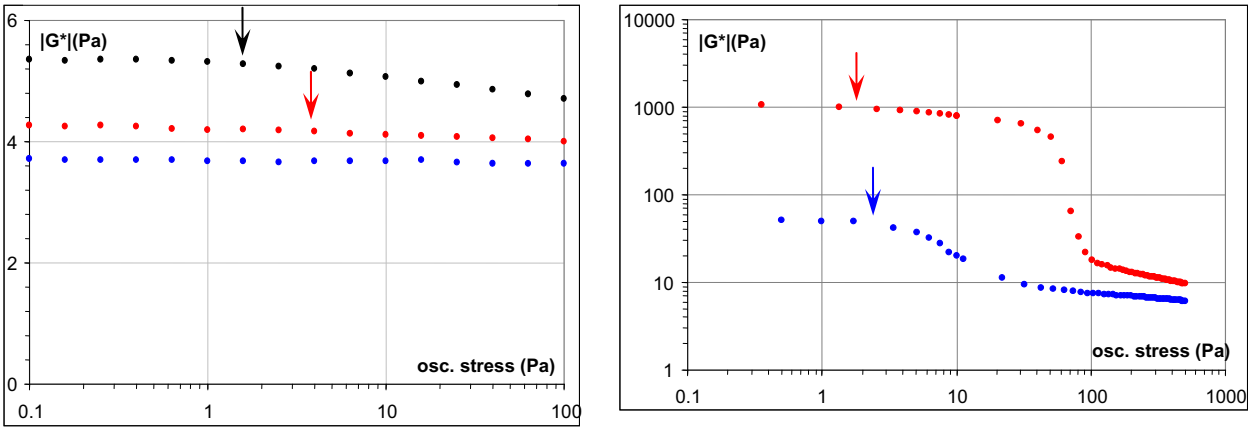

Figure 73. Oscillation experiment – stress sweep test. Arrows delineate the limit of linear stress range.
Left : 0% (Blue), 2% (Red), 5% (Black) vol. solid fraction.
Right 10% (Blue), 20% (Red) %vol. solid fraction.

- 0 %vol. solid fraction. The blend shows a linear response in the complete investigated stress range (0-500 Pa).
- 2,5,10 %vol. The stress interval where the response is linear corresponds to the viscosity plateau at low stresses, i.e. the structure remains undestroyed and stable.
- 20 %vol. The first jump in viscosity, already reported in flow tests (see III.1) is not observed in dynamic tests.
- For higher solid fractions the critical stress corresponding to the limit of linear viscoelasticity is so low that measurements are no longer feasible.

Same observations can be done for the two formulations, EVA20-Car10 and EVA10-Car20**.**

III.3.2 Frequency sweep.

- EVA20-Car10 composition.

In Figure 74 are depicted the variations of G' as a function of frequency for the different solid fractions.

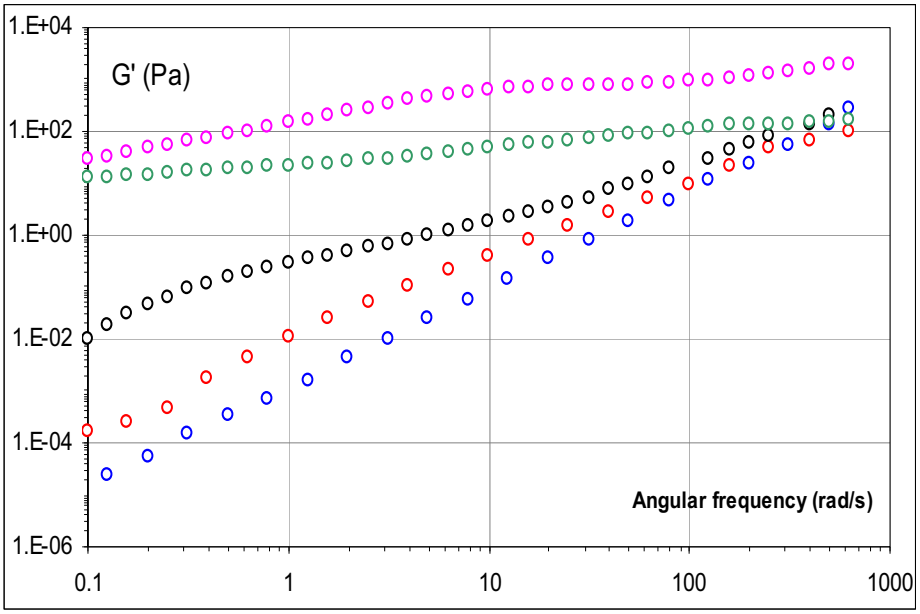

Figure 74. Frequency dependence of the storage modulus G' in a log-log plot, for different solid fractions : 0%vol.(Blue), 2%vol.(Red), 5%vol. (Black), 10%vol. (Green), 20%vol. (Purple).

In the case of the blend, G' varies as ω^2 (G" as ω) and the Maxwell model is adequate to describe mathematically the experimental results. η_o is equal to the value determined in flow tests, 0.6 Pa.s) while G_o is of the order of 1000. η_o/G_o has the dimension of a time

constant and is equal to 6.0 10^{-4} s. Indeed, a representation of the data in the complex plane, see Figure 75 Right, shows that only a small part of the semicircle is obtained.

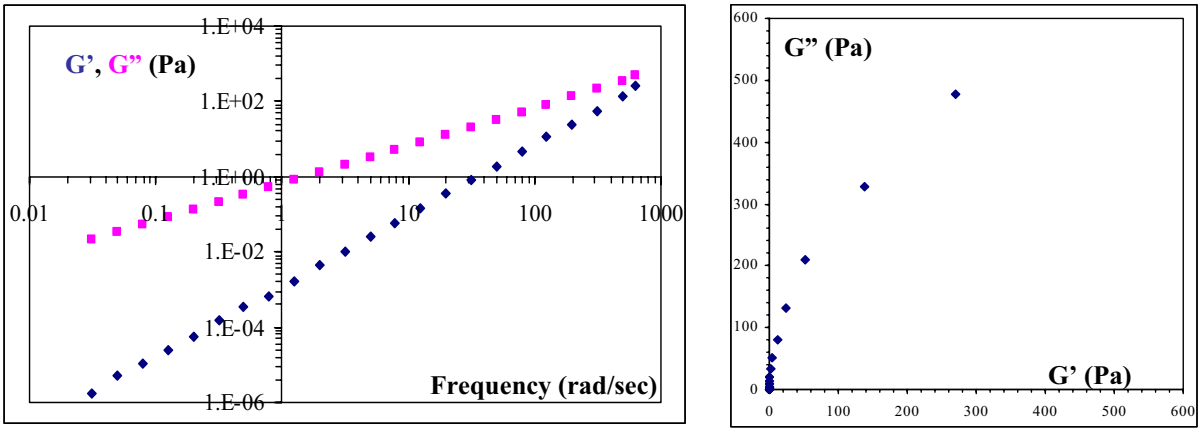

Figure 75. Frequency dependence of G' and G" for the blend : Left) as a function of frequency, Right) Cole-Cole plot (G", G')

Addition of the powder to the blend has a noticeable effect with an increase of both moduli, G' and G", at all frequencies [30-35].

In Figure 76 are reported J' and (J"ω) as a function of frequency for the 5%vol. solid fraction sample. The choice of J' and (J"ω) instead of G' and G" has been made because, in the former case, the first two terms describing the stationary elastic and viscous behaviours, contribute only a constant background (resp. $1/G_o$ and $1/\eta_o$) and this makes much more apparent the contribution of any distribution of time constants.

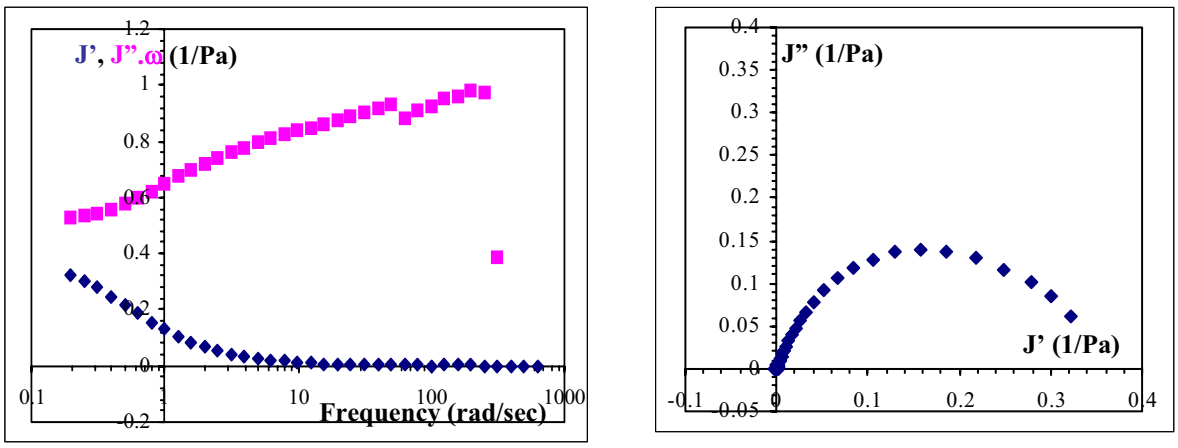

Figure 76. J' and (J". ω) (5%vol. solid fraction) : Left) as a function of frequency. Right) – Cole-Cole plot.

In the case of the organic matrix, J' and (J"ω) are indeed constant as expected, while for 2%vol. fraction of solid, a small dispersion can be seen. In the case retained in Figure 76

(5%vol. of powder) the dispersion is well defined. Clearly a distribution of time constants is associated with the addition of the powder. At high frequencies, J' tends towards a constant (1/Go), substantially the same as that of the blend, about 10^{-3}. J' and [J"-1/($\eta_o\omega$)] are plotted in the complex plane, drawing a deformed semicircle[36].

It has been emphasized that a creep experiment is another way to study viscoelasticity. Results obtained for 0, 2, 5, 10 and 20%vol. are presented in Figure 77. Once again, a viscoelastic response is observable for a minimum solid fraction of 5vol%. After 350 seconds, the strain linearly increases with time, i.e. the behaviour is viscous.

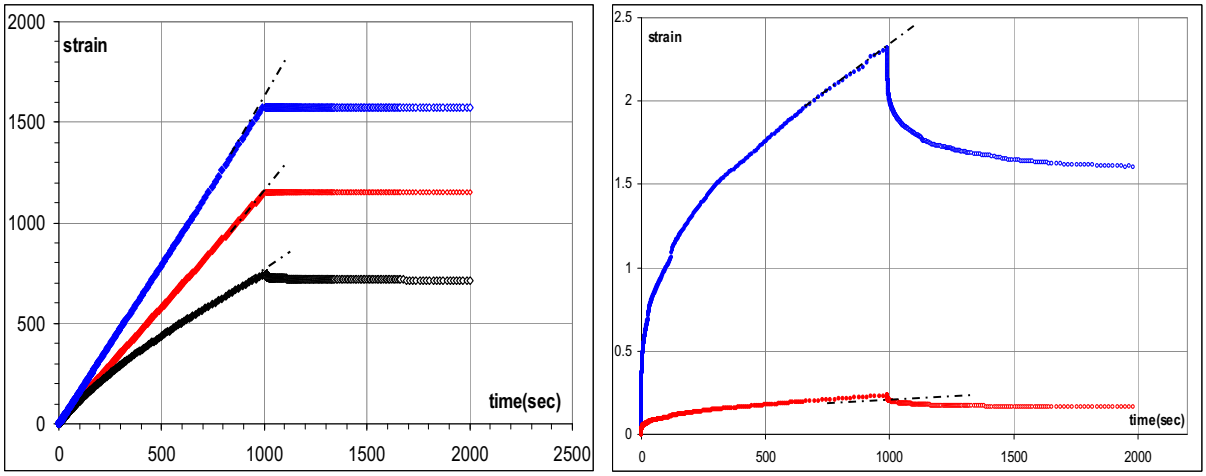

Figure 77. Creep curve : full points (σ=1 Pa), recovery curve : open points (σ=0 Pa). Left) Blue curve – 0%, Red – 2%, Black - 5% vol. solid fraction. Right) Blue curve 10%, Red curve 20%vol. solid fraction.

The quantitative determination of the time distribution function f(lnτ) from the experimental data (creep or oscillation) is called an inverse problem. When noise is present, which is unavoidable, the problem is ill-posed, i.e. difficult to solve. We have used CONTIN, a portable FORTRAN package for inverting noisy linear operator, i.e. of the form :

$$y_k = \int_a^b F_k(Ln\,\tau)\, s(\tau)\, d(Ln\,\tau) + \sum_i L_{ki}\,\beta_i + \varepsilon_k$$

where the index k represents the different times (creep test) or frequencies (oscillation sweep) of the experiment, y_k the measured quantity (strain in our case) ; the $\sum_i L_{ki}\,\beta_i$ term permits the fit of a superimposed background, ε_k the unknown noise component of the measurement. For more details, refer to [37]. Results of the calculation are presented in Figure 78.

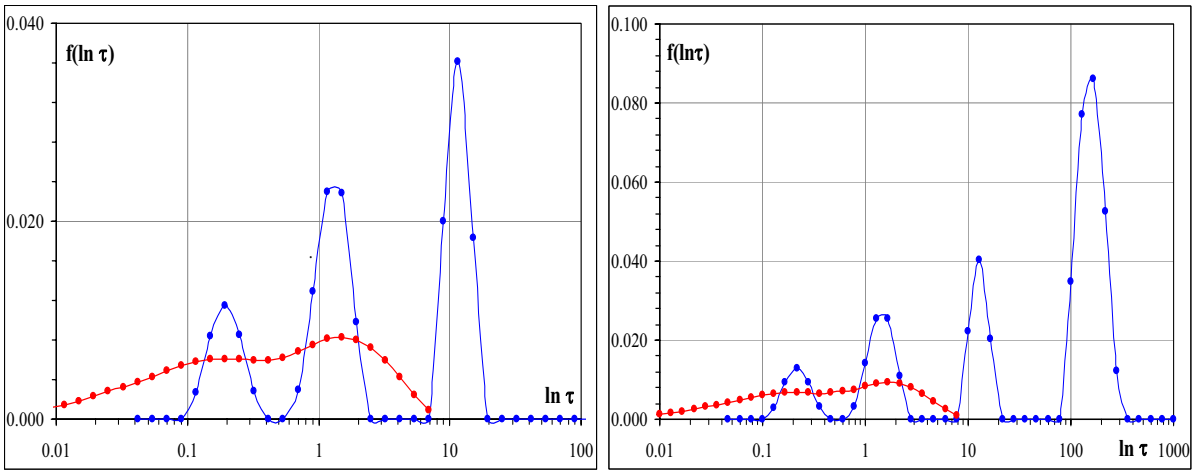

Figure 78 Distribution of time constants f(ln τ) deduced from an oscillation experiment (red), from a creep experiment (blue). Results for 5%vol. (Left) and 10%vol. (Right) solid fraction.

A good agreement is observed in the medium range of time constants. The peaks are broader when determined from the oscillation sweep experiment. This arises because the data are more noisy but the peaks are located at the same values of the time constant. As expected, the creep test gives more information at large τ's and the oscillation sweep experiment at short τ's.

In Figure 79, J' and [J"-1/($\eta_o\omega$)] are plotted in the complex plane for 10% vol. solid fractions.

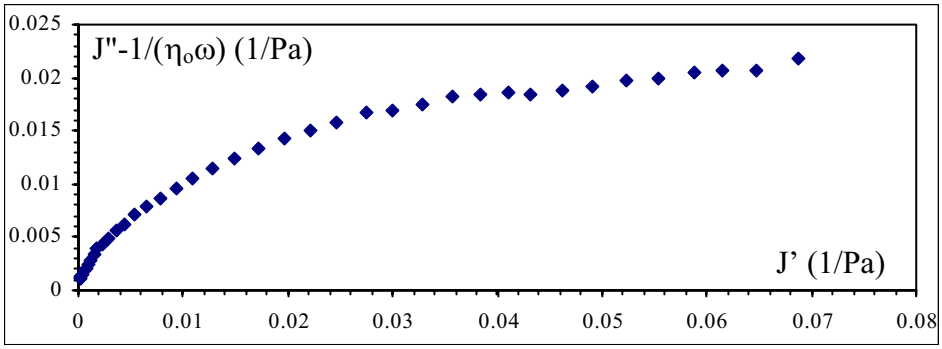

Figure 79. J' and [J"-1/(ηoω)] data (10%vol.solid fraction) presented as a Cole-Cole plot

For 10%vol. the figure is still a deformed semicircle, in agreement with the CONTIN analysis. In Figure 80, J' and [J"-1/($\eta_o\omega$)] are plotted in the complex plane for 20% vol. solid fractions.

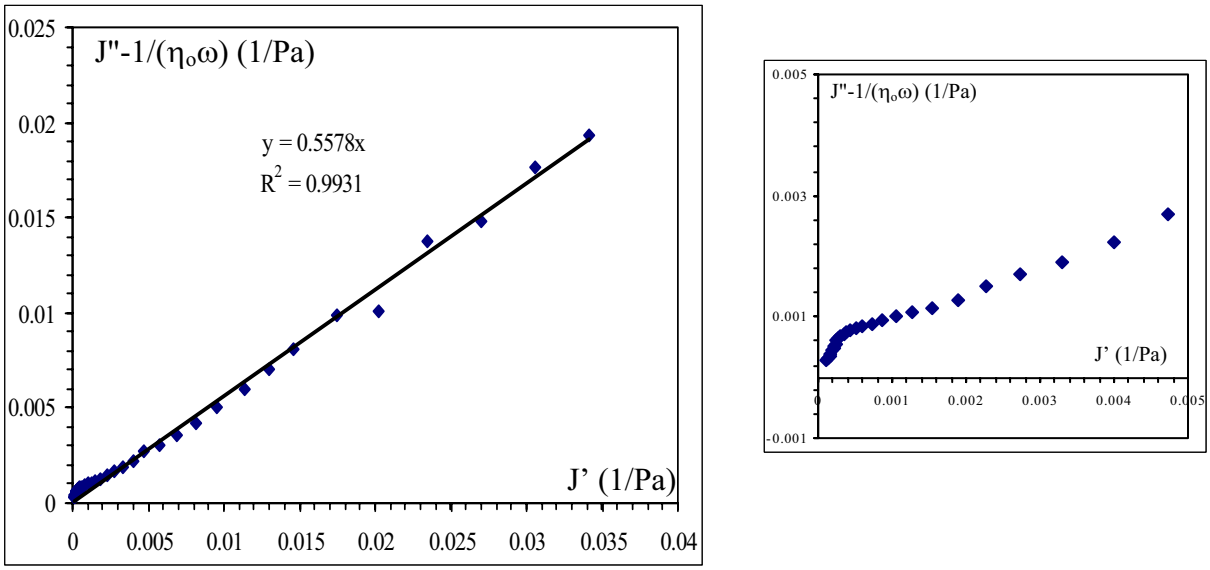

Figure 80. J' and [J"-1/(ηoω)] data depicted in a Cole-Cole plot (20%vol.solid fraction). Right) zoom around the origin of the left figure.

The Cole-Cole plot is a straight line, although some magnification reveals a small high frequency semicircle. This evolution confirms the formation of a network for a solid fraction between 10% and 20%vol. [36, 38]

- **EVA10-Car20** compositions.

It is interesting to compare the results obtained for the two compositions EVA20Car10 and EVA10Car20. In Figure 81, which can be compared to Figure 74, G' is depicted versus frequency. For 2% and 5%vol. solid fractions, the curves are very similar with the growing contribution of a distribution of time constants at low frequencies.

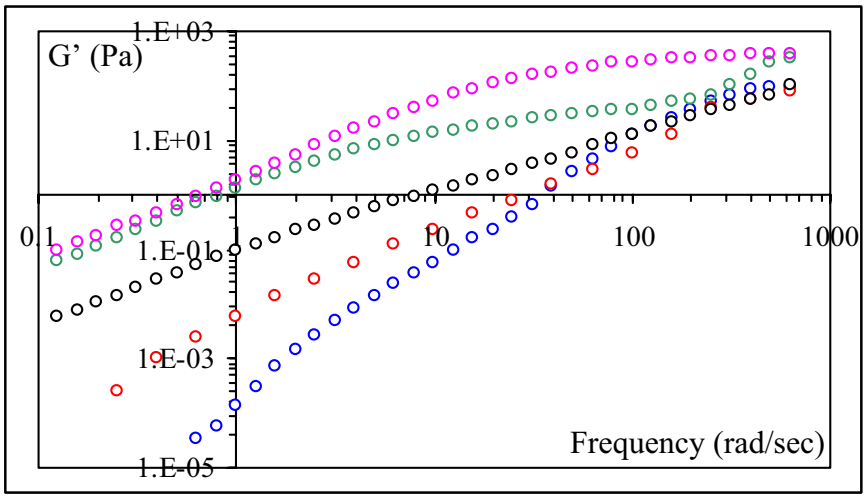

Figure 81. Frequency dependence of the storage modulus G' at various solid fractions : 0%vol (Blue)., 2%vol. (Red), 5%vol. (Black), 10%vol. (Green), 20%vol.(Purple).

Plotted as J' and J"ω versus frequency in Figure 82, the data show a continuous evolution of this distribution incorporating longer and longer time constants when increasing the solid fraction up to 20%vol.

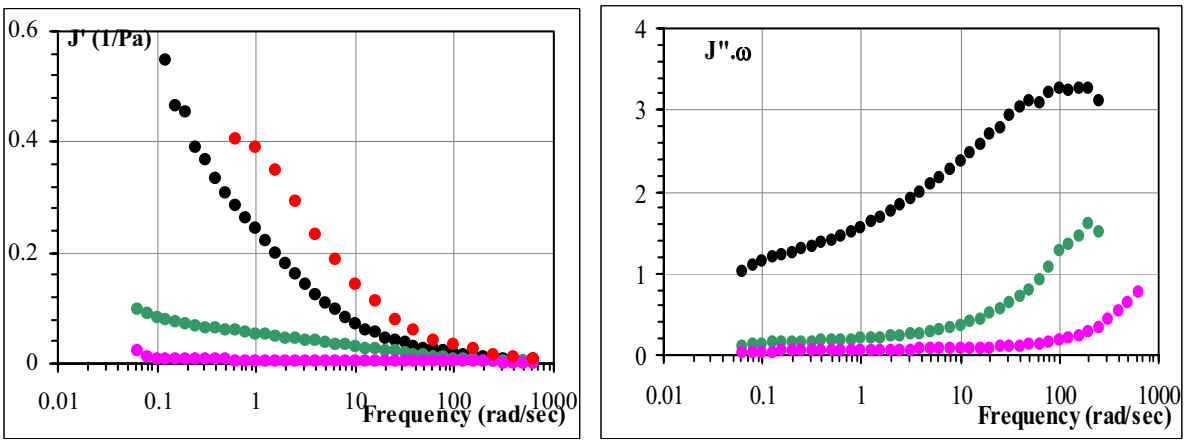

Figure 82. Frequency dependence of J' and (J"ω) for different solid fractions: 2%vol. (Red), 5%vol. (Black), 10%vol. (Green), 20%vol.(Purple).

This is quite different from the results obtained with the composition EVA20Car10, for which a transition solid-liquid was evidenced. This is further exemplified in Figure 83 (compare with Figure 80) using a Cole-Cole representation.

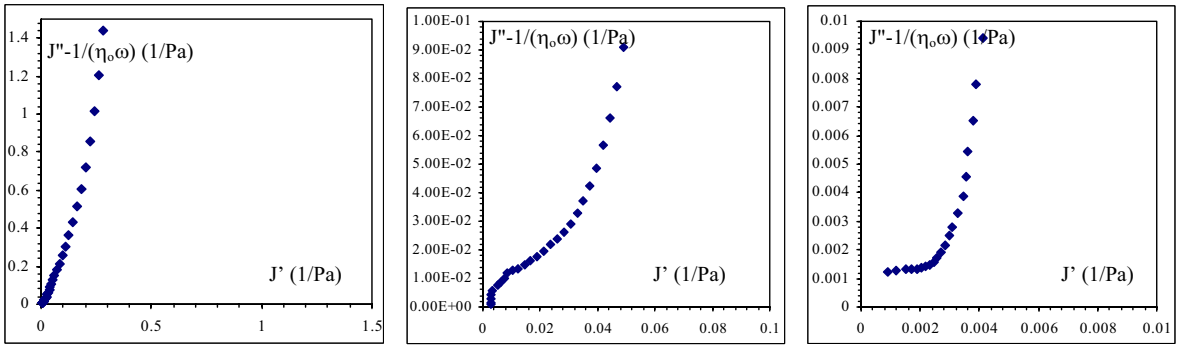

Figure 83. Cole-Cole plots for 5 (Left), 10 (Center) and 20 (Right) % vol. solid fraction.

The small circle at high frequencies was already seen in Figure 80 and could be related to the interactions of EVA molecules with the grains surfaces

III.4 Thixotropy.

The word "thixotropy" is used with different meanings [39]. According to Barnes [40] in his comprehensive review of thixotropy, people using this word fall into two camps : first those who understand it as the time response of the microstructure brought about by shearing or resting. In this sense, all materials are thixotropic, although the characteristic time can be so short that it is not experimentally accessible (<30 ms with our rheometer). Thus, it can be said that the paste with 0-2-5%vol. fraction of solid are not thixtropic while all other pastes were thixotropic. Secondly there are those who understand thixotropy in the sense of conferring solid-like elastic properties to a flowable fluid and vice versa. This is very often associated with extremely shear thinning, although a different aspect. In this more restricted sense, only those pastes with 50 or 60%vol. were thixotropic. In the following, we shall refer to the second definition.

Coussot [41] has proposed a physical basis to rheology, what he calls rheophysics; the fluid is considered as a collection of elements. The displacement of one element, which produces some flow, necessitates to overcome a potential barrier and this supplement energy is brought through shearing, i.e.$E=\sigma\, b^3$ if b is the average distance between two elements. The rate of deformation is proportional to the fraction of elements which are displaced per unit of time:

$$\dot{\gamma} = \Psi(E)$$

This equation implicitly assumes that the energy E is immediately returned to the medium after the displacement, for instance through Brownian motion. However, the cooperative aspect of flow makes this hypothesis very crude except for simple fluids. To take into account this delayed response, it is assumed that the energy of the barrier is E+W where W depends on the environment or equivalently the microstructure. If the latter can be characterized by a unique scalar λ, then the most general formulation is given by :

$$\begin{aligned} \dot{\gamma} &= \Psi(E + W(\lambda)) \\ \lambda(t) &= F\ \ (\lambda_o, \dot{\gamma}(t' < t)) \end{aligned} \qquad (1)$$

where F is an unknown functional and λ_o is the initial state of the fluid. Most often, F is of the form :

$$\frac{dW}{dt} = f_1(W,\sigma) - f_2(W,\sigma)$$

i.e. a balance between the tendency to restore a rest state and the disruption due to shearing. In the stationary state :

$$f_1(W,\sigma) = f_2(W,\sigma)$$

This coupled with equation (1), gives the rheological law.

In this system, primary particles are bounded through EVA and form a continuous network. In order to induce flow, this network must be disrupted and this does not occur instantaneously [42, 43]. This is the origin of observed thixotropy. In the following we shall present and use a model proposed by P. Coussot and A.I. Leonov [44], taking advantage of two complementary approaches of the authors. A. I. Leonov [45, 46, 47] has developed a general theory, i.e. constitutive equations, of the rheological behaviour of polymeric liquids based on thermodynamics. The most important feature of these fluids is that they can accumulate large recoverable strains while flowing. Flow is a considered as a deviation of a quasi-thermodynamic equilibrium, that of the elastically deformed material.
This may be coupled to the considerations of P. Coussot to give the following model. Its most remarkable feature is that there is a yield stress but there is no yield criterion which governs the transition from solid like elastic gel behaviour to flow.

Two types of interaction are considered :

$$\sigma = \sigma_{el} + \sigma_m$$

- σ_{el} : Strong attractive interactions exist between the particles and are responsible for the formation of the network. These are assumed to be basically elastic, but when a critical elastic strain, γ_c (<<1), is attained, irreversible deformations also occur which result in a viscoelastic behaviour, described by a simple Maxwell equation

$$\frac{1}{G}\frac{d\sigma_{el}}{dt} + f(\xi)\frac{\sigma_{el}}{\eta_p} = \dot{\gamma}$$

where G is an elastic modulus. The viscosity η_p characterises an elementary drag for the flocs in the liquid and f(ξ), where ξ (0≤ξ≤1) is the fraction of broken bonds between the particles, takes into account the influence of the environment.

If ξ equals zero, the mathematical condition f(0)=0 is equivalent to assume that the material behaves as a pure elastic solid. Moreover, f(ξ) must be a regular, increasing function of ξ. The authors propose to define f(ξ) as :

$$f(\xi) = \frac{\left[(1-\xi)^{-n} - 1\right]}{n}$$

which becomes simply :

$$f(\xi) = \frac{\xi}{1-\xi}$$

if n equals 1.

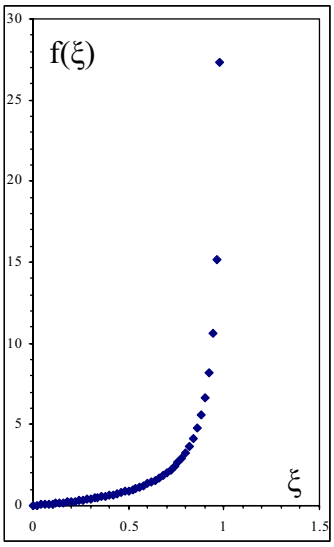

Figure 84. f(ξ) n=1.

- σ_m : Hydrodynamic interactions between flocs, as in suspensions of inactive particles with a viscosity η_m, function of the particle concentration.

  $$\sigma_m = \eta_m \dot{\gamma}$$

The two basic equations can be written in an adimensional form :

$$\Sigma = S + k\,\Gamma$$

$$\frac{dS}{dt'} + f(\xi) S = \Gamma$$

where $\Sigma = \frac{\sigma}{G\,\gamma_c}$, $S = \frac{\sigma_{el}}{G\,\gamma_c}$, $\Gamma = \frac{\eta_p\,\dot{\gamma}}{G\,\gamma_c} = \frac{\theta\,\dot{\gamma}}{\gamma_c}$ $t' = \frac{t}{\theta}$ and $k = \frac{\eta_m}{\eta_p}$, $\theta = \frac{\eta_p}{G}$

Substituting in the second equation an expression of Γ derived from the first equation, it comes :

$$k\frac{d\Gamma}{dt'} + (1 + kf)\,\Gamma = \frac{d\Sigma}{dt'} + f\,\Sigma$$

which can be qualified as a time dependent Burger's model.

Another equation is needed to describe the time evolution of ξ :

$$\frac{d\xi}{dt'} = \frac{1}{\tau}\left[(1-\xi)\Gamma - \xi\right] \qquad (2)$$

an extension of the kinetic equation proposed by Moore. The right-hand side is equal to rate of rupture of the interparticle bonds, which in turn is proportional to the fraction of unbroken

bonds (1-ξ) and the magnitude of the shear rate $|\dot{\gamma}|$, while -ξ/τ is the rate of bond restoration. According to the authors, there can be two long restructuring processes: one approaching the true equilibrium gel structure and another approaching dynamic equilibrium in steady state flows. Therefore, they propose the following expression of τ(Γ,ξ) :

$$\tau = \exp\left[\frac{b}{1 + c\,\Gamma\,(\xi - \xi_1)}\right]$$

This model relies on four material parameters, η_m, η_p, γ_c and G, and three other parameters, n, b and c. Different experiments have been performed for their evaluation, experiments at constant shear stress and at constant shear rate. None alone was sufficient to provide the values of these parameters.

- Creep experiment

In a creep experiment, the stress is applied suddenly and this induces, a jump in strain rate :

$$\delta\Gamma = \delta\Sigma / k$$

then, the applied stress is constant in time :

$$k\frac{d\Gamma}{dt'} + (1 + kf)\,\Gamma = f\,\Sigma$$

Later on it will appear that the effective time constant k/(1+kf) (≤k) is indeed very short and this equation reduces to :

$$\Sigma = \left(\frac{1}{f} + k\right)\Gamma \qquad (3)$$

It is emphasized that this not a stationary equation because ξ varies with time but the variations are supposed to be slow enough. This equation, which was not in the original paper, is very interesting because it permits to convert the flow curve into a curve ξ(σ).

The steady state solution is given by :

$$\xi_1 = \frac{\Gamma}{1 + \Gamma}$$

or, taking into account the pseudo stationary state, equ. (2) , ξ_1 is solution of :

$$\{1 + k\,f(\xi)\}\xi = \Sigma\,(1 - \xi)f(\xi)$$

which reduces to

$$\xi\,\{\xi\,(\Sigma - 1 + k) - (\Sigma - 1)\} = 0 \text{ if n=1.}$$

ξ=0 is always solution but another nonzero solution exists if the condition $\sigma \geq 1$ is fulfilled. In case n equals to one ::

$$\xi_s = \frac{(\Sigma - 1)}{(\Sigma - 1 + k)} \qquad (4)$$

and :

$$\Sigma = 1 + k\,\Gamma \text{ or } \sigma = G\,\gamma_c + \eta_m\,\dot{\gamma}$$

i.e. a Bingham law. This is indeed the case, see Figure 85, although some small deviations can be seen, which will be adressed later on.

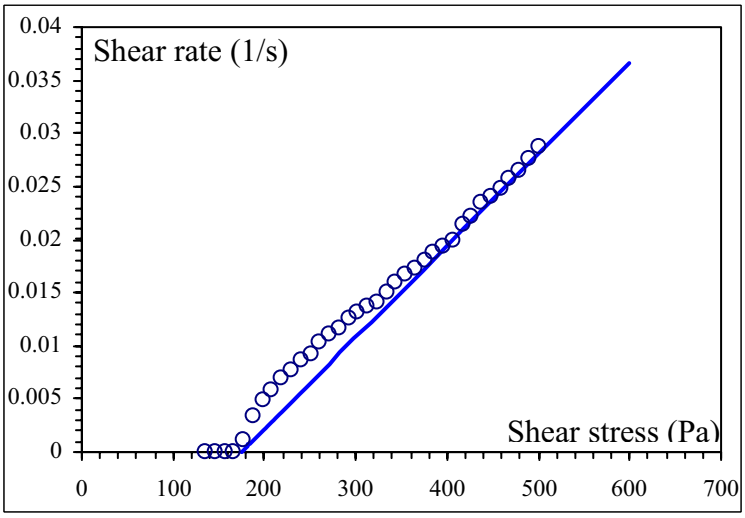

Figure 85. Flow curve experiment. Simulation using a Bingham law (Blue line).

Analysis of the experimental data provides the parameters σ_c (=175 Pa) and η_m=11600 Pa.s.

- "Start shear flow" experiment, i.e. the stress response to a step increase of the strain rate starting from an initial rest state. At the initial time, a jump in strain rate induces a jump in stress :

$$\delta\Sigma = k\,\delta\Gamma$$

then, the applied strain rate is constant in time :

$$(1 + kf)\,\Gamma = \frac{d\Sigma}{dt'} + f\,\Sigma$$

For short times the relaxation time 1/f is large and the response can be considered as elastic,

$$\sigma = G\,\dot{\gamma}\,t$$

in agreement with the experimental data, see Figure 86, whence the elastic modulus G (=43 000 Pa).

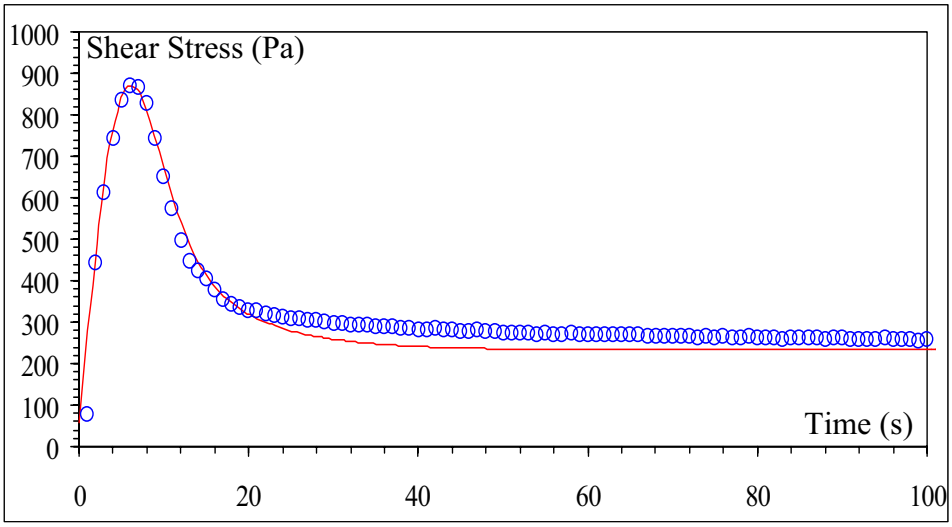

Figure 86.Overshoot experiment. Red line, simulation using the following parameters (see text). b=2.85, c=0, θ=1.75 s, $\dot{\gamma}$ = 5 10^{-3} s^{-1},

The critical strain ($\gamma_c=\sigma_c/G \cong 0.004$) is infinitesimal as required by the theory. Then the stress increases up to a very high value, much higher than the critical stress and this is due to the fact that ξ relaxes slowly towards its equilibrium value.

- The kinetics.

The analysis of the kinetics brings further information on the parameters b and c and θ ($=\eta_p/G$). A good fit of the stress growth curve was obtained with small values of c, see Figure 86, i.e. a constant relaxation time τ (=30.2 s). However such a solution cannot be satisfactory because it does not provide the delayed response which is observed in flow test on increasing the stress. The relaxation time must depend on the microstructure to induce some thixotropy : the formula proposed by P. Coussot was modified, introducing a power law in the expression of τ :

$$\tau = \exp\left[\frac{b}{1+c\,\Gamma\,\left(\xi-\xi_1\right)^m}\right]$$

This is not merely a mathematical trick. It describes more accurately how the characteristic time changes when the state of the material approaches equilibrium. The low value of m (0.1), which was found adequate, traduces the rapid increase of τ when approaching equilibrium. In Figure 87 are reproduced the simulations obtained for different creep duration and comparison is made with the experimental results. The agreement is satisfactory.

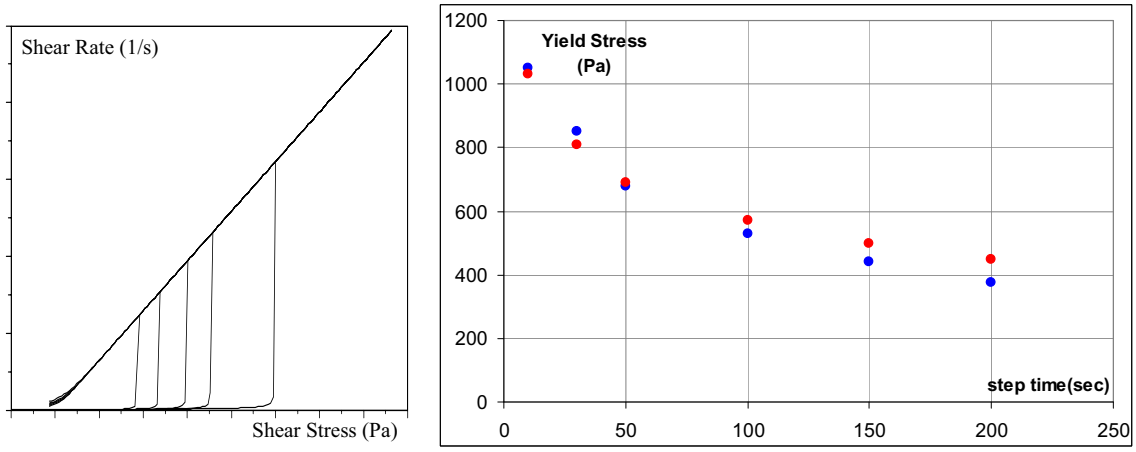

Figure 87. Comparison of the predictions of the model with the experimental data.
Left : hysteresis loops for different step durations , (see experimental data in Figure 55.
Right : yield stress versus step duration, (Blue) experiment, (Red) results of simulation.

Using the approximate formula, eq.(3), with n equals one, the evolution of ξ as a function of stress can be determined *independently of the kinetic equation* :

$$\xi = \frac{\eta_p}{\sigma / \dot{\gamma} + \eta_p - \eta_m} \qquad (5)$$

They are depicted in Figure 88 and compared to the predictions of the simulations *which involve the kinetic equation.*

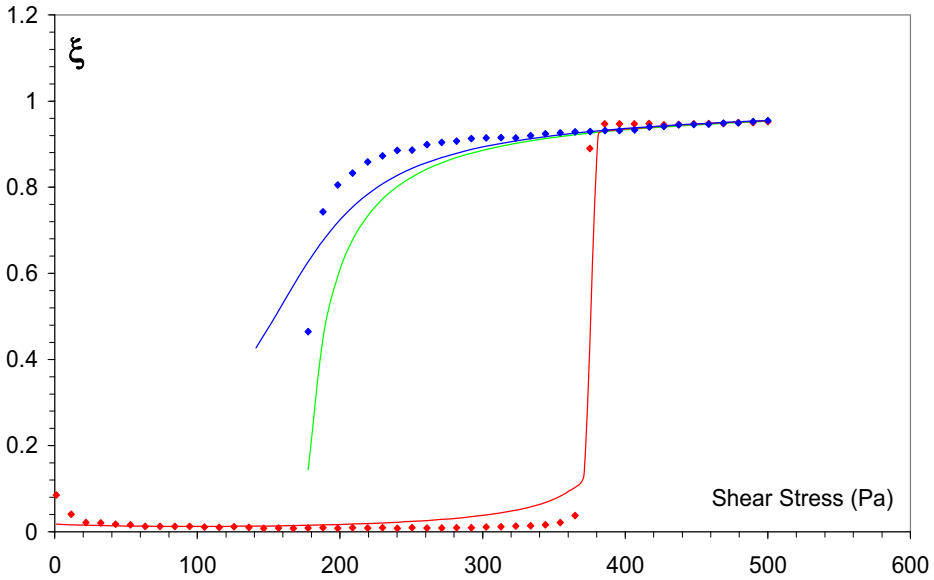

Figure 88. ξ as a function of shear stress.
Increasing stress :(Red). Dots, calculated according to equ.(5). Line, results of simulation.
Decreasing stress (Blue) Dots, calculated according to equ.(5). Line, results of simulation.
Equilibrium values calculated according to equ.(4). (Green line)

It is noted that while the simulations predict an increasing deviation from equilibrium on the return part of the hysteresis curve, the experimental data show on the contrary a "catastrophic" evolution towards equilibrium. Clearly, equation (2) is not the last answer to thixotropy.

Bibliography.

[1] - TA Instruments Rheology Manuals, "Instrument & Accessory Manuals".

[2] – J.F. Steffe, "Rheological methods in food process engineering", Freeman Press, USA, (1996).

[3] – H.A. Barnes, "A handbook of elementary rheology", University of Wales, Institute of Non-Newtonian Fluid Mechanics, Aberyth, (2000).

[4] - Bird, R. B., Armstrong, B. C., and Hassager, O., "Dynamics of polymeric liquids": Volume 1 Fluid Mechanics, John Wiley & Sons, New York, (1987).

[5] - http://www.abe.msstate.edu/classes/abe3813/viscoelasticity/Single.html

[6] - J.D. Ferry, "Viscoelastic Properties of Polymers", Willey, New York (1970).

[7] - D. M. Parks, "Elements of polymer structure and viscoelasticity", Mechanics and Materials II, MIT Open Courses, p.1-15 (2004).

[8] – G. Schramm, "A practical approach to rheology and Rhometry", Gebrueder HAAKE GmbH, Karlsruhe (1994).

[9] – T. Mezger, "A little course in rheology" Rheology Workshop, Dordrecht , (2000).

[10] - G. Fleury, G. Schlatter, R. Muller, "Non linear rheology for long chain branching characterization, comparison of two methodologies: Fourier transform rheology and relaxation." Rheol Acta, 44, p.174–187 (2004).

[11] - H. Giesekus "A simple constitutive equation for polymer fluids based on the concept of deformation-dependent tensorial mobility", J. Non-Newtonian Fluid Mech., 11, p.69-109, (1982).

[12] - J.C. Maxwell, Phil. Tran. Roy. Soc 157, 49, (1867).

[13] - E. Ben-Naim, "Maxwell Model of Inelastic Collisions", 88th Statistical Mechanics Conference, Rutgers University, (2002).

[14] - J, Kim, S.H. Kim, T.K. Shin, H.J. Choi, M.S. Jhon, "Miscibility and rheological characteristics of biodegradable diphatic polyester and linear low density polyethylene blends" Eur. Polym. J., 37, p.2131-2139, (2001).

[15] - M. I. Aranguren, E. Mora, J.V. DeGroot, C.W.Macosko, "Effect of reinforcing fillers on the rheology of polymer melts" J. Rheol. 36, p.1165-1182, (1992).

[16] - V.Vignaux-Nassiet, A.Allal and J.P Montfort, "Emulsion models and rheology of filled polymers" Eur. Polym. J. 34, p.309-322, (1998).

[17] - M. Kluppel, "The role of disorder in filler reinforcement of elastomers on various length scales" Adv. Polym. Sci. 164, p.1-86, (2003).

[18] – http://en.wikipedia.org/wiki/classical.mechanics

[19] - P. Doremus, J.M. Piau, "Yield stress fluid. Structural model and transient shear flow behaviour", J. Non Newtonian Fluid Mech. 39, p.835-952, (1991).

[20] - H.M. Princen, A.D. Kiss, "Rheology of foams and highly concentrated emulsions: IV An experimental study of the shear viscosity and yield stress of concentrated emulsions", J. Coll. Interf. Sci. 128, p.176–187, (1989).

[21] - A. Einstein, "Eine neue Bestimmung der Molekuldimensionen," Ann. Phys. 19, p.289–306, (1906); English translation in "Investigation on the Theory of Brownian Motion", Dover, New York, (1956).

[22] – J. S. Reed, "Principles of Ceramic Processing" 2nd edition, John Wiley and Sons, New York, (1995).

[23] - T. Cosgrove, N. Finch, B. Vincent, J. Webster, "The adsorption of random copolymers of vinyl acetate and ethylene on surface-modified silica particles", Colloids Surf., 31, p.33-46, (1988).

[24] - Krieger IM, Dougherty TJ, "A mechanism for non-Newtonian flow in suspensions of rigid spheres". Trans. Soc. Rheol. 3, p. 137-152, (1959).

[25] - M. Kawaguchi, Y. Kimura, T. Tanahasi and others, "Polymer adsorption effects on structures and rheological properties of silica suspensions" Am. Chem. Soc., 11, p.563-567, (1995).

[26] - F. M. Fowkes "Role of acid-base interfacial bonding in adhesion" J. Adhesion Sci. Tech. 1 p.7-27, (1987).

[27] - P.G. Gennes, "Polymers at an interface; A simpled view", Adv. Coll. Interf. Sci. 27, p.189-209, (1987).

[28] - Ph. Cassagneau, "Payne effect and shear elasticity of silica-filled polymers in concentrated solutions and in molten state." Polymer 44, p.2455-2462, (2003).

[29] - L. Chazeau, J.D. Brown, L.C. Yanyo and .S. Sternstein , "Modulus recovery kinetics and other insights into the Payne effect for filled elastomers." Polymer composites 21(2), p.202-222, (2002).

[30] - Ph. Cassagneau, F. Mélis, "Non-linear viscoelastic behaviour and modulus recovery in silica filled polymers", Polymer 44, p.6607-6615, (2003).

[31] - G. Wu, S. Asai, M. Sumita, T. Hattori, R. Higuchi, J. Washiyama, "Estimation of flocculation structure in filled polymer composites by dynamic rheological measurements", Colloid Polym. Sci., 278, p.220-228, (2000).

[32] - A.J. Zhu and S.S. Sternstein "Non-linear viscoelastic behaviour of nanofilled polymers: interfaces, chain statistics and properties recovery kinetics." Compos. Sci. Technol. 63, p.1113-1126, (2003).

[33] - J. Peon, M. Aguilar, J.F Vega et al. , "On the processability of metallocene-catalysed polyethylene: effect of blending with ethylene-vinyl acetate copolymer", Polymer, 44, p.1589-1594, (2003).

[34] - J. Peon, J.F Vega and others "Phase morphology and melt viscoelastic properties in blends of ethylene/vinyl acetate copolymer and metallocene- catalysed linear polymer" Polymer, 44, p.2911-2918, (2003).

[35] - J. Berriot, F. Martin, H. Montes, L. Monnerie, P. Sotta, "Reinforcement of model filled elastomer : characterization of the crosslinking density at the filler-elastomer interface by 1H NMR measurements." Polymer, 44, p.1437-1447, (2003).

[36] – B. Niraula, T. N. Seng, M. Misran "Vesicles in fatty acid salt–fatty acid stabilized o/w emulsion—emulsion structure and rheology" Colloids Surf. A: Physicochem. Eng. Aspects 236, p.7–22, (2004).

[37] - D.E. Knuth "Contin" Addison Wesley Pub. Corp. Reeding Mass. (USA) (1984).

[38] - B. Niraula, T. N. Seng, M. Misran, "Rheology properties of dodecyl-β-d-maltoside stabilised mineral oil-in-water emulsions", Colloids Surf. A: Physicochem. Eng. Aspects 231, p.159–172, (2003).

[39] - J.Mewis, “Thixotrophy – a general review”, J. Non-Newtonian Fluid Mech. 6, p.1-20, (1979).

[40] - H.A. Barnes, “Thixotrophy – a review”, J. Non-Newtonian Fluid Mech. 70, p.1-33, (1997).

[41] - P. Coussot, C. Ancey, Rhéophysique des pâtes et des suspensions. EDP Sciences Pub.France (1999).

[42] - G. Havet, A.I. Isayev, “A thermodynamic approach to the rheology of highly interactive filler-polymer mixtures : part I-Theory”, Rheol. Acta 40, p.570-581, (2001).

[43] - G. Havet, A.I. Isayev, “A thermodynamic approach to the rheology of highly interactive filler-polymer mixtures : part II. Comparision with polystyrene/nanosilica mixtures” Rheol. Acta 42, p.47-55, (2003).

[44] P. Coussot, A.I. Leonov, J.M. Piau ,”Rheology of concentrated dispersed systems in a low molecular weight matrix”, J. Non-Newtonian Fluid Mech. 46, p.179-217, (1993).

[45] - A I Leonov, “Nonequilibrium thermodynamics and rheology of viscoelastic polymer media”. Rheol. Acta, 15, p.85-98, (1976).

[46] - A.I. Leonov, “On the rheology of filled polymers”, J. Rheol. 34(7), p.1039-1068, (1990).

[47] - M. Simhambhatla, A.I. Leonov, “On the rheological modelling of filled polymers with particle-matrix interactions.” Rheol Acta 14, p.329-338, (1995).

Chapter three: Rheological behaviour at high stresses (>500 Pa) using a capillary rheometer.

Tube viscometers are very useful in collecting rheological data. These instruments may be classified into three basic categories: glass capillaries, often called U-tube viscometers, pipe viscometers and high-pressure capillaries [1]. All establish a pressure difference along the capillary to induce flow.

I Rheological background.

I.1 The apparatus.

The apparatus used in this study is a high pressure commercial rheometer, the Rheomat 1000 (Göttfert, Germany), see Figure 89. The capillary is a cylinder of length L_o (L_o=1, 2, 3 mm) and diameter (D_o= 1 mm) made of steel, coated on its inner surface with tungsten carbide in order to minimise abrasion. It is preceded by a cylindrical chamber (diameter D_1=12 mm) which contains the paste to be characterised. Assuming the incompressibility of the paste, the velocity of the paste is multiplied by a factor 144 when flowing from the chamber into the capillary! This occurs trough convergence of the flow streamlines.

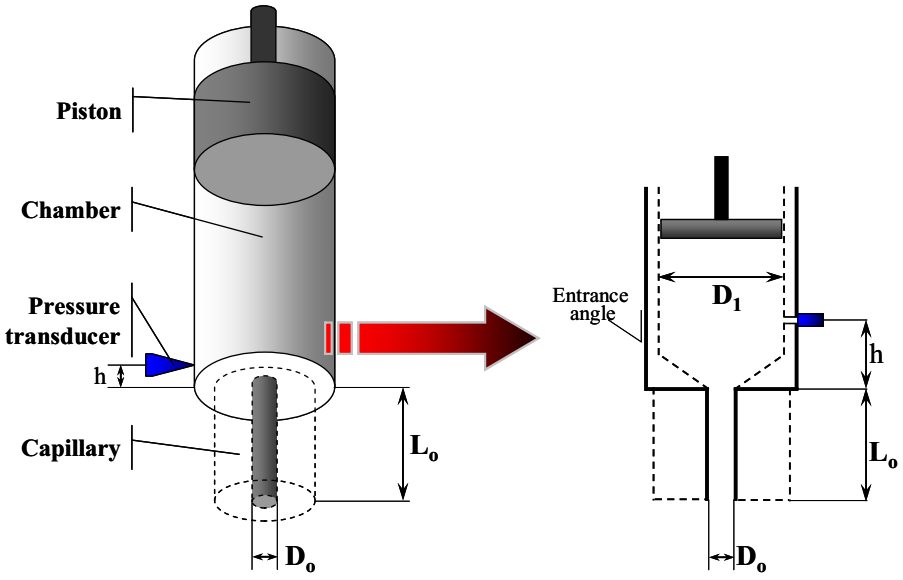

Figure 89. High pressure capillary viscometer.

A flow rate, Q, is fixed by the downward motion of a piston in the chamber at a prescribed velocity, driven by a step motor.

The pressure drop, ΔP, is measured by one pressure transducer, placed in the chamber 16 mm above the capillary entrance, in a region not affected by the convergent flow. The pressure at the exit is the atmospheric pressure (≅1 bar).

I.2 Experimental procedure.

The experimental procedure begins by allowing the apparatus to warm up (usually up to T=130°C) and the required temperature to stabilise. After that, the paste is introduced in the chamber. A resting time of 20 min is necessary to permit the consolidation of the paste. Then, the piston drive is engaged and the paste is extruded through the die. The experiment consists of a set of different piston's speeds, an example of which is given in Table 16. For each velocity, the pressure changes are recorded, see Figure 90.

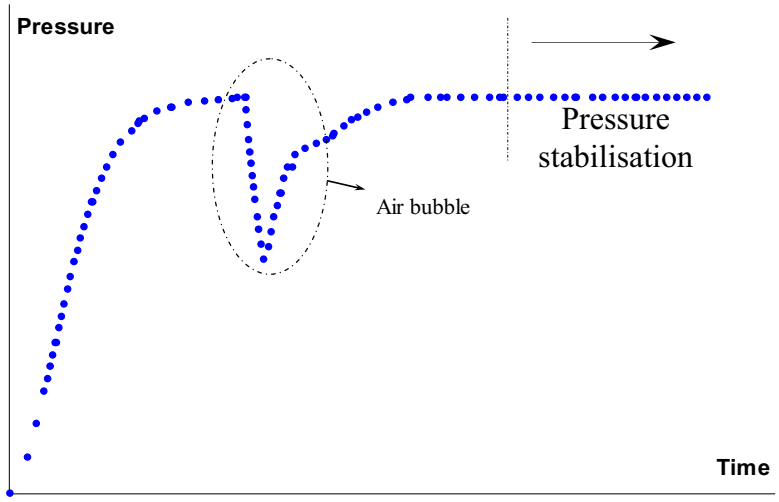

Figure 90. Pressure stabilisation using a manual procedure.

The stationary state is automatically or manually detected. In this work a manual control was preferred to avoid artefacts, such as air bubbles. To cover the broad range of measured pressures, three sensors were necessary P_{50} (0-5 MPa), P_{200} (0-20 MPa) and P_{1000} (0-100 MPa).

Pressure transducer	Piston speed (mm/sec)
P_{50}	0.01-0.4
P_{200}	0.3-0.8
P_{1000}	0.6-2.0

Table 16. Pressure transducers and piston speeds ranges. (Do=1 mm).

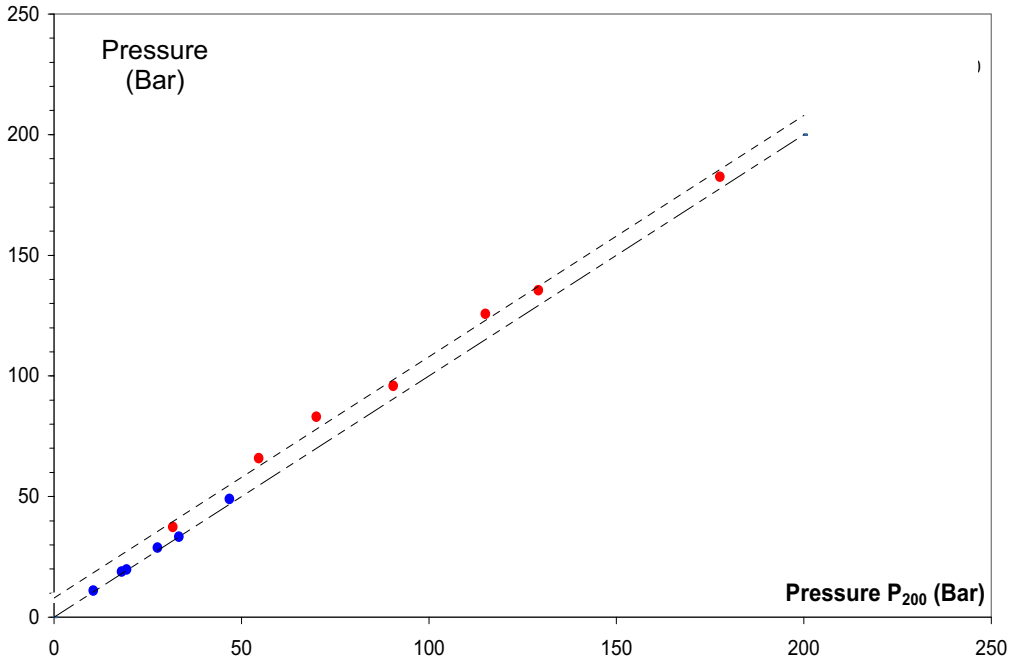

Figure 91. Comparison of pressure values for different transducers: P_{50}, (Blue), P_{1000} (Red) versus P_{200}.

Measurements with sensors P_{50} and P_{200}, in the same conditions of capillary length and flow rate, agree within a few percents. In the case of sensors P_{200} and P_{1000}, a systematic difference of + 1.1 MPa has been evidenced and corrections have been made.

For a given capillary length and pressure gauge, several runs, usually three, were conducted in order to estimate experimental random errors. Altogether, relative uncertainties on stresses are of the order of 5%. For each value of the piston speed, three capillaries with different lengths (L=10, 20, 30 mm) were used. Only pastes with 30, 40, 50, 60% vol. of the powder (Y-ZrO_2 in this chapter), could be studied.

I.3 The ideal capillary.

In the case of highly viscous pastes, the velocity is always so low that the flow is laminar. Moreover, we are interested in the steady, isothermal regime [2]. To simplify, the capillary is supposed to be of infinite length and there is no slip at the walls. In those conditions, the Navier-Stokes equation reduces to a simple force balance [3].

Let us consider a fluid flowing through a horizontal tube of inner diameter D and in the fluid, a small volume, a cylinder of length L and radius r, see Figure 92.

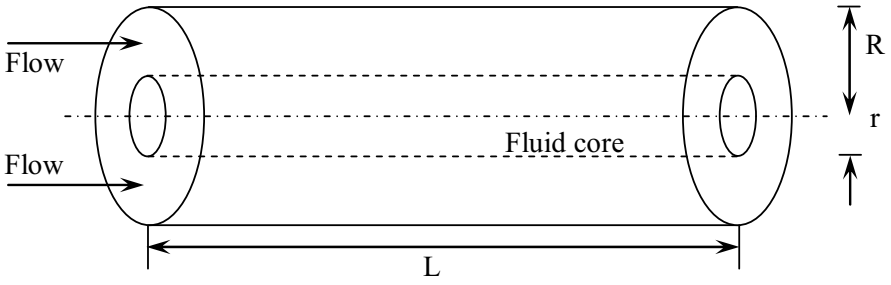

Figure 92. Fluid core of radius r in tube flow geometry.

The forces acting on this volume are the pressure gradient, which promotes the flow, counterbalanced by a surface force, the shear stress σ, induced by the viscous nature of the fluid. It is assumed that the effect of gravity is negligible.

$$\frac{\Delta P}{L}\pi r^2 L = \sigma 2\pi r L \quad \text{or} \quad \sigma = \Delta P \frac{r}{2L}$$

The stress varies linearly with r and is the highest at the wall (r=R):

$$\sigma_W = \frac{\Delta P}{L}\frac{D}{4}$$

Let us emphasize that this relation is independent of the nature of the fluid.

On the opposite, to solve completely the problem, i.e. to determine the velocity field, the nature of the fluid has to be defined. Let us assume a Newtonian behaviour, i.e. the shear stress is proportional to the velocity gradient:

$$\sigma = \eta \frac{dv}{dr}$$

σ being a function of r, this is a first order differential equation in v(r) which can be solved with the boundary condition, v(R)=0:

$$v = \frac{D^2}{16\eta}\frac{\Delta P}{L}\left[1 - \left(\frac{2r}{D}\right)^2\right]$$

and the flow rate is given by :

$$Q = 2\pi \int_0^{D/2} v(r)dr = \frac{\pi R^4}{8\eta}\frac{\Delta P}{L}$$

called the Poiseuille-Hagen equation [4]. It can be seen that the radius has a very strong influence on the behaviour of the system since it is raised to the fourth power. The shear rate at the wall is equal to:

$$\dot{\gamma}_w = \frac{4Q}{\pi R^3}$$

In the general case of a non-Newtonian fluid, it can be shown that :

$$\dot{\gamma}_w = \left(\frac{dv_z}{dr}\right)_w = \frac{4Q}{\pi R^3}\left(\frac{3}{4} + \frac{1}{4}\frac{d\ln\left(\frac{4Q}{\pi R^3}\right)}{d\ln\sigma_w}\right)$$

The factor $\frac{4Q}{\pi R^3}$ is called the apparent shear rate, $\dot{\gamma}_{app}$. Knowing the relationship $\dot{\gamma}_{app}(\sigma_w)$, it is then possible to calculate the true relation $\dot{\gamma}_w(\sigma_w)$; this procedure is called the Rabinowitch correction [5]. This equation can be rewritten in the following simplified form :

$$\dot{\gamma}_w = \dot{\gamma}_{app}\left(\frac{3n+1}{4n}\right)$$

where $n = \frac{d\ln\sigma_w}{d\ln\dot{\gamma}_{app}}$ is the local slope of the ln(σ_w) versus ln($\dot{\gamma}_{app}$) graph. In many cases, n is more or less constant, what is called a power law.

As already emphasized, the velocity profile depends on the specific relationship between stress and strain rate. A parabolic velocity profile is associated with a Newtonian behaviour. This is no longer the case if it is non-Newtonian, in particular in the case of a power law [6, 7]. After integration and use of the no slip boundary condition:

$$v(r) = \left(\frac{\Delta P}{2L\,K}\right)^{\frac{1}{n}}\left(\frac{n}{n+1}\right)\left[R^{\frac{n+1}{n}} - r^{\frac{n+1}{n}}\right]$$

The relationship between the velocity at r and the volumetric average velocity

$$\langle v\rangle = \frac{Q}{\pi R^2}$$

can be calculated :

$$\frac{v}{\langle v\rangle} = \left(\frac{3n+1}{n+1}\right)\left[1 - \left(\frac{r}{R}\right)^{\frac{n+1}{n}}\right]$$

A low value of the index n result in a flat velocity profile, see Figure 93.

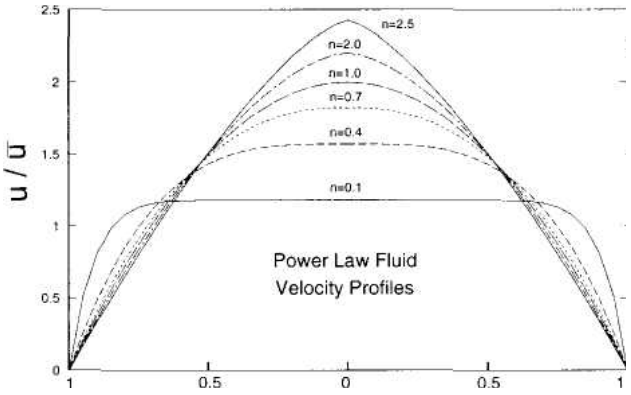

Figure 93. Velocity profiles in the laminar regime for power law fluids with different values of the index n.

I.4 Corrections.

I.4.1 End Effects.

In Figure 94 are reported the experimental data obtained for two capillary lengths, plotted as apparent shear rates versus wall shear stress. Two different curves are obtained, which are not straight lines: the paste behaves as a non-Newtonian fluid. That the pressure drop at the entrance of the capillary cannot be neglected is also clearly evidenced.

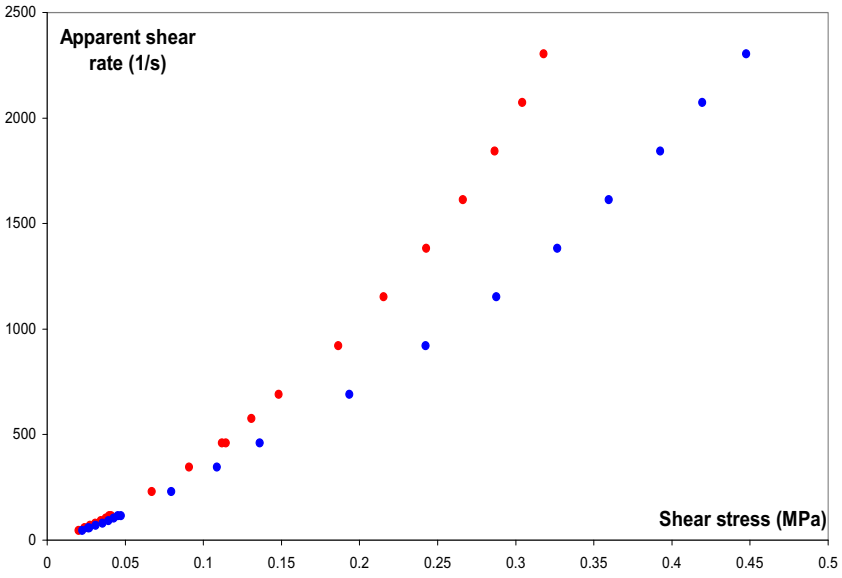

Figure 94. Apparent shear rate vs. shear stress for two capillaries lengths, L=10 mm (Blue), L=20 mm. (Red). Solid fraction 60%vol. Y-ZrO_2 paste.

Energy losses due to fluid divergence at the end of a capillary are small and usually neglected but entrance losses can be very significant and have to be evaluated [8, 9]. They

result from the sudden change in geometry and the convergence of the stream lines. As already mentioned, the pressure transducer is placed above this perturbed region and measures both contributions, the one of the entrance, that of the pressure gradient in the capillary.

The latter depends on the length of the capillary while the former does not:

$$\Delta P_{meas} = 4\sigma_W \frac{L}{D} + \Delta P_{Bagley}$$

where ΔP_{meas} is the measured pressure drop, and ΔP_{Bagley} is the entrance pressure loss. This is the basis of what is called the Bagley's correction [10]. An example is given in Figure 95 where the measured pressure drops are plotted versus L. A linear relationship is indeed observed in agreement with expectation, permitting the determination of the Bagley correction, ΔP_{bagley} and of the pressure gradient in the capillary, A (= 4 σ_w/D), and finally of the maximum stress at the wall for each value of the flow rate.

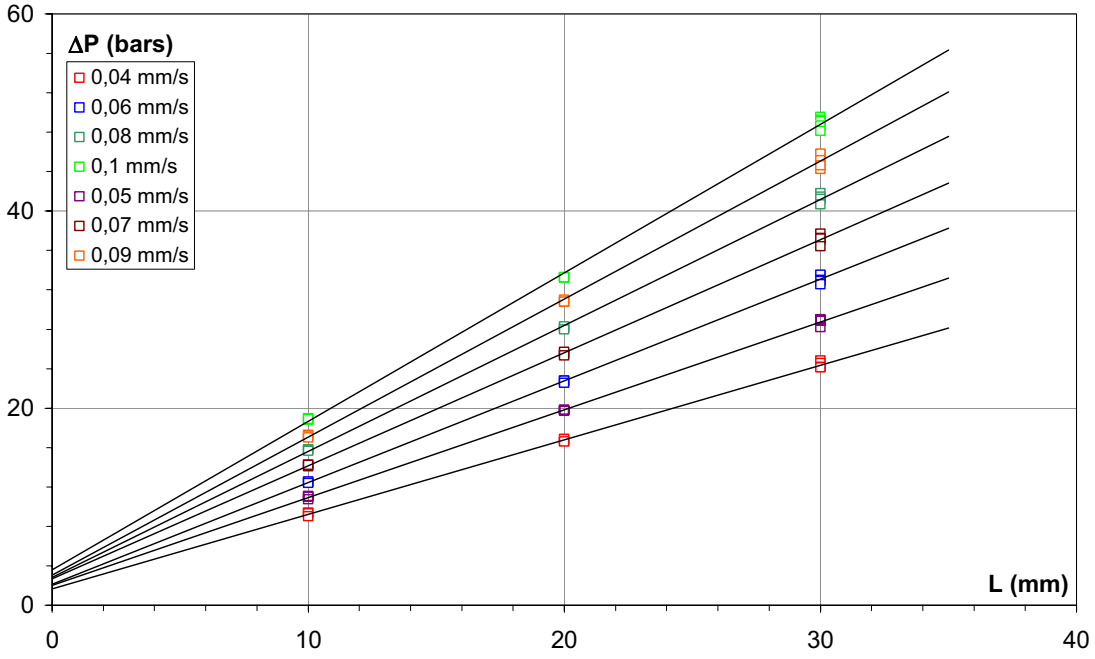

Figure 95. Plots of pressure drop vs. capillary length, for different piston velocities. 60% vol. solid fraction – Y-ZrO_2 paste.

I.4.2 Wall Effects.

The no-slip boundary condition is not always verified [11, 12, and 13]. Slip occurs when a thin layer of fluid, having a viscosity lower than that of the fluid, forms at the wall.

This problem was addressed by Mooney [14, 15] and others [16, 17]. The consequence is to modify the expression of $\dot{\gamma}_{app}$:

$$\dot{\gamma}_{apps} = \frac{32Q}{\pi D^3} - \frac{8V_s}{D} \quad \text{or} \quad \frac{32Q}{\pi D^3} = \dot{\gamma}_{apps} + \frac{8V_s}{D}$$

Experiments are performed with capillaries of different diameters and the same L/D ratio at constant shear stress. The results are reported as a function of 1/D. The slope of the curve is equal to $8V_s$. To verify this phenomena some tests with different capillaries were made.

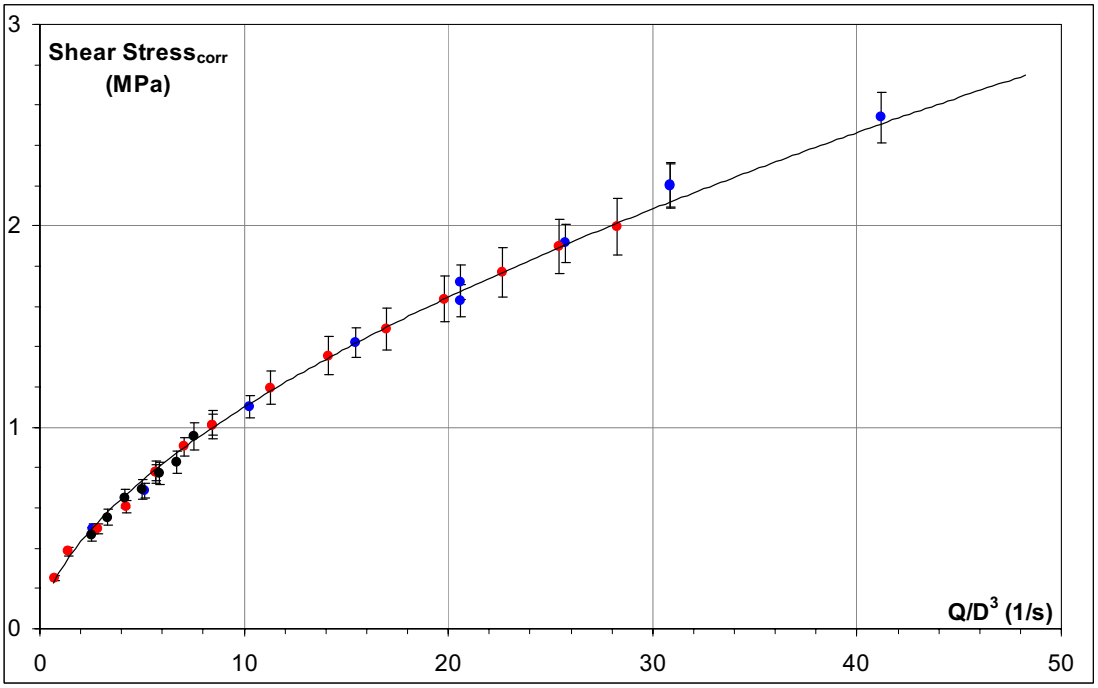

Figure 96. Comparison between results obtained with different capillary diameters D_o=1.3 mm (Blue), D_o=2 mm (Red) D_o=3 mm (Black) – all values of shear stress are determined following the Bagley's procedure (L_1 = 10 mm and L_2 = 30 mm).

As is shown in Figure 96, the values obtained for six capillaries define a unique curve which means that no slip exists at the wall.

II Experimental results.

II.1 The shear properties.

In Figure 97, the shear stress is plotted versus the apparent shear rate. In order to calculate the true shear rate, the slope of the curve $\dot{\gamma}_{app}(\tau_w)$ has to be evaluated. Fortunately, a very good fit can be obtained with a polynomial of low order and the derivative is calculated analytically.

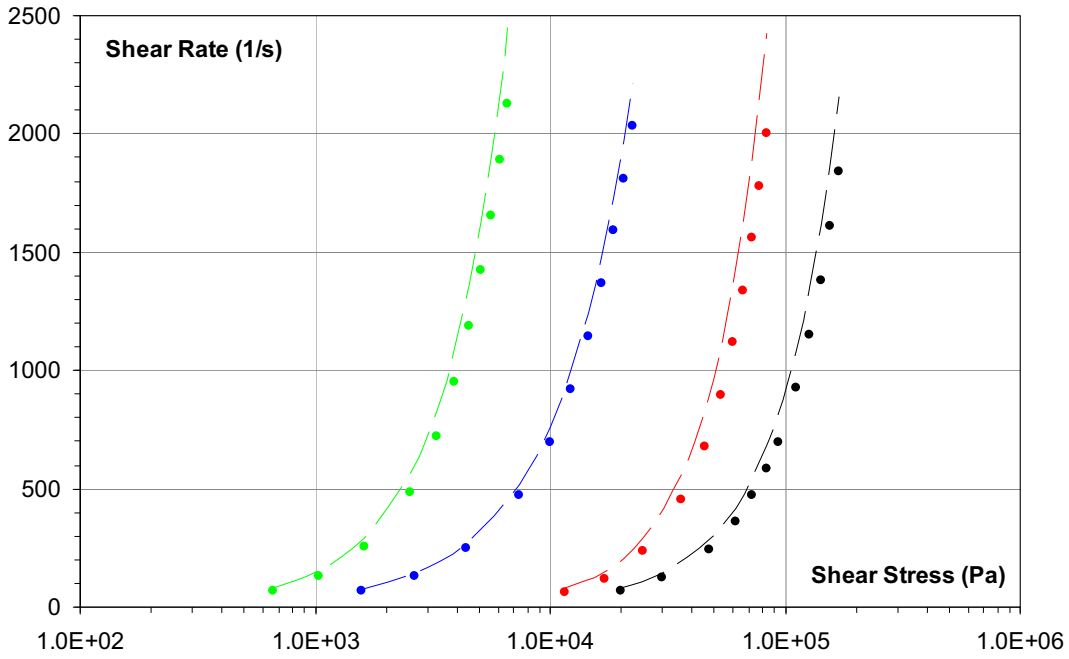

Figure 97. Shear stress vs shear rate for different solid fractions 30%vol. (Green), 40%vol. (Blue), 50%vol. (Red), 60%vol.(Black). Y-ZrO_2 paste. Solid line – after Rabinowitch correction [5].

As far as the shear rate is concerned, the correction is important only in the high stress range i.e. above 10^5 Pa for the 60% vol. solid fraction paste.

Figure 98 summarizes the results obtained with the two kinds of rheometers for the 30%vol solid fraction paste.

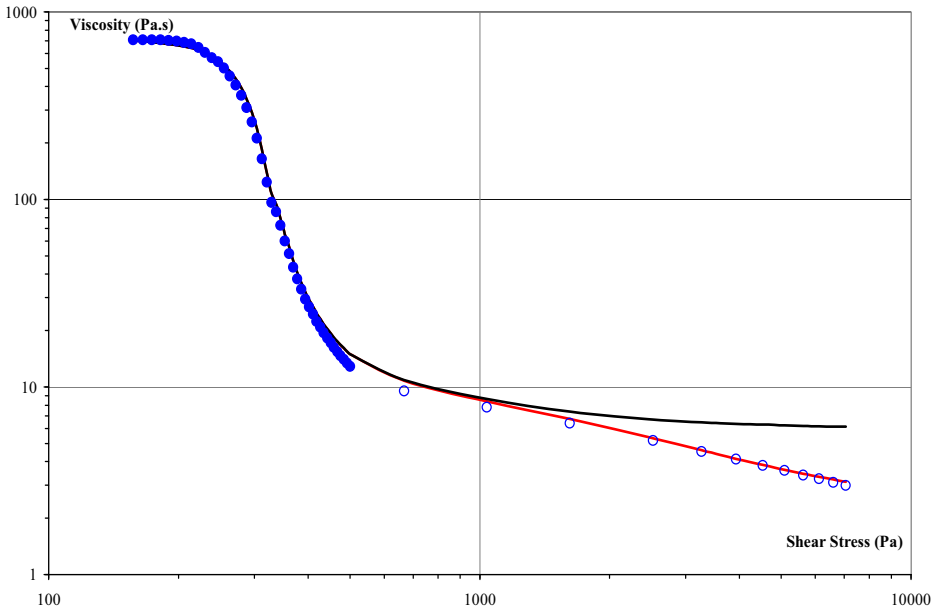

Figure 98. Flow curve in a log-log plot for the 30%vol solid fraction paste, combining results obtained with both types of rheometers: rotational (full dots), capillary (open dots) Fits: Black line, one Carreau term [18], Red line, two terms, see text.

There is a remarkable agreement between the two sets of data, which incidentally is another proof of the no slip condition.

A single Carreau's [18] term was not sufficient to fit the complete set of data and therefore two terms were included:

$$\eta = \eta_\infty + \frac{\Delta_1}{\left(1 + K_1\ \dot{\gamma}^2\right)^{m1/2}} + \frac{\Delta_2}{\left(1 + K_2\ \dot{\gamma}^2\right)^{m2/2}}$$

The first term was already used in the previous fit, see Figure 66. The values of the parameters are given in Table 17.

Parameter	Value
η_∞ (Pa.s)	2
Δ_1 (Pa.s)	780
Δ_2 (Pa.s)	4
K_1 (s^2)	5
K_2 (s^2)	1.0e-5
m_1	1
m_2	0.7

Table 17. Values of parameters used to fit the data of Figure 98.

$(\eta_\infty+\Delta_1)/\eta_m$ corresponds to a value of k=1.6 using the Krieger-Dougherty relation [19] as already mentioned and can be interpreted as corresponding to aggregates. Then, the second term describes the fragmentation of aggregates into individual particles (η_∞/η_m is equal to 3.3 and k=1.09). Thus, for this paste, we were able to characterize the different steps of fragmentation from the agglomerates to the isolated grains.

In Figure 99, the results obtained for the "homogeneous" pastes with 40, 50, 60%vol. solid fractions, are presented.

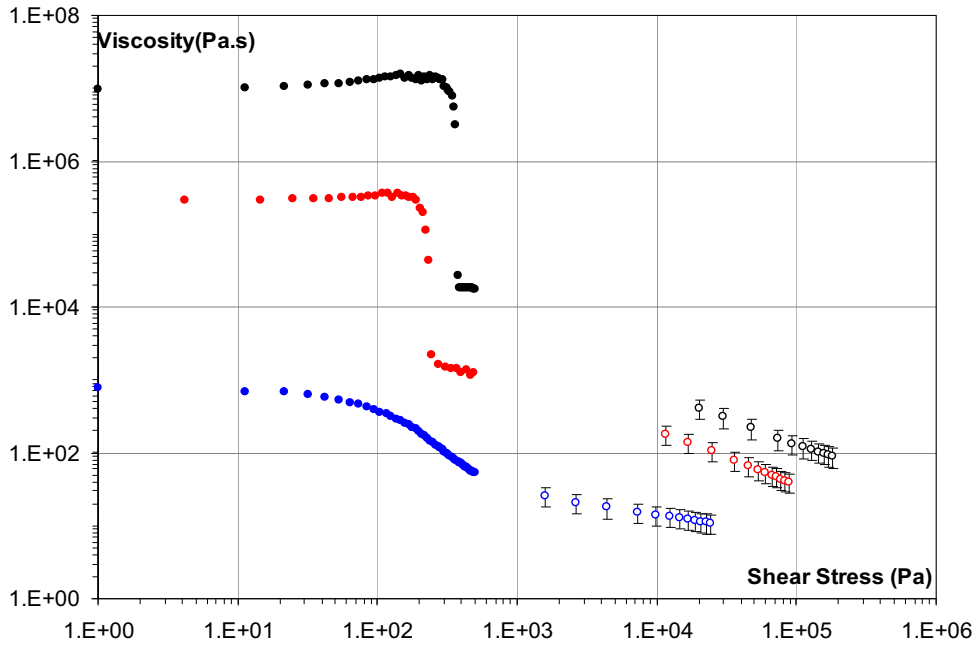

Figure 99. Flow curve in a log-log plot for the 40%vol (Blue), 50%vol. (Red), 60%vol. (Black) solid fraction Y-ZrO_2 paste, combining results obtained with both types of rheometers : rotational (full dots), capillary (open dots).

Once again, a good agreement between the two sets of data is observed. For the 40%vol. solid fraction paste, the fragmentation of the aggregates also takes place, but at a higher value of the applied stress. In the case of the 50 and 60%vol. solid fraction pastes, complete fragmentation occurs only for values of stress, which are unattainable (>10^6-10^7 Pa.s). The consequence is a power law behaviour, which is verified over three orders of magnitude! Clearly, increasing the solid fraction makes the grains closer, strengthens the binding between grains.

II.2 Extensional properties.

The Bagley's pressure drops are plotted versus flow rate (Q) in Figure 100.

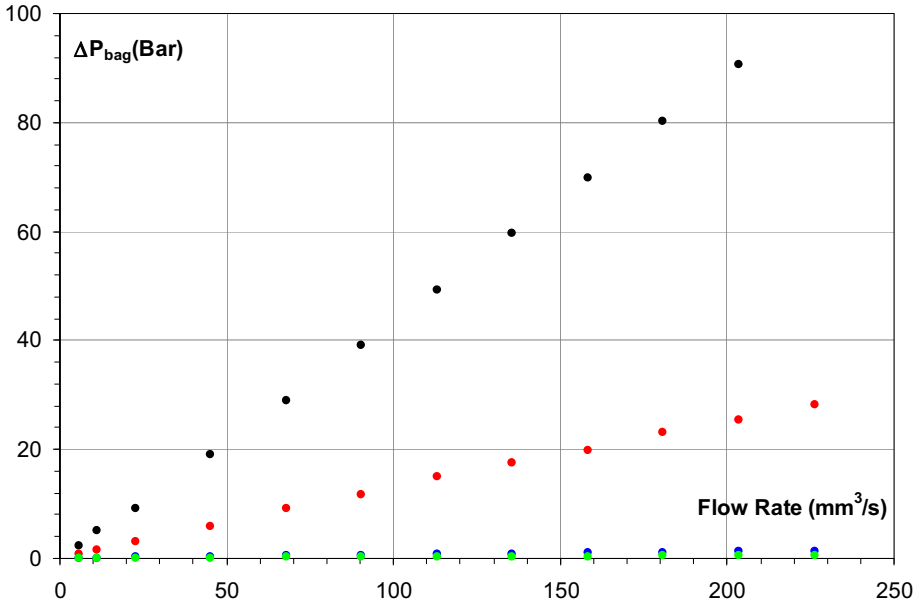

Figure 100. The Bagley's pressure drop versus the flow rate for different solid fractions : 30%vol. (Green), 40%.vol. (Blue), 50%vol. (Red), 60% vol. (Black). Y-ZrO$_2$ paste.

They appear to be simply proportional to Q. This reminds the Darcy's law, which would imply some accumulation of the powder at the entrance of the capillary and some kind of filter press effect [20]. To test this hypothesis, the weight of the extrudate was monitored during the experiment performed at constant speed, see Figure 101, and as shown, it varies linearly with time.

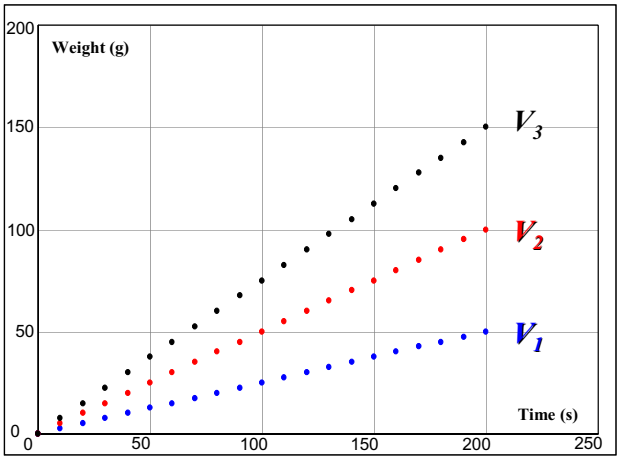

Position of the piston.	Density (kg/m^3)
Beginning	3970 ± 5%
Half-way	3950 ± 6%
End	3960 ± 5%

Table 18. Density at different positions along the extrudate.

Figure 101. Extrudate weight (arbitrary scale) as a function of time. 60% vol. solid fraction paste.

The density of the extrudate, calculated from the slope, is equal within uncertainty to that of the prepared paste. Let us emphasize that the test is very sensitive because of the high density of zirconia (6050 kg/m^3) compared to that of the organic matrix (≅1000 kg/m^3). It is concluded that no segregation occurs and that the paste can be considered as homogeneous. This is confirmed by SEM observations, see Figure 102.

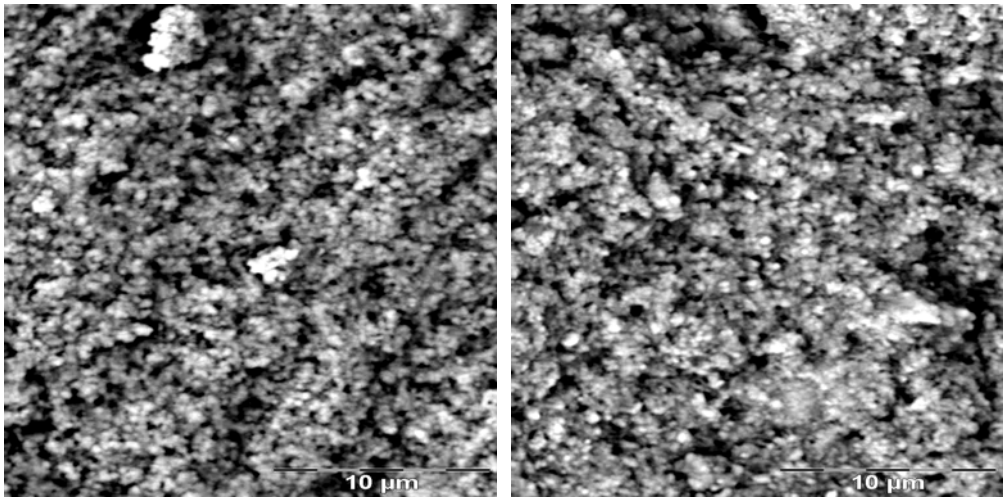

Figure 102. SEM observations of extrudate. Left - vertical cut, Right - horizontal cut.

At the entrance of the capillary, the velocity of the paste is increased by two orders of magnitude in order to accommodate the change in radius and to keep the flow rate constant! In the case of a Newtonian behaviour, the viscosity is the only parameter and simulation of the flow can be performed, see Figure 103, which clearly shows the convergence of the velocity lines [21].

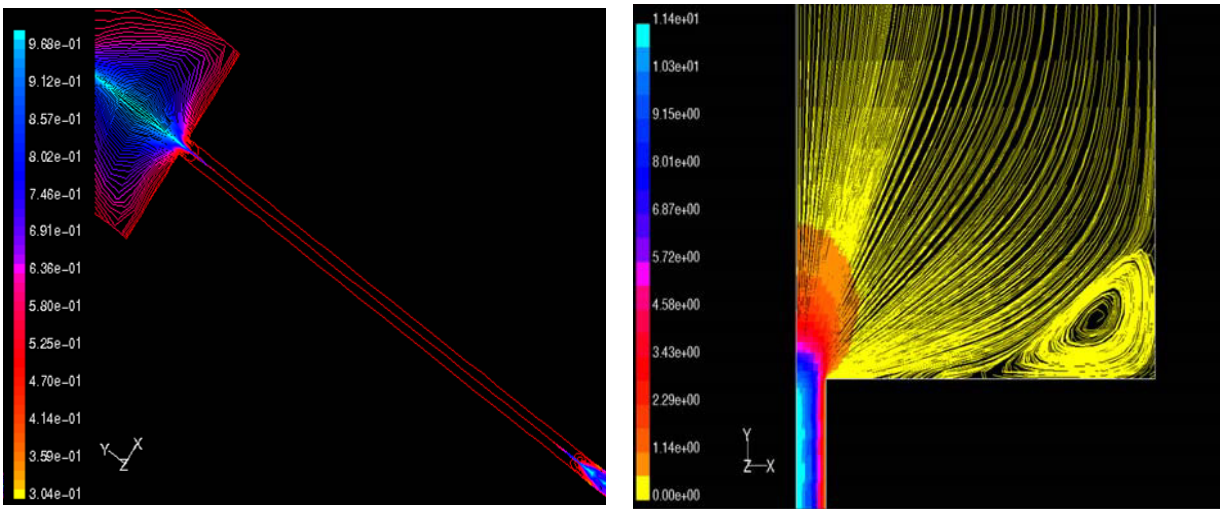

Figure 103. Mathematical modelling using the Polyflow software.
Left. Contours: Green - pure extension, Blue - pure shear. Right: velocity field

Along the axis, the deformation is no longer a simple shear but is a pure extension.

Trouton [22] has defined the extensional viscosity as:

$$\eta_E = \frac{(\sigma_{11} - \sigma_{22})}{\dot{\varepsilon}}$$

where σ_{11} and σ_{22} are the normal components of the stress tensor and $\dot{\varepsilon}$ the extensional rate. The ratio of η_E to η is called the Trouton ratio and is equal to 3 in the case of a Newtonian behaviour. In the case of a viscoelastic material, the two viscosities are independent parameters and the Trouton ratio can be very different from 3. The direct determination of the extensional viscosity is experimentally difficult because a pure extensional regime implies an exponentially increasing deformation with time. Developing a well-defined extensional flow, necessary for the measurement of the extensional viscosity, is not an easy task. Some techniques can produce the kinematics required for pure elongation but are unable to reproduce the extreme conditions found in typical processing applications. Therefore, besides specific set-up devoted to such measurements, indirect methods have been used to, at least, estimate the extensional viscosity, among them fibre spinning experiments and converging flow experiments [23]. The latter is performed in a capillary rheometer, which therefore permits the study of both the shear and extensional properties using a single apparatus [24, 25 and 26]. This is the choice we have made in this study.

Cogswell [27, 28] was the first to propose an analytical analysis of the flow in a conical die taking into account both shear and extensional contributions. The extensional stress and strain rate are given by the following formulas:

$$\sigma_E = \frac{3}{8}(n+1)\Delta P_{Bagley} \qquad \dot{\varepsilon} = \frac{4\eta_{app}\dot{\gamma}_{app}^{\ 2}}{3(n+1)\Delta P_{Bagley}}$$

and

$$\eta_E = \frac{9(n+1)^2(\Delta P_{bagley})^2}{32\eta_{app}\dot{\gamma}_{app}^{\ 2}}$$

where the apparent shear viscosity is assumed to obey a power law dependence: $\eta_{app} \propto \dot{\gamma}_{app}^{n-1}$. For the studied paste, this is verified in the conditions of the capillary rheometer.

Let us emphasise that the extensional viscosity is calculated for each value of the flow rate (or equivalently the shear rate).

Experimentally, the Bagley's pressure drop is proportional to the flow rate or equivalently to the apparent shear stress and therefore:

$$\eta_E(\dot{\varepsilon})\,\eta_{app}(\dot{\gamma}) \approx \text{const.}$$

i.e. the extensional viscosity increases with the extensional strain rate ! Taking into account the power law behaviour of η_{app}, the extensional viscosity obeys a power law:

$$\eta_E \approx \dot{\varepsilon}^{\frac{1}{n}-1}$$

In Figure 104 are depicted the variations of the extensional viscosity against the strain rate calculated using the Cogswell's analysis.

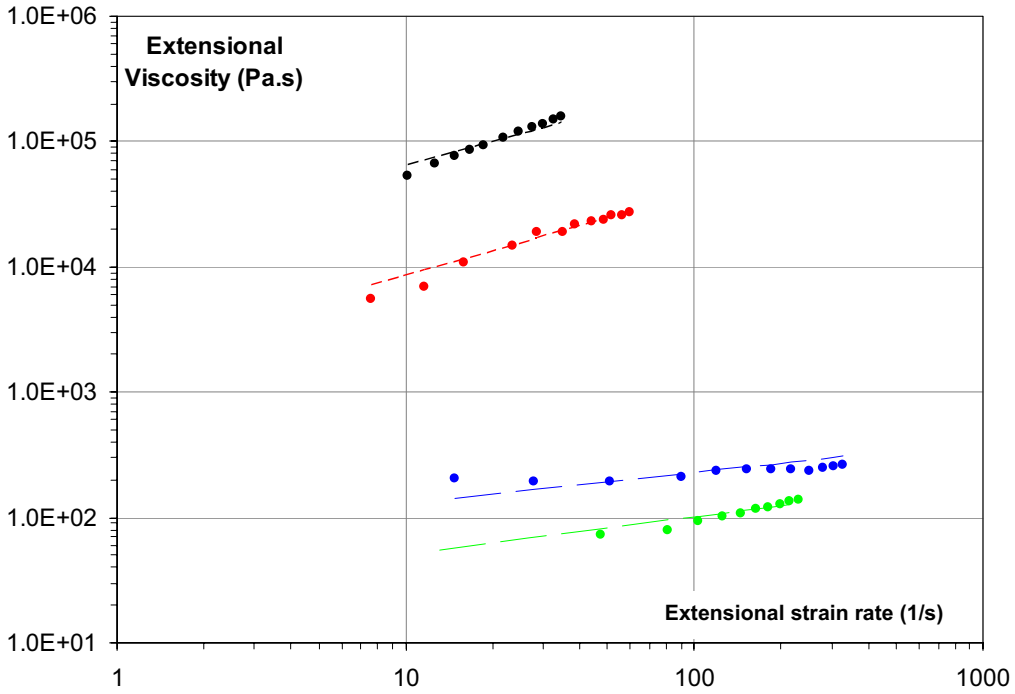

Figure 104. The extensional viscosity (η_E) versus the extensional strain rate calculated according to, Cogswell's analysis (dots) and Binding's analysis (lines) for different solid fractions :30%vol. (Green), 40%vol. (Blue), 50%vol. (Red), 60% vol. (Black). Y-ZrO_2 paste.

The Cogswell analysis suffers from several approximations which are not coherent with each other and which have been criticized. A more elaborate model has been proposed by Binding [29, 30, 31].

The strain rate tensor is a priori postulated with both a shear $(\dot{\gamma})$ and extensional $(\dot{\varepsilon})$ components.

$$T_{ij}=\begin{bmatrix}-P & 0 & 0\\ 0 & -P+T_{yy} & T_{yz}\\ 0 & T_{yz} & -P+T_{zz}\end{bmatrix} \quad D_{ij}=\begin{bmatrix}0 & 0 & 0\\ 0 & -\dot{\varepsilon} & \dot{\gamma}/2\\ 0 & \dot{\gamma}/2 & \dot{\varepsilon}\end{bmatrix}$$

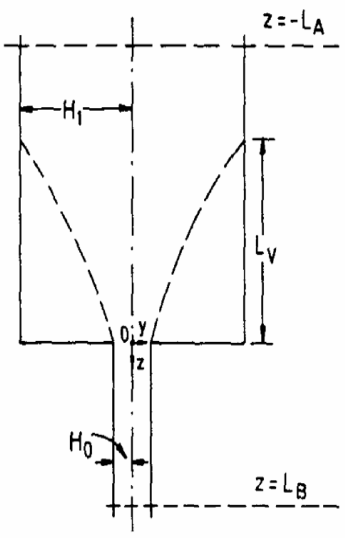

It is further assumed that both obey a power law with different exponent, resp. n and t:

$$\eta = k\left|\dot{\gamma}\right|^{n-1} \qquad \text{and} \qquad \eta_E = l\left|\dot{\varepsilon}\right|^{t-1}$$

Vortices are supposed to be present in the corners of the reservoir in agreement with Figure 103.

The boundary between the main flow and these vortices is fixed by the constraint of a least power consumption. Then the strain rate and stress tensors can be calculated at every point and the entry pressure drop can be evaluated. It depends in a complicated manner on the parameters of the model:

$$\Delta P_{entrance} \cong \frac{2k(1+t)^2}{3t^2(1+n)^2}\left\{\frac{lt(2n+1)n^t I_{nt}}{k}\right\}^{1/1+t}\dot{\gamma}^{t(n+1)/t+1}\left\{1-\alpha^{3t(n+1)/1+t}\right\}+\frac{3\rho(3n+1)^2Q^2(1-\alpha^4)}{2\pi R_0^4(2n+1)(4n+3)}$$

where α is the inverse of the contraction ratio,

$$\alpha = R_0/R_1 \text{ and } I_{nt}=\int_0^1\left|2-\frac{3n+1}{n}x^{1+\frac{1}{n}}\right|^{t+1}x.dx$$

but fortunately, the last term in the sum is, in our case, negligible. Let us recall that the apparent shear rate is related to flow rate Q. Then, the observed linear relationship of ΔP_{Bagley} versus Q, implies

$$t.n \cong 1 \qquad \text{and } \eta_E \approx \dot{\varepsilon}^{\frac{1}{n}-1}$$

a result already obtained in the Cogswell's analysis. The prefactors are also similar. Therefore, almost identical results are obtained with both approaches, see Figure 104.

As a consequence of the fact that t is larger than n, the vortex size increases with increasing flow rate. Since extensional and shear viscosities are functions of strain rates of different nature, a conventional method of comparison is needed to remove ambiguity.

Jones [32] suggests that the shear viscosity should be evaluated at a shear rate of $\dot{\varepsilon}\sqrt{3}$:

$$N_{Tr} = \frac{\eta_E(\dot{\varepsilon})}{\eta(\sqrt{3}\,\dot{\gamma})}$$

and this has been done in Figure 105.

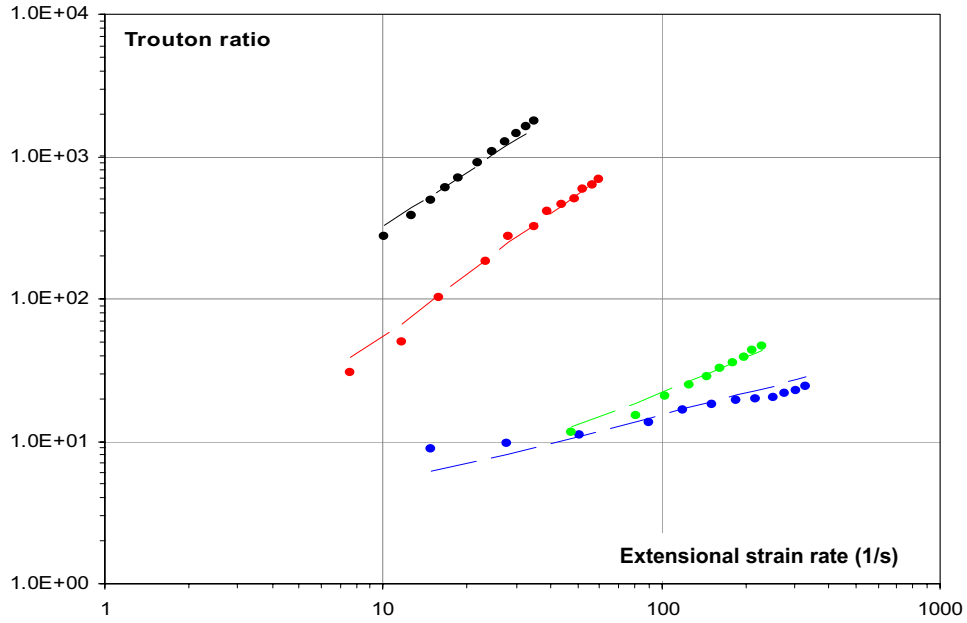

Figure 105. The Trouton ratio η_E/η depicted versus the extensional rate for different solid fractions : 30%vol. (Green), 40%vol. (Blue), 50%vol. (Red), 60% vol. (Black). Extensional viscosity calculated according to Cogswell's (points) and Binding's (lines) analysis. Y-ZrO_2 paste.

The value of the Trouton ratio is very far from 3 with strong implications in processing.

It is to be noticed that a high extensional viscosity is associated with the existence of a yield stress (50, 60%vol. solid fraction pastes). This is also for these compositions that fragmentation into individual grains is so difficult, i.e. the binding forces between the grains are very high.

Bibliography.

[1] – J.F Aggassant, P. Avenas, J.Ph. Sergent. “La mise en forme des matières plastiques. Technique et Documentation” – Lavoisier, Paris, (1986).

[2] – A. Weill. “Rhéologie des Polymères Fondus”, Techniques de l’Ingénieur, Vol. A3615, p.1-20.

[3] – V. Gupta, S.K Gupta, “Fluid mechanics and its applications”, Wiley Eastern Ltd., New Delhi, (1984).

[4] - J. Kestin, M. Sokolov, W. Wakeham, “Theory of capillary viscometers”, Appl. Sci. Res. 27, p.241-264, (1973).

[5] – B. Rabinowitsch, “Über die Viskosität und Elastizität von Solen” Z. Physik. Chemie A 145, p.1-26, (1929).

[6] – R. Darby, “Chemical engineering fluid mechanics”, Marcel Dekker, New York, (1996).

[7] – W. Philippoff, F.H Gaskins, “The capillary experiment in rheology”, Trans. Soc. Rheol., II, p.263-284, (1958).

[8] – S. Tantayanon, S. Juikham “Enhanced toughening of poly(propylene) with reclaimed-tire rubber”. J. Appl. Polym. Sci., 91, p.510 – 515, (2003)

[9] – N. Sombatsompop, R. Dangtungee “Flow visualization and extrudate swell of natural rubber in a capillary rheometer: Effect of die/barrel system.” J. Appl. Polym. Sci., 82, p.2525 – 2533, (2001).

[10] - E. B. Bagley “End corrections in the capillary flow of polyethylene”, J. Appl. Phys., 18, p.624-627, (1957).

[11] - W. Gleisle, E. Windhab, “The "twin capillary" a simple device to separate shear- and slip-flow of fluids”, Exp. Fluid 3, p.177-180, (1985).

[12] – U. Yilmazer, D. M. Kalyon, “Slip effects in capillary and parallel disk. Torsional flows of highly filled suspensions”, J. Rheol., 33(8), p.1197-1212, (1898).

[13] – Ph. Mourniac, J.F. Agassant, B. Vergne, “Determination of wall slip velocity in the flow of SBR compound” Rheol. Acta, 31, p.565-574, (1992)

[14] - N. Mooney, “Explicate formulas for slip and fluidity”. J. Rheol. 2 , p.210-222, (1931).

[15] - N. Mooney, S.A Black, “A generalized fluidity power-law and laws of extrusion”, J. Colloid Sci., 7, p.204-217, (1952)

[16] – K. Geiger. “Rheologische charakterisierung von EPDM kautchukmischungen mittels capillar-rheometer system”. Kautschuk + Gulli Kunstoffe, 42, p.273-283, (1989).

[17] – S. Wiegreffe. “Untersuchungen zum wandgleitverhalten vom EPDM und SBR”. Kautschuk + Gummi Kunstoffe, 44, p.216-221, (1991).

[18] - Bird, R. B., Armstrong, B. C., and Hassager, O., “Dynamics of polymeric liquids”: Volume 1 Fluid Mechanics, John Wiley & Sons, New York, (1987).

[19] – Krieger IM, Dougherty TJ, “A mechanism for non-Newtonian flow in suspensions of rigid spheres”. Trans. Soc. Rheol. 3, p.137-152, (1959).

[20] – H. Darcy, “Les fontaines publiques de la Ville de Dijion, au filtrage des eaux”, Victor Dalmont, Paris (1856)

[21] - D.V. Boger, “Viscoelastic flows through contractions”, Ann. Rev. Fluid Mech., 19, p.157-182, (1987).

[22] – F.T Trouton, "On the coefficient of viscous traction and its relation to that of viscosity" Proc. Roy. Soc. A77, p.426-440, (1906).

[23] - J. Greener and J.R.G. Evans, “Measurements of elongational flows in ceramic processing”, J. Eur. Ceram. Soc., 17, p.1179-1183, (1997).

[24] - A. D. Gotsis, A. Odriozola “The relevance of entry flow measurements for the estimation of extensional viscosity of polymer melts”, Rheol. Acta, 37, p.430-437, (1998).

[25] - E. Mitsoulis, S. G. Hatzikiriakios, K. Christodoulou, D. Vlassopoulos “Sensitivity analysis of the Bagley correction to shear and extensional rheology”, Rheol. Acta, 37, p.438-448, (1998).

[26] - T. Glomsaker, E. L. Hinrichen “Numerical simulation of extrusion of S-PVC formulations in a capillary rheometer”, Rheol. Acta, 39, p.80-96, (2000).

[27] - F. N. Cogswell “Converging flow of polymer melts in extrusion dies”, Polym. Eng. Sci., 12, p.64-73, (1972).

[28] – F.N. Cogswell, “Measuring the extensional rheology of polymer melts” Trans. Soc. Rheol., 16:3, p.383-403, (1972).

[29] - D. M. Binding "An approximate analysis for contraction and converging flows", J. Non-Newtonian Fluid Mechanics, 27, p.173-189, (1988).

[30] – M.A Couch, D.M. Binding, "High pressure capillary rheometry of polymeric fluids" Polymer 41, p.6323-6334, (2000).

[31] - D. M. Binding, M. A. Couch and K. Walters, "The pressure dependence of the shear and elongational properties of polymer melts". J. Non-Newtonian Fluid Mech., 79, p.137-155, (1998).

[32] - D. M. Jones, K. Walters, P. R. Williams, "On the extensional viscosity of mobile polymer solution" Rheol. Acta, 26, p.20-30, (1987).

Chapter four: Influence of the powder material.

The rheological properties of pastes prepared with different powders were investigated. Three materials were selected : alumina, silicon carbide and zirconia, which are commonly used in ceramic applications on one hand and are of a different chemical nature on the other hand.

I General review.

We have seen that Einstein's prediction [1] in the case of low volume fractions of solid is a simple, very informative, tool. The experimental results are presented in Figure 106.

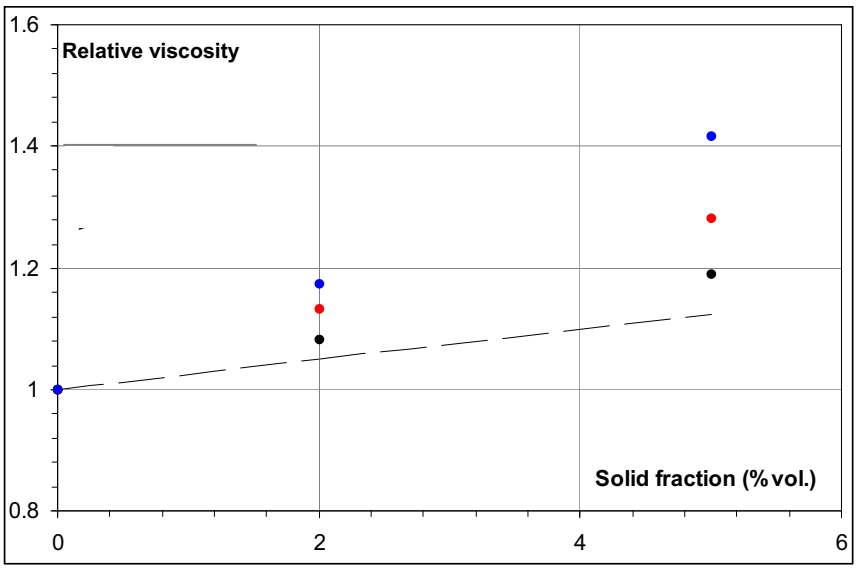

Figure 106. Relative viscosity vs. the volume fraction of solid for the three materials : Y-ZrO_2 (Blue), Al_2O_3 (Red), SiC (Black), - - - - - Einstein prediction.

The values of k, calculated on using an extension of Einstein's prediction, are reported in Table 19.

Powder material	**k**
SiC	1.5
Al_2O_3	2.1
Y-ZrO_2	3.0

Table 19. Values of k derived from the data of Figure 106.

They show a different behaviour of the three powders, i.e. a different interaction of the organic matrix with the grains depending on the material. Assuming that EVA and Carnauba wax are the polymers adsorbed on the surface of the grains, it is concluded that the ratio EVA/Carnauba decreases in the sequence Y-ZrO_2, Al_2O_3, SiC.

The three pastes behave very similarly, i.e. a second viscosity jump exists for the 20%vol. and 30%vol. fraction of solid which disappears for 40%, see Figure 107

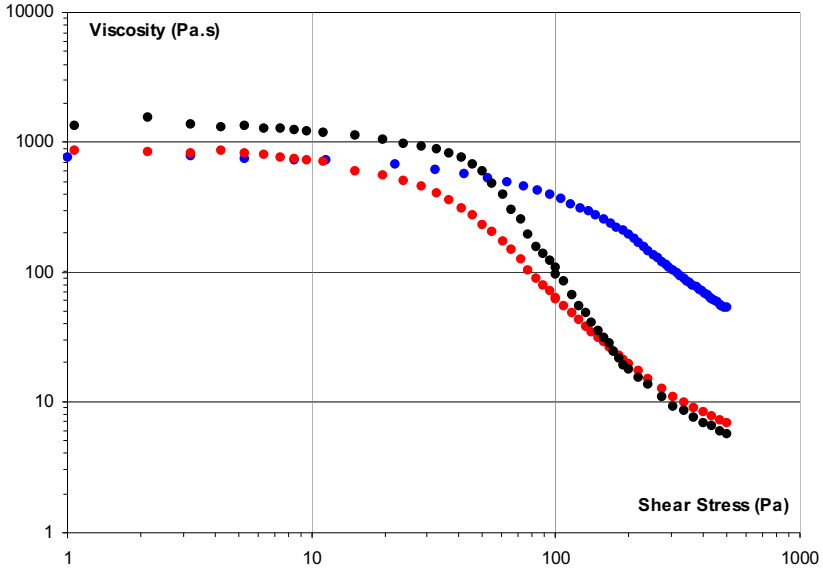

Figure 107.Flow curves – log-log scale. Viscosity vs shear stress for the three powders : Y-ZrO_2 (Blue), Al_2O_3 (Red), SiC (Black). 40 % vol. solid fraction.

SEM observations confirm that this is related to the homogeneity of the paste, the former being inhomogeneous, the latter homogeneous, see Figure 108.

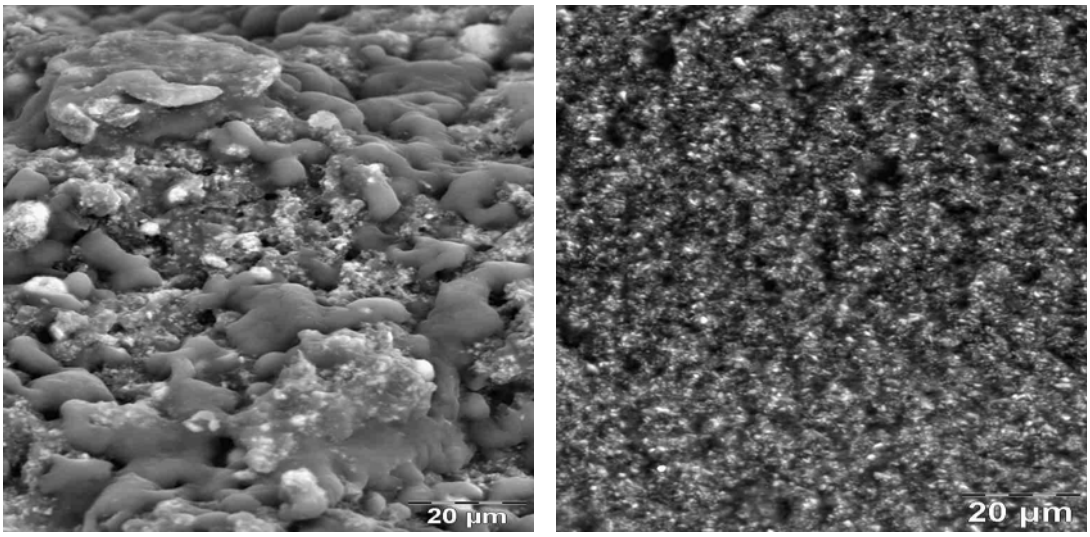

Figure 108. SEM observations of alumina loaded pastes : LEFT 20%vol. RIGHT 40%vol. solid fraction.

II The inhomogeneous pastes.

In Figure 109 are depicted the flow curves obtained for 5%vol. fraction of solid and different materials.

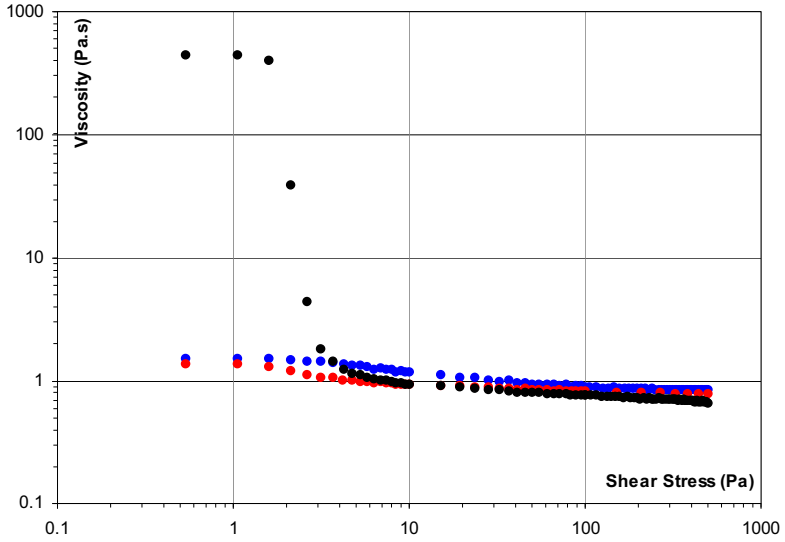

Figure 109. Flow curves – log-log scale. Viscosity vs shear stress for the three powders : Y-ZrO_2 (Blue), Al_2O_3 (Red), SiC (Black). 5 % vol. solid fraction.

Clearly, silicon carbide loaded paste shows a different behaviour. This difference still exists for a 10%vol. fraction of solid, although not so pronounced, and is not very apparent for higher solid fractions, see Figure 109. This will be discussed later on.

As in chapter two, the high stress viscosity can be used to determine the effective volume fraction $k\phi$. When the volume fraction of solid, ϕ, is low, the determination of η_∞ and then of k, is easy. In the case of the 30%vol. fraction of solid, a fit of the data is necessary and this has been done with Carreau's equation [2]. Contrary to zirconia, one term did not permit a good fit of the flow curves in the case of alumina and silicon carbide and an additional term was included, a procedure already used in chapter three. This has been attributed to the fragmentation of primary aggregates into individual grains. In the case of alumina and silicon carbide, this second contribution is centred around 200 Pa and can be observed with the rotational rheometer while in the case of the zirconia based paste, much higher stresses are needed, attainable only with the capillary rheometer. The data are collected in Table 20, and the volume fraction of trapped liquid $(k-1)\phi$, is plotted in Figure 111 versus the volume solid fraction, ϕ.

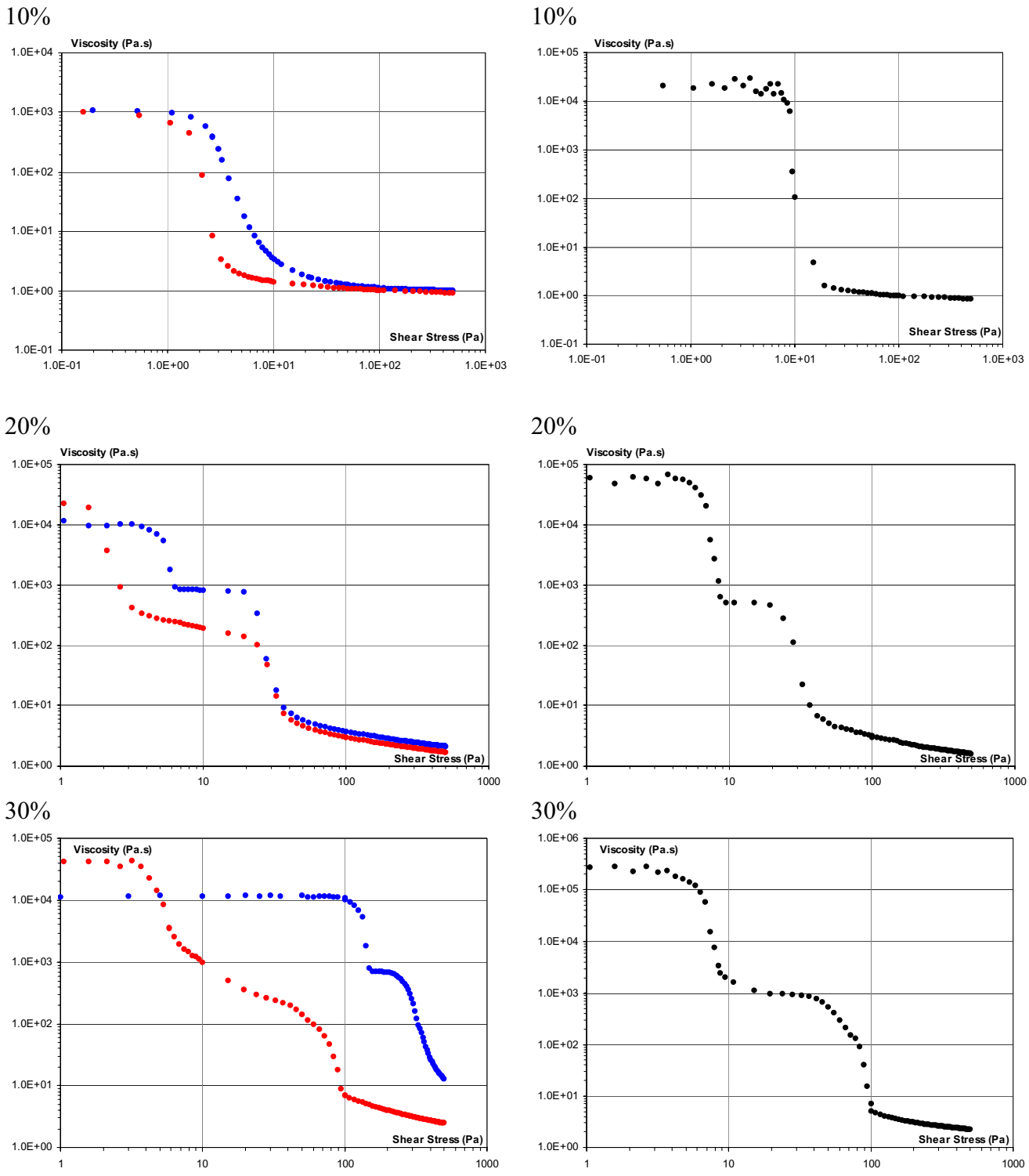

Figure 110. Flow curves – log-log scale.: LEFT) Y-ZrO_2 (Blue), Al_2O_3 (Red). RIGHT) SiC (Black)

From top to bottom: 10% vol., 20% vol., 30% vol. solid fractions.

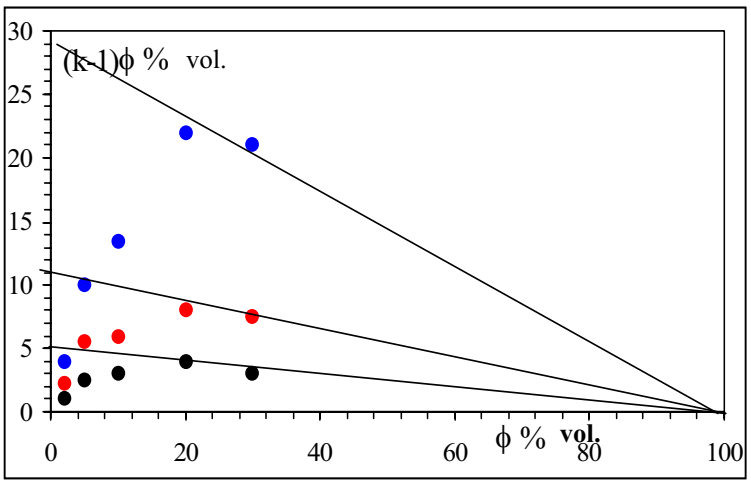

ϕ(%)	**Y-ZrO_2**	**Al_2O_3**	**SiC**
2	3	2.1	1.5
5	2.5	1.9	1.4
10	2.35	1.75	1.3
20	2.1	1.4	1.2
30	1.7	1.25	1.1

Table 20. Values of k determined through the application of the Krieger-Dougherty equation.

Figure 111. Trapped liquid (k-1)ϕ (%) as a function of the volume fraction of solid for the three materials : Y-ZrO_2 (Blue), Al_2O_3 (Red), SiC (Black)

Once again, saturation is observed for 20 and 30%vol. solid fractions, which permits the determination of ϕ_L, 11% and 5% for resp. alumina and silicon carbide. These values are lower than the amount of EVA + Car and therefore it is not possible to determine the ratio of EVA/Car of adsorbed species on the grain surfaces from the knowledge of the values of ϕ_L. However, let us recall that a value of k=1.1 was obtained for the zirconia powder immersed in pure liquid carnauba wax and this suggests that EVA is not adsorbed on the surface of silicon carbide grains and little on those of alumina.

One can be surprised that a change in the flow curve with two plateaus of viscosity always occurs for a volume solid fraction of 20%, independently of the material (Y-ZrO_2, Al_2O_3, SiC) and of the blend composition (EVA20Car10, EVA10Car20). This is the consequence of a simple geometric criteria : depending on the compactness (50-65%), the powder occupies fully the liquid inclusions (30%vol.) for a volume solid fraction between 10 and 20%. This is not contradictory with the discussion of the previous paragraph. The apparent volume, kϕ, is that of aggregates obtained by disruption of the inclusions and 1/k is the compactness of the aggregates and not of the agglomerates inside the inclusions. A low value of k (k<1.5, 1/k>66%), is indicative of small aggregates. This was already the case for the EVA10Car20 composition. In the case of agglomerates, the trapped liquid is only partly adsorbed on the grains surfaces.

Once the interactions between inclusions have been suppressed (the intermediate plateau of viscosity), the viscosity is very similar for the three materials (around 1000 Pa.s). This a further indication of a common structure of the paste, a given volume (30%) of fully filled inclusions, determined by the EVA + Car. content only.

For volume fractions of solid lower than 20%, the low stress viscosity is fixed by the deformability of the inclusions under stress. In the absence of solid particles, they appear to deform easily and the behaviour is Newtonian. The presence of solid particles makes them less akin to deformation, a pronounced effect in the case of silicon carbide. The fact that the difference in behaviour decreases when the volume solid fraction increases strongly suggests that the topology of the agglomerates inside the inclusion is a key factor. Somehow, silicon carbide seem closer to the behaviour of carbon black loaded elastomers [3, 4]. This may be related to the fact that they are non oxides and have a low affinity with polymer molecules. Other (colloidal?) forces are probably operative.

III The paste suitable for injection.

When the blend composition is EVA20Car10**,** the prepared paste is homogeneous for volume fractions of powder of 40% and higher, independently of the nature of the material. On the opposite, in the case of a zirconia based paste with the same volume fraction of solid of 40%, it has been seen in chapter two that the paste is inhomogeneous for a blend composition EVA10Car20. This suggests that the key factor is the presence (in the latter case) or the absence (in the former case) of free carnauba wax in the liquid phase. Indeed, the DSC study in chapter one has shown that carnauba wax and paraffin are immiscible and in chapter two that carnauba wax acts as a dispersant. This may explain why the inclusions remain stable in the presence of free carnauba wax. On the other hand EVA and paraffin, although immiscible have shown some affinity which may favour homogeneity of the paste when the EVA content is low enough.

In the following, the properties of pastes prepared with a volume fraction of solid of 60%, which are suitable for injection moulding, will be further investigated.

III.1 Influence of the material.

The flow curves are presented in Figure 112.

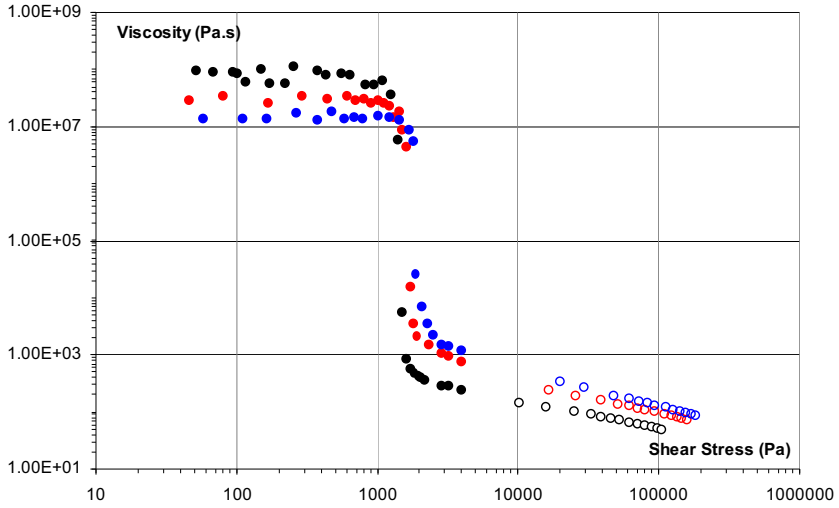

Figure 112. Flow curves – log-log scale. Viscosity vs shear stress for the three materials : Y-ZrO_2 (Blue), Al_2O_3 (Red), SiC (Black). 60 % vol. solid fraction. Combining results obtained with both types of rheometers : rotational(step duration – 30 sec) (full dots), capillary (open dots)..

The data obtained with the two kinds of rheometers, rotational and capillary ones, are reported in Figure 112 and there is a good agreement between the two sets of data. Although small differences exist, they behave quite similarly.

Using the capillary rheometer and from the determination of Bagley's [5] pressure drop, see Figure 113, the extensional viscosity was estimated as in chapter three.

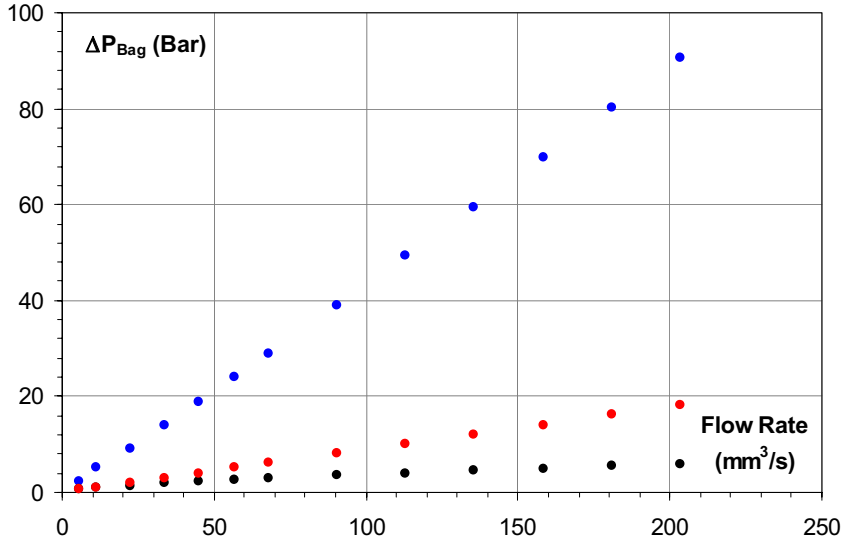

Figure 113. The Bagley's pressure drop versus the flow rate. Three materials : Y-ZrO_2 (Blue), Al_2O_3 (Red), SiC (Black) Solid fraction – 60% vol.

The results are presented in Figure 114.

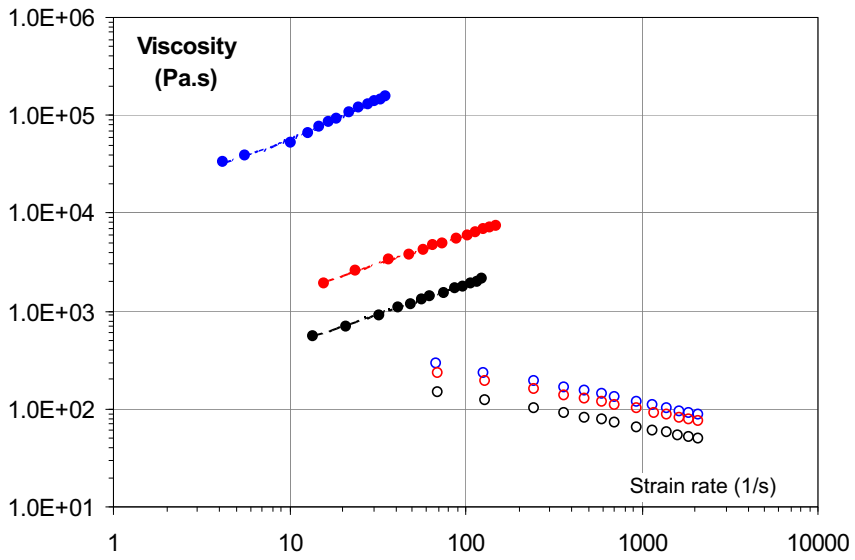

Figure114. The extensional viscosity (full dots) and shear viscosity (open dots) depicted versus the strain rate using two different approaches, Cogswell's [6] (dots) and Binding's [7] analysis (lines). Three materials : Y-ZrO_2 (Blue), Al_2O_3 (Red), SiC (Black).

On the same figure are reported the shear viscosity data. Shear properties appear to be very similar. In the reported range of stress, a power law can be used to fit the data with the same index (0.65). On the opposite, the extensional viscosities are very different. In Figure 115, the Trouton ratio [8] is depicted as a function of strain rate.

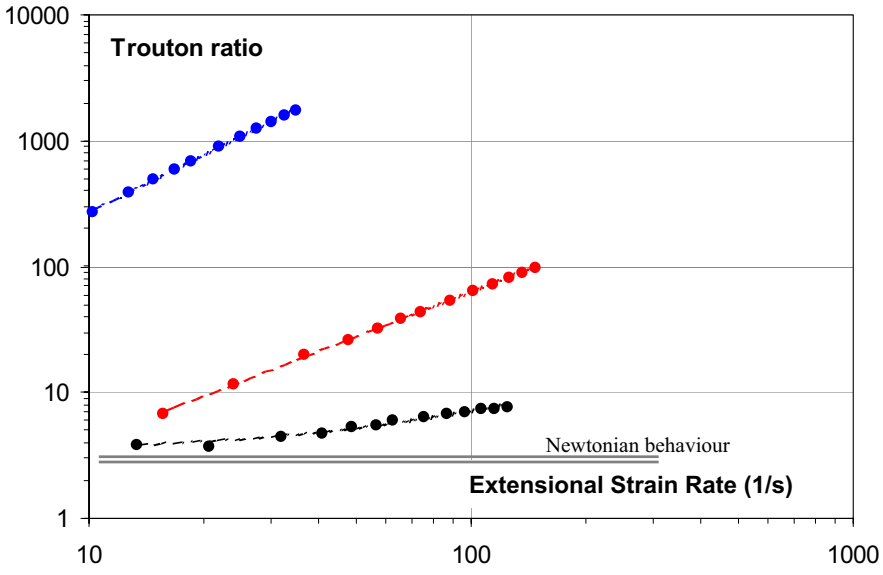

Figure 115. The Trouton ration η_E/η depicted versus the strain rate. Three materials : Y-ZrO_2 (Blue), Al_2O_3 (Red), SiC (Black).Solid fraction 60% vol.

The differences are even more striking, Let us recall that the Trouton ratio is equal to 3 in the case of a Newtonian behaviour. This is almost the case of silicon carbide loaded paste !. It is concluded that the extensional properties are mainly fixed by the EVA adsorption.

III.2 Influence of temperature.

The capillary rheometer was used to investigate the properties of the three pastes at three temperatures, 125, 130 and 135°C.

III.2.1 Shear properties.

The shear viscosity data are depicted in Figure 116.

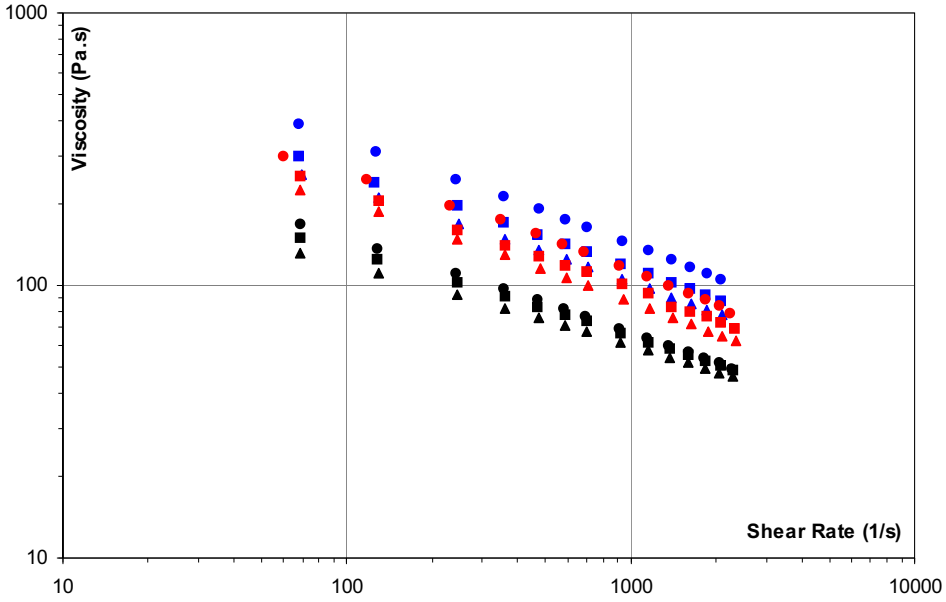

Figure 116. Viscosity versus shear rate.
Three materials : Y-ZrO_2 (Blue), Al_2O_3 (Red), SiC (Black).
Three temperatures: circle – 125°C, square – 130°C, triangle – 135°C.

In a log-log plot, although a slight curvature can be seen, a power law is used to fit the data. The index varies very little with temperature, 0.65±0.05. Variations with temperature are also not strong – for silicon carbide paste almost insignificant (+/- <10% of viscosity value).

III.2.2 Extensional properties.

The Bagley's pressure drops data are depicted in Figure 117. In the case of silicon carbide, they are so low that uncertainties are quite important.

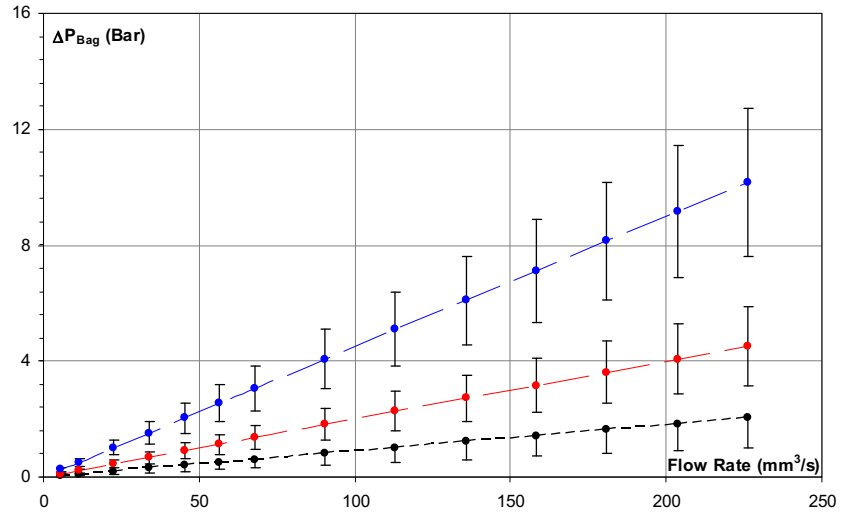

SiC

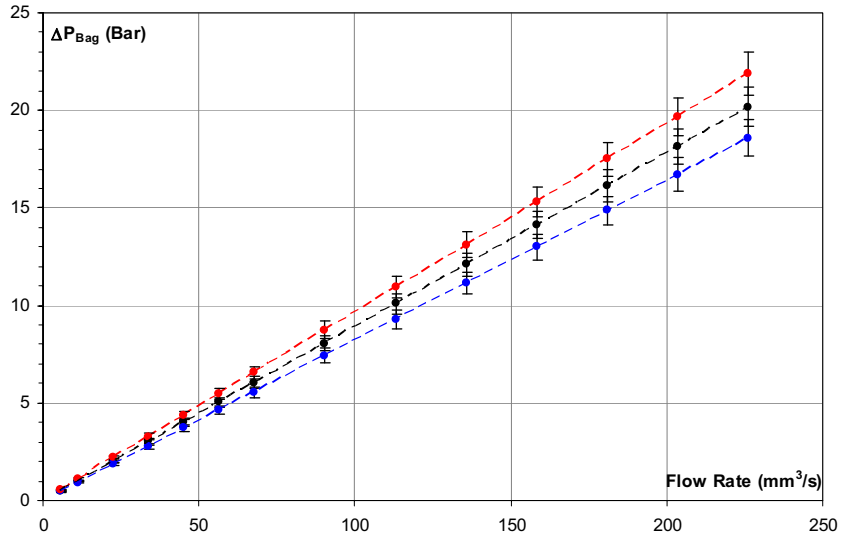

Al_2O_3

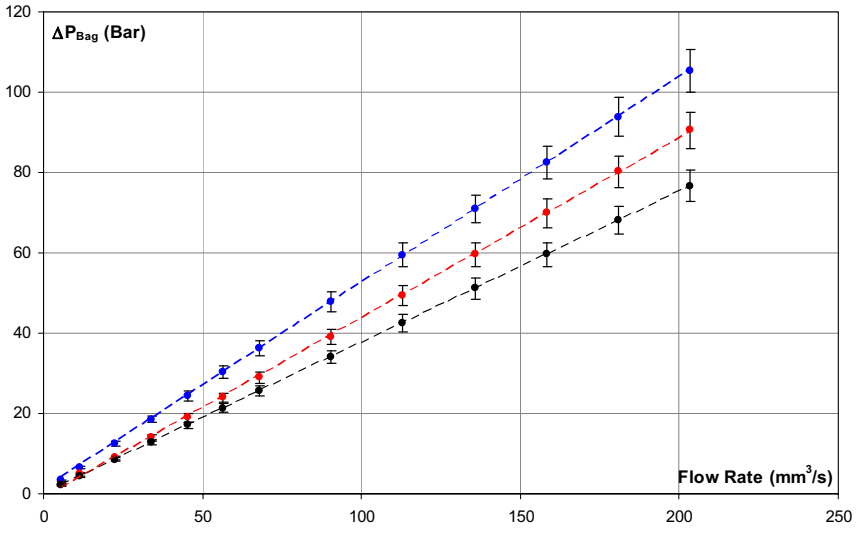

Y-ZrO_2

Figure 117. The Bagley's pressure drop versus the flow rate for different temperatures 125°C (Blue), 130°C (Red), 135°C. (Black) and different materials.

In Figure 118, the variations of the Trouton ratio are depicted versus extensional rate.

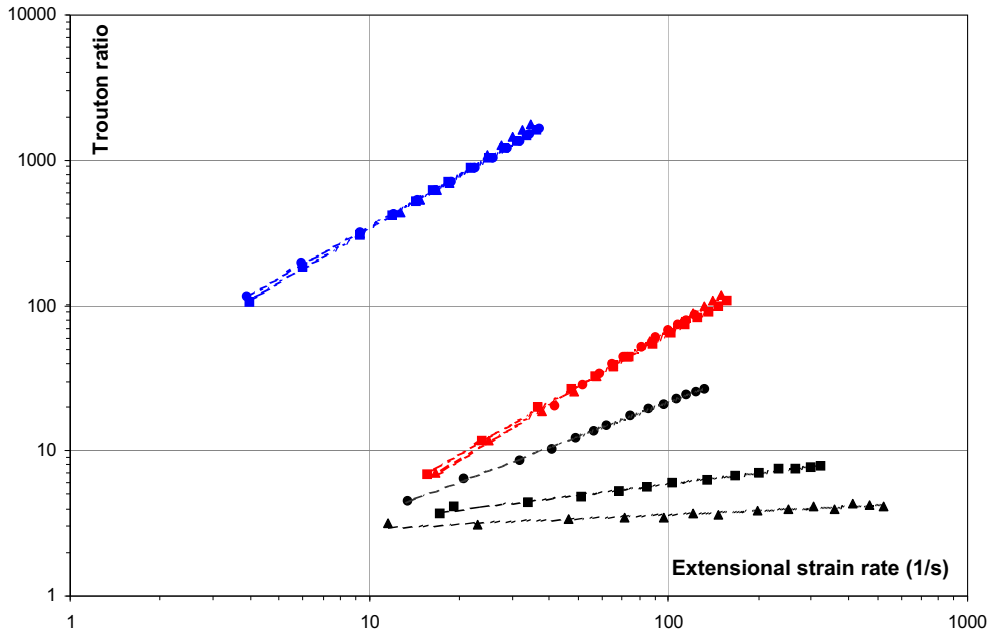

Figure 118. Trouton ratio vs. extensional rate for three materials: zirconia (Blue), alumina (Red), silicon carbide (Black) and these temperatures: 125°C (circle), 130°C (square), 135°C (triangle). Cogswell's (points) and Binding's analysis (lines)

As is show in Figure 118 once again, silicon carbide presents a different behaviour with a strong impact of temperature changes.

Bibliography.

[1] – A. Einstein, “Eine neue Bestimmung der Molekuldimensionen,” Ann. Phys. 19 (1906) p.289–306; English translation in “Investigation on the Theory of Brownian Motion”, Dover, New York, (1956).

[2] – Bird, R. B., Armstrong, B. C., and Hassager, O., “Dynamics of polymeric liquids”: Volume 1 Fluid Mechanics, John Wiley & Sons, New York, (1987).

[3] – M. Kluppel, “The role of disorder in filler reinforcement of elastomers on various length scales” Adv. Polym. Sci. 164, p.1-86, (2003).

[4] – J.C. Huang, C.L. Wu, "Processability, Mechanical properties, and electrical conductivities of carbon black-filled ethylene-vinyl acetate copolymers", Adv. Polym. Tech., 19(2), p.132-139, (200).

[5] – E. B. Bagley “End Corrections in the capillary flow of polyethylene”, J. Appl. Phys, 18, p.624-627, (1957).

[6] – F. N. Cogswell “Converging Flow of Polymer Melts in Extrusion Dies”, Polym. Eng. Sci., 12, p.64-73, (1972).

[7] – D. M. Binding “An Approximate Analysis for Contraction and Converging Flows”, J. Non-Newtonian Fluid Mechanics, 27, p.173-189, (1988).

[8] – F.T Trouton, "On the coefficient of viscous traction and its relation to that of viscosity" Proc. Roy. Soc. A77, p.426-440, (1906).

Conclusions.

Processing of ceramics is a major research topic of the SPCTS laboratory where this work was conducted. Rheological characterization of a paste is a prerequisite to master a forming process such as extrusion or injection moulding and this was one of the pursued objectives. The other, more ambitious, objective was to relate these properties to the physico-chemical composition. This is possible if complementary techniques are used such as DSC, SEM or sedimentation tests. The studied paste, comprising several organic components: paraffin (28%), EVA (8%), carnauba wax (4%) mixed with a zirconia submicronic powder (60%vol.) was found adequate for injection moulding in a previous study. Starting from this initial composition, several parameters were modified. First of all the solid content was varied (from 0 to 60%vol.) but also the organic matrix composition and the nature of the material (ZrO_2, Al_2O_3, SiC).

Einstein's law, extended through the concept of an effective solid concentration $k\phi$, is a simple and useful tool to characterize the degree of aggregation, k, which in turn depends on the adsorption of polymer molecules on the grain surfaces. The viscosity of a paste with low solid fraction (≤5%vol.) is measured at high shear rates and plotted as a function of solid content ϕ. A good correlation was found between the values of k and the role of each constituent. The molecules of carnauba wax act as a dispersant, k=1.1, while the copolymer EVA binds the grains, k=3.6. Paraffin molecules do not interact and aggregation proceeds most probably through Van der Waals attractive forces; it acts as a solvent. More surprisingly, because established on weaker foundations than Einstein's law, the Krieger-Dougherty equation was found to be useful to extend the analysis to higher solid contents. When the latter increases, the aggregates densify and ultimately at high shear stresses break down into individual particles (k=1.1). This analysis has proved that, in the case of zirconia, EVA and carnauba wax molecules adsorb in a volume ratio 2/1, which was found adequate for injection. For 30%vol. of powder, adsorption is complete (30%vol.). It is not so high in the case of alumina (11%) and even lower in the case of silicon carbide (5%). Most probably EVA does not interact (or very little) with silicon carbide grains.

Another important aspect to be considered is the miscibility of the different organic components. They are in general immiscible and this was found to be the case, raising the

question of the compatibility of the different phases with the solid. In the studied pastes, SEM observations show that the grains are not wetted by paraffin and this can be related to the adsorption properties already discussed. The solid being limited to the EVA and carnauba wax inclusions, this also explains why the aggregates densify on increasing the solid content: it is the only way to accommodate the largest amount of powder. From the rheological point of view, the inclusions become more and more rigid. The dependence of the complex elastic modulus on frequency shows a transition from a liquid to solid behaviour. When the inclusions are full, they interact because their volume is close to the percolation threshold (30%vol) and two viscosity jumps can be seen on the flow curve. The first one at low shear stresses relates to the interactions between the inclusions, and the second one to the breakdown of the inclusions. Using a capillary rheometer, a third viscosity jump of small amplitude is revealed at high shear stresses corresponding to the breakdown of aggregates into individual particles. Clearly, there must be some limit to the capacity of the inclusions to incorporate the solid. The evolution of the system depends on the EVA and carnauba wax contents: the two polymers act in opposite ways. An excess of EVA, i.e. the part of untrapped EVA, which shows some affinity to paraffin, leads to the formation of a homogeneous paste for a solid content of 40%vol. while an excess of carnauba wax promote stabilisation of the inclusions. The former paste shows only one viscosity jump and is quite fluid, even at low shear stresses.

In order to minimize the difficulties (and cost!) during the debinding step, homogeneity of the paste is a necessary condition to increase the solid fraction as much as possible. For.50 and 60%vol. of powder the paste behaves at low shear stresses almost as a solid showing a very high viscosity ($>10^7$ Pa.s.). For a given critical stress, a rapid transition occurs towards a fluid like behaviour. The flow curve can be fitted with a Bingham law. This is interpreted as the disruption of a network formed by interacting grains. The paste is strongly thixotropic, the kinetics of this mechanism being very slow. As a consequence, the critical stress depends on the duration of the experiment. A model developed by Coussot et al. is a good compromise between an entirely mathematical approach and a detailed physical description and it gives a good fit of the data. Some of the limitations were pointed out. The properties are very similar for the three materials investigated.

In a process, deformation involves both shear and elongational strains. While a rotational rheometer permits a detailed analysis of the shear properties, elongational ones are

difficult to investigate. A capillary rheometer is a very interesting tool because it gives an estimation of the extensional viscosity, η_E, through the determination of the Bagley's pressure drop at the entrance of the capillary. It is found to be an increasing function of the strain rate, contrary to the shear viscosity, η, which is shear thinning. η did not show major variations with the nature of the powder but η_E proved to be very sensitive with a Trouton ratio, i.e. η_E/η, decreasing in the order Y-ZrO_2 >> Al_2O_3 > SiC from 1000 down to 4. This last value is close to 3, the predicted value in the case of a Newtonian behaviour. This is clearly related to the amount of adsorbed EVA.